Corinna Maria Weixler, BSc

# Influence of different A-site cations on the properties of tin halide perovskites for the application in solar cells

**MASTER'S THESIS**

to achieve the university degree of

Diplom-Ingenieurin

Master's degree programme: Technical Chemistry

submitted to

**Graz University of Technology**

Supervisor

Assoc.Prof. Dipl.-Ing. Dr.techn. Gregor Trimmel

Institute for Chemistry and Technology of Materials

Graz, June 2019

# AFFIDAVIT

I declare that I have authored this thesis independently, that I have not used other than the declared sources/resources, and that I have explicitly indicated all material which has been quoted either literally or by content from the sources used. The text document uploaded to TUGRAZonline is identical to the present master‘s thesis.

# EIDESSTATTLICHE ERKLÄRUNG

Ich erkläre an Eides statt, dass ich die vorliegende Arbeit selbstständig verfasst, andere als die angegebenen Quellen/Hilfsmittel nicht benutzt, und die den benutzten Quellen wörtlich und inhaltlich entnommenen Stellen als solche kenntlich gemacht habe. Das in TUGRAZonline hochgeladene Textdokument ist mit der vorliegenden Masterarbeit identisch.

Date/Datum

Signature/Unterschrift

# Abstract

Over the last years, perovskite solar cells (PSC) developed to a promising new alternative to the currently market leading silicon based solar cells. Especially, lead PSCs were investigated extensively and were up to now improved to efficiencies greater than 23%. However, as lead exhibits a high toxicity, carcinogenicity and environmental toxicity, research towards alternatives is in progress. In the course of this work, the influence of different A-site cations in $ASnI_3$ perovskites on structure and optical properties as well as on the cell performance and the cell stability was investigated. Therefore, diverse characterization methods like X-ray diffraction, UV-VIS spectroscopy, scanning electron microscopy, optical microscopy, profilometry measurements, current-voltage plots and external quantum efficiency measurements were used. All cells contained perovskite layers that were prepared by means of solution processing, using an antisolvent (AS) precipitation step.

First, a formamidinium tin iodide ($FASnI_3$) reference system was used to investigate and improve the solar cells. Therefore, different methods like AS dripping at varying times, hot AS dripping and hot substrate spinning, for the formation of $FASnI_3$ perovskite layers, were tested. Among all these methods, the best results were obtained with an optimized AS dripping procedure, which was also used for further experiments. Furthermore, the influence of different $SnF_2$ additions to the perovskite precursor solution and the integration of different interlayers between the hole transport and the perovskite absorber layer were studied. Optical and structural investigations of this material were in accordance with literature data. The prepared $FASnI_3$ solar cells were able to achieve a power conversion efficiency (PCE) of 3.55%. In addition, the single cation perovskites $CsSnI_3$ and $RbSnI_3$ were prepared and characterized. It was shown that $CsSnI_3$ crystallized in an orthorhombic B-γ polymorph, but low PCEs suggest the conclusion that the used cell set-up seemed to be inappropriate for this material. In contrast, $RbSnI_3$ crystallized in a photoinactive yellow 1D crystal structure.

Moreover, another main part of this work was the investigation of mixed A-site cation perovskites. For that purpose, small amounts of piperazine-1,4-diium iodide ($PIPI_2$) and n-hexylammonium iodide (HAI) were added to a $FASnI_3$ precursor solution and the best resulting new PSCs were characterized in more detail. Structural investigation of $FA_{0.98}PIP_{0.02}SnI_3$ provided no evidence for insertion of PIP into the perovskite structure, whereas $FA_{0.95}HA_{0.05}SnI_3$ most probably changes to a lower dimensionality. The small amounts of $PIPI_2$ and HAI almost did not cause any changes of the absorption spectra and determined bandgaps compared to $FASnI_3$. Furthermore, current-voltage measurements were carried out and provided highest PCEs of 1.49% for $FA_{0.98}PIP_{0.02}SnI_3$ and 2.31% for $FA_{0.95}HA_{0.05}SnI_3$.

# Kurzfassung

Perowskitsolarzellen (PSZ) haben sich über die letzten Jahre hinweg zu einer vielversprechenden neuen Alternative zu den derzeit markführenden Siliziumsolarzellen entwickelt. Vor allem Blei-basierte PSZ wurden umfassend untersucht und konnten bisher zu Effizienzen von über 23% verbessert werden. Da Blei jedoch eine hohe Toxizität, Karzinogenität und Umweltschädlichkeit aufweist, ist die Forschung nach Alternativen im Gange. Im Zuge dieser Arbeit, wurde der Einfluss unterschiedlicher A-Kationen eines $ASnI_3$ Perowskiten auf die Struktur, die optischen Eigenschaften als auch die Zellleistung und die Zellstabilität untersucht. Es wurden hierzu Messmethoden wie Röntgendiffraktometrie, UV-VIS Spektroskopie, Rasterelektronenmikroskopie, optische Mikroskopie, Profilometrie, Strom-Spannungs-Messungen als auch externe Quanteneffizienzmessungen verwendet. Alle Zellen enthielten Perowskitschichten die anhand eines Lösungsprozesses unter Verwendung eines Antisolvent (AS) Fällungsschrittes hergestellt wurden.

Zuerst wurde ein Formamidiniumzinniodid ($FASnI_3$) Referenzsystem verwendet um die Solarzellen zu untersuchen und zu verbessern. Dazu wurden unterschiedliche Methoden wie *AS dripping* zu unterschiedlichen Zeitpunkten, heißes *AS dripping* als auch heißes *substrate spinning* für die Herstellung von $FASnI_3$ Perowskitschichten getestet. Unter all diesen Methoden wurden die besten Ergebnisse mit einem optimierten *AS dripping* erhalten, welches auch für weitere Experimente verwendet wurde. Zusätzlich wurden der Einfluss von unterschiedlichen $SnF_2$ Zusätzen zur Perowskit Precursor-Lösung und der Einbau von unterschiedlichen Zwischenschichten zwischen die Lochleiter- und Perowskit Absorberschicht untersucht. Optische und strukturelle Untersuchungen dieses Materials waren in Übereinstimmung mit Literaturdaten. Die gebrauchsfertigen $FASnI_3$ Solarzellen konnten eine Effizienz von 3.55% erzielen. Darüber hinaus, wurden auch die ein-kationischen Perowskite $CsSnI_3$ und $RbSnI_3$ hergestellt und charakterisiert. Es wurde gezeigt, dass $CsSnI_3$ in einem orthorhombischen B-γ Polymorph kristallisiert, jedoch lassen niedrige Effizienzen vermuten, dass der gewählte Aufbau für dieses Material unpassend ist. Im Gegensatz dazu kristallisierte $RbSnI_3$ in einer photoinaktiven, gelben 1D-Kristallstruktur.

Zudem war ein weiterer Hauptteil dieser Arbeit die Untersuchung von gemischten A-kationischen Perowskiten. Für diesen Zweck wurden kleine Mengen Piperazin-1,4-diiumiodid ($PIPI_2$) und n-Hexylammoniumiodid (HAI) zu einer $FASnI_3$ Precursor-Lösung zugegeben und die besten resultierenden PSZ genauer charakterisiert. Strukturelle Untersuchungen von $FA_{0.98}PIP_{0.02}SnI_3$ zeigten keinen Beweis für den Einbau von PIP in die Perowskitstruktur, wohingegen $FA_{0.95}HA_{0.05}SnI_3$ vermutlich eine niedrigere Dimensionalität ausbildet. Die geringen Mengen von $PIPI_2$ und HAI hatten kaum Änderung der Absorptionsspektren und der Bandlücke im Vergleich zu dem puren $FASnI_3$ zur Folge. Zudem wurden auch Strom-Spannungs-Messungen durchgeführt, die höchste Effizienzen von 1.49% für $FA_{0.98}PIP_{0.02}SnI_3$ und 2.31% für $FA_{0.95}HA_{0.05}SnI_3$ zeigten.

# Acknowledgement

I am using this opportunity to thank all the people, who supported me during this thesis. At this point I especially want to thank Assoc.Prof. Dipl.-Ing. Dr.techn. Gregor Trimmel for giving me the chance to work in the field of solar cells and for supervision of my work.

Furthermore, I want to thank Dipl.-Ing. Dr.techn. Sebastian Höfler BSc, MSc Jimmy Mangalam BSc, Dipl.-Ing. Dr.techn. Thomas Rath and Dipl.-Ing. Stefan Weber BSc for their good advice, support during work and their helpful ideas all the time.

I want to thank Mrs. Birgit Kunert for doing the XRD measurements and Dr. Theodoros Dimopoulos for the SEM measurements.

I also want to thank the project PERMASOL and the cooperation partners the Austrian Institute of Technology, the Johanneum Research and the University of Patras.

Additionally, I want to thank the whole working group for the very good atmosphere there. It was a great experience to be part of such a nice and supportive team.

Finally, I want to express my profound gratitude to my parents, my sister and my boyfriend for their moral support over the last years. Thank you.

# List of Abbreviations

| | |
|---|---|
| *AS* | antisolvent |
| *BCP* | bathocuproine |
| *CB* | chlorobenzene |
| *DMF* | dimethyl formamide |
| *DMSO* | dimethyl sulfoxide |
| *DSSC* | dye sensitized solar cell |
| $E_f$ | fermi level |
| $E_g$ | bandgap |
| *ETL* | electron transport layer |
| *EQE* | external quantum efficiency |
| *FA* | formamidinium |
| *FF* | fill factor |
| *FTO* | fluorine doped tin oxide |
| *GA* | guanidinium |
| *HA* | hexylammonium |
| *HOMO* | highest occupied molecular orbital |
| *HTL* | hole transport layer |
| *I* | current |
| $I_{SC}$ | short circuit current |
| *ITO* | indium tin oxide |
| *J* | current density |
| *LUMO* | lowest unoccupied molecular orbital |
| *MA* | methylammonium |
| *MPP* | maximum power point |
| *m-MTDATA* | 4,4',4"-Tris[(3-methylphenyl)phenylamino]triphenylamine |
| *P* | Power |
| $PC_{60}BM$ | [6,6]-Phenyl-C61-butyric acid methyl ester |
| *PCE* | power conversion efficiency |
| *PEA* | phenylethylammonium |
| *PEDOT:PSS* | Poly(2,3-dihydrothieno-1,4-dioxin)-poly(styrenesulfonate) |

| | |
|---|---|
| *PIP* | piperazine-1,4-diium |
| *PSC* | perovskite solar cell |
| *PTAA* | poly(triaryl amine) |
| *P3HT* | poly(3-hexylthiophene-2,5-diyl) |
| *SEM* | scanning electron microscopy |
| *Spiro-OMeTAD* | $N^2$,$N^2$,$N^{2'}$,$N^{2'}$,$N^7$,$N^7$,$N^{7'}$,$N^{7'}$-octakis(4-methoxyphenyl)-9,9′-spirobi[9H-fluorene]-2,2′,7,7′-tetramine |
| *TCO* | transparent conductive oxide |
| *TGA* | thermogravimetric analysis |
| *V* | voltage |
| $V_{OC}$ | open circuit voltage |
| *XRD* | X-ray diffraction |

# Table of Contents

# 1 Introduction

The demand for energy increased very much over the last decade and reached its record high in 2018. In that year the total energy demand rose by 2.3% with China, the United States and India as main contributors. This development can be explained by a growing global economy and higher heating and cooling needs in a few regions. As a consequence, the demand for all fuels increased as well. A main problem the world has to face, is the increasing demand in electricity, which rose by 4% in 2018 and now nearly reaches a 20% share in total energy consumption.[1] Due to that fast rise in energy demand the global warming also developed to a severe problem over the last decades and is mainly caused by the anthropogenic greenhouse effect. Especially, the concentrations of the greenhouse gases carbon dioxide, methane and nitrous oxide have risen strongly. For example, the concentration of $CO_2$ increased by approximately 40% compared to pre-industrial levels and thus, causes the largest contribution to radiative forcing.[2] In 2018 the $CO_2$ emissions rose by 1.7%, which corresponds to a total of 33 Gt $CO_2$ emissions worldwide.[1] To assess the climate development in the past and forecast trends, different climate scenarios were developed. One important scenario is the 450 scenario, which describes a 50% chance of limiting the average global temperature increase to two degrees compared to pre-industrial levels.[3] To implement this temperature goal, the global greenhouse gas emissions should not exceed 450 ppm $CO_2$ equivalents in long term.[4] Therefore, the usage of renewable technologies gains in importance.

The main renewable energy sources are bioenergy, hydropower, solar energy and wind energy. They all contribute to the total energy consumption in the electricity, heat and transport sector. Figure 1 demonstrates the total renewable energy consumption of the European Union for 2017 and 2023.[5]

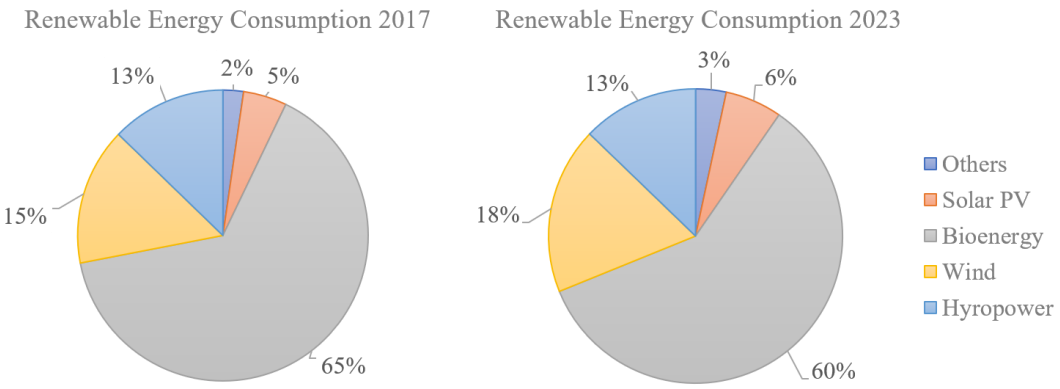


**Figure 1** *Consumption of renewable energy in 2017 and forecast of the energy consumption in 2023 for the European Union. Figure based on data from literature 5.*

In 2023 the share of renewables in the power sector will increase and will reach approximately 30%. This growth is primarily caused by solar photovoltaics followed by wind, hydropower and bioenergy.[5]

The sun is one of the most important renewable energy sources and provides $1.08*10^{18}$ kWh energy per year. Only one ten thousandths of the incoming solar energy would be enough to cover the energy demand worldwide.[6] At the time different types of technologies are used to provide energy from the sun. The most common ones comprise solar photovoltaics, solar thermal power systems, solar space heating and cooling systems as well as solar water heating systems. Electricity generation can be done with the first two mentioned types. In solar PVs the photovoltaic effect is used to convert solar energy directly into electricity. An indirect way to provide electricity is utilized in solar thermal power systems. Here, solar concentrating collectors are used to drive a heat engine and further convert this mechanical energy into electrical energy.[7] In general, there exist many different types of solar cells like for example silicon solar cells, organic solar cells, dye sensitized solar cells or also perovskite solar cells.[8,9] Especially, lead perovskite solar cells gained much attention, due to their fast increase in power conversion efficiencies over the last years. However, lead shows the main drawback of high toxicity for environment and therefore, also alternative elements like tin or germanium, were studied extensively.[10]

During this work different tin-based perovskite solar cells were fabricated and investigated. One main focus was on the development and improvement of a stable and reliable reference system. Therefore, different single cation perovskites like $FASnI_3$, $CsSnI_3$ and $RbSnI_3$ were studied. All investigated cells had the set-up "Glass-ITO/PEDOT:PSS/Perovskite/$PC_{60}BM$/Aluminium". Based on these results, $FASnI_3$ seemed to be a promising candidate as a reference perovskite material. First, improvements concerning the preparation of the perovskite layer were carried out. Therefore, antisolvent (AS) dripping times, hot AS dripping and hot substrate spinning were tested. Furthermore, different layer thicknesses and $SnF_2$ concentrations as well as the insertion of interlayers between PEDOT:PSS and the perovskite layer were investigated. Another important part of this work was the investigation of new mixed tin halide perovskites. For that purpose, varying amounts of n-hexylammonium iodide and piperazine-1,4-diium iodide were integrated into the $FASnI_3$ structure. Extensive characterization of the reference system and the newly developed double cationic perovskites was conducted, using methods like current-voltage-measurements, UV-VIS spectroscopy, profilometry, scanning electron microscopy, light microscopy and X-ray diffraction.

# 2 Theoretical Background

## 2.1 Working principle of a solar cell

To understand the working principle of a solar cell it is necessary to understand a semiconducting material. In general, every electron in an atom possesses discrete energy levels. If many atoms are combined, like it is the case in a solid, the energy levels must shift to lower or higher energies due to the Pauli exclusion principle, which describes that no more than two electrons are capable to occupy each energy level. The splitting causes the formation of many energy levels with small differences in energies that so-called "energy bands" can be formed. One can differ between the valence band, which is the energy band of lower energy and the conduction band, which is the energy band of higher energy. Depending on the materials that are used, it may lead to a gap between the shifted energy levels that is called "bandgap". There can be distinguished three types of materials: metals (overlapping valence and conduction band), semiconductors (bandgaps up to 4.0 eV) and insulators (bandgaps > 4.0 eV).[11] Figure 2 illustrates the behavior of such materials.

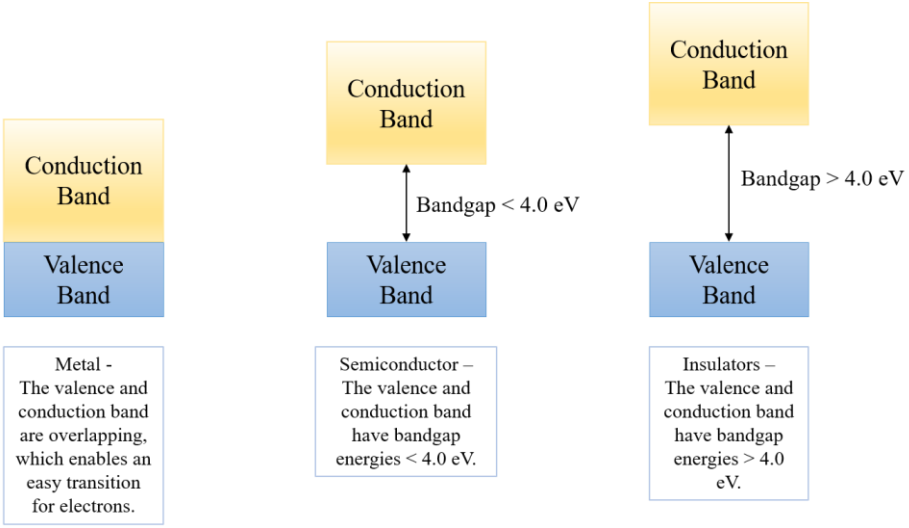


**Figure 2** *Band structures of metals, semiconductors and insulators. Self-designed based on literature 11.*

A semiconducting material has relatively low bandgap energies and possesses conductivities between metals and insulators at room temperature.[12] In general, one can differ between intrinsic and extrinsic semiconductors. Intrinsic semiconductors are mostly influenced by temperature and are independent of impurities. The properties of extrinsic semiconductors (n- or p- type) are normally determined by usage of dopants. Doping describes the insertion of impurities into a semiconducting material to improve its conductivity. For n-type semiconducting materials normally impurities that cause an electron excess in the material (e.g. addition of phosphorus or antimony to silicon or germanium) are inserted. The p-type doping in contrast works with additions of impurities that result in a deficiency of electrons in the material (e.g. addition of gallium or boron to silicon or germanium). The main advantage of such

materials is that they are independent of temperature and therefore, very interesting for different technical applications.[11,13]

A photovoltaic cell describes a device, which is capable to convert radiant energy into electrical energy.[12] This is achieved by light induced charge generation, followed by the transport of the generated charges and their collection at the electrodes.[9] The underlying working principle can vary between the different types of solar cells. In this chapter, the main focus will be on the investigation of perovskite solar cells (PSCs).

The first step is induced by the absorption of incoming photons that cause the formation of an electron-hole pair called "exciton". In the past it was shown that the excitons formed in perovskite solar cells, have very small binding energies and can therefore, decompose easily into free electrons and holes.[9] Only a photon with an energy higher than the bandgap energy can excite an electron from the valence into the conduction band.[14] The formed free charges are then separated in an electric field.[12] The simplest form of a photodiode can be described with a p-n junction. If the n-type and p-type semiconductors come in contact with each other it is generated a concentration gradient in the material that causes a diffusion current. This diffusion current evolves from the flow of the free charges. The electrons from the n-type semiconductor migrate to the p-type semiconductor to recombine there with the holes and leave behind a fixed positive charge. For holes the same process takes place, they flow from the p-type to the n-type semiconductor and leave behind fixed negative charges. After a while there are nearly no free charges left at the interfaces and only fixed charges remain in the materials. It develops an electric field that forces the electrons to the n-type side and holes to the p-type side resulting in a drift current. The resulted drift current and the diffusion current are in equilibrium with each other and cause the formation of a space-charge region at the p-n junction. This behavior is exemplified in figure 3. For a better understanding, also the band diagrams of these materials are shown. In general, an undoped (intrinsic) semiconductor should have a fermi level directly in the middle of the bandgap. Doping results in a displacement of the fermi levels so that the n-doped material (electron excess, higher probability that electrons are in the conduction band) has a higher fermi energy and the p-doped material (electron deficiency, higher probability that electrons are in the valence band) has a lower fermi energy.[14] The produced charges are separated by this generated electric field and travel through the doped regions to the respective electrodes, where the charges are collected. The electrons are directed to the n-type semiconductor and the holes to the p-type semiconductor. In the end, the electrons are transported through an external circuit to the back contact to recombine there with the holes, generating a current.[8,12]

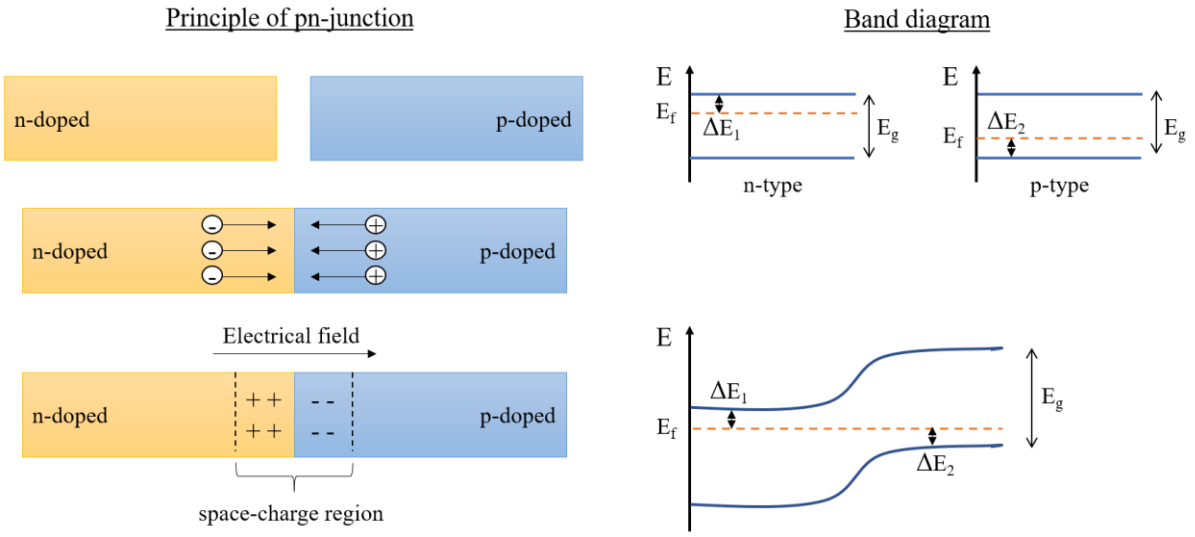


**Figure 3** *Principle of a p-n junction and the corresponding band diagrams for the n- and p- doped semiconductors. Self-designed based on literature 14.*

PSCs typically work as n-i-p or p-i-n junction solar cells. They normally consist of a transparent conductive glass that is coated with either an electron selective (n-type) or a hole selective (p-type) contact, followed by a light absorbing perovskite layer, an electron or hole selective layer and a metal contact. For that purpose, an intrinsic semiconductor is normally sandwiched between a n-type and a p-type semiconducting material.[15] This is necessary to achieve charge separation and to create an electric field in the photovoltaic cell. The working principle of a n-i-p junction solar cell is pictured in figure 4.

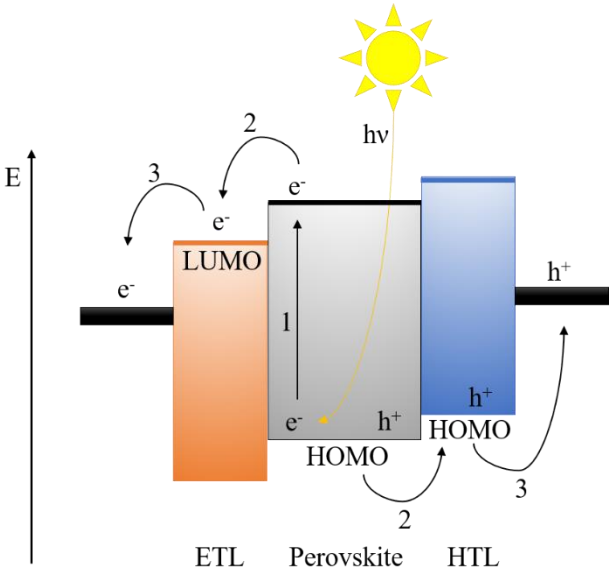


**Figure 4** *Working principle of a perovskite solar cell with a n-i-p architecture.* ***(1)*** *Absorption of a photon and generation of free charges;* ***(2)*** *Charge transport to the hole and electron transport materials;* ***(3)*** *Extraction of the charges by the electrodes. Self-designed based on literature 9.*

Here, the first step is induced by incoming light that excites an electron from the valence into the conduction band of the absorber material. Afterwards, the electrons migrate to the ETL forming a n-i junction and the holes migrate to the HTL forming an i-p junction. The electrons and holes can be collected at the corresponding electrodes. If the two electrodes are connected, the electrons are injected into an external circuit and can recombine again with the holes at the HTL/back contact to generate a current. During this process the charges flow until equilibrium is reached and a space-charge region can be formed at the respective interfaces, which causes band-bending. For this process the band alignment of the different layers in the perovskite solar cell is of high importance. In general, the conduction band edge of the ETL should be lower than that of the absorber layer and the valence band edge of the HTL should be higher compared to that of the absorber layer.[8]

The usage of a p-i-n junction shows sometimes advantages over the normal p-n junction. With the integration of the intrinsic semiconductor (perovskite absorber layer) it is possible to increase the depletion region between the n-type and the p-type semiconductor, resulting in larger radiation absorption region that can be helpful to increase the efficiency of a photodiode. Furthermore, they often provide higher quantum efficiencies, higher bandwidths and reduced capacitance compared to normal p-n junction solar cells.[16–20]

## 2.2 Solar cell characteristics

A solar cell works like a photodiode and can be characterized with IV-measurements (Current-Voltage measurements), that are normally carried out under standard test conditions (STC). Therefore, solar cells are measured under controlled conditions with an artificial light source at AM1.5 (air mass 1.5) with a power density of 1000 W/m$^2$ at 25 °C.[21] The air mass is defined by the magnitude of $1/\sin(\gamma_S)$, where $\gamma_S$ describes the angle between the incident light to the earth's surface (elevation angle). The air mass of 1.5 at STC would correspond to a $\gamma_S$-angle of approximately 41.8°. The smaller the angle of $\gamma_S$, the longer is the way of sunlight through the atmosphere and the higher is the AM value.[22] However, it is also possible to define the AM by the angle $\theta$ between the zenith (vertical to earth's surface) and the incident sunlight, which changes the formula for the AM to $1/\cos\theta$. In this case, an AM of 1.5 would correspond to an $\theta$-angle of 48.2°.[23,24]

Figure 5 pictures typical IV-curves of a solar cell device that was measured in the dark and during illumination. It can be seen, that the current output increases with increasing illumination of the solar cell. In case of the dark curve, no current is generated during measurement.[25]

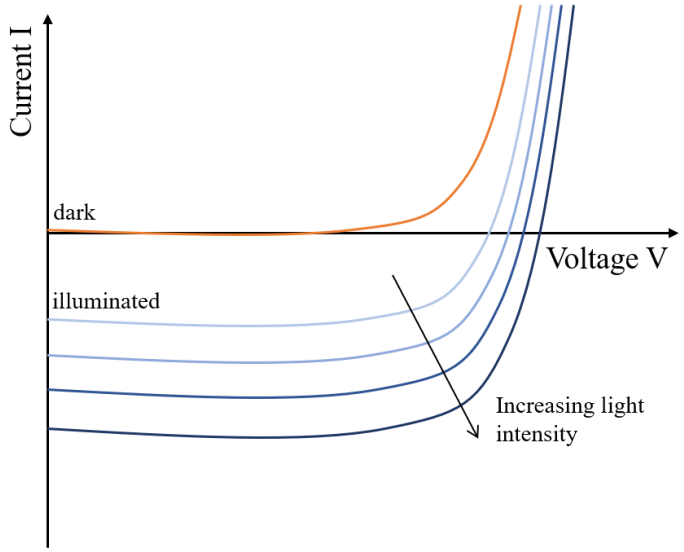


**Figure 5** *IV-curves of a solar cell: The dark curve pictures a solar cell that is not illuminated and generates no current; the blue curves show the generated current by a solar cell when the light intensity is increased. Self-designed based on literature 25.*

The generated photocurrent strongly depends on the absorption properties and the quantum efficiency of a material. In general, the absorption can be increased if the reflection of the material is reduced to a minimum (use of antireflective surfaces). Investigations of the internal (considers reflection) and external quantum efficiency enable a determination of electron-hole pairs that contribute to the generated photocurrent.[26]

The IV-curves can be used to obtain information about important cell parameters like the Short Circuit Current ($I_{SC}$), the Open Circuit Voltage ($V_{OC}$), the Maximum Power Point (MPP), the Fill Factor (FF) and the Power Conversion Efficiency (PCE). In figure 6 are shown all important cell parameters.

The $I_{SC}$ can be determined by the intersection of the IV-curve with the Current axis (y-axis). At this point, the current that flows in the solar cell reaches its maximum and can only occur when the voltage in the device is zero (means when the device is short circuited). It can be influenced by the area of the solar cell, the light intensity, the spectrum of the light and optical losses. To consider the area dependence, it is often useful to use the current density J ($mA*cm^{-2}$) instead of the current I.[22,26,27]

Another important parameter is the $V_{OC}$, that can be taken from the intersection of the IV-curve with the voltage axis (x-axis). The value corresponds to the maximum voltage of a solar cell when no current flows through the device. If the $V_{OC}$ or $I_{SC}$ are equal to zero the solar cell cannot generate any electric power.[22,26,28]

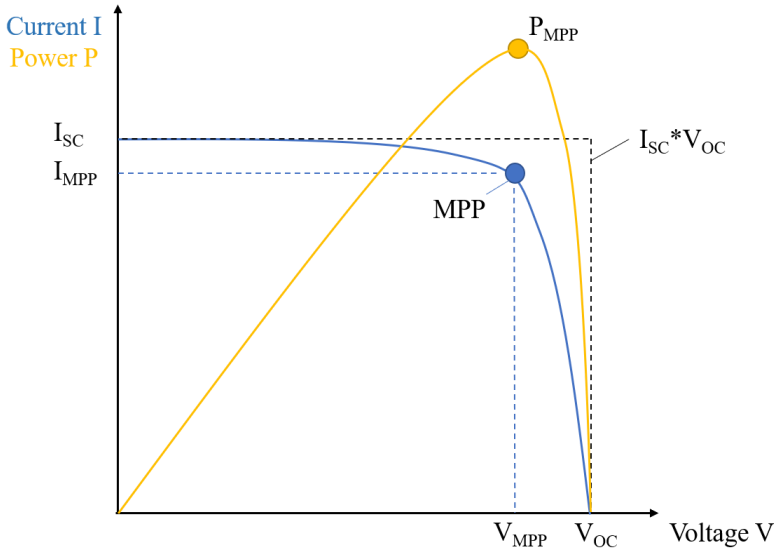


**Figure 6** *IV-curve and Power-curve of a solar cell. In the picture are shown the most important cell parameters. Self-designed based on literature 26.*

In general, the power P can be defined by the product of I*V. The highest achievable power of a solar cell is called the Maximum Power Point (MPP), and the corresponding current and voltage at MPP are called $I_{MPP}$ and $V_{MPP}$. This parameter describes the area of the largest rectangle that fits in the IV-curve. Based on these values, it is possible to define another new parameter called "Fill Factor". It is a measure for the quality of a cell and can be calculated with the ratio of the maximum power to the product of $I_{SC}$ and $V_{OC}$ (see formula 1).[21,26,29]

$$FF = \frac{V_{MPP} * I_{MPP}}{V_{OC} * I_{SC}} = \frac{P_{MPP}}{V_{OC} * I_{SC}} \qquad \textit{Formula (1)}$$

Typically, the FF shows magnitudes between 25% - 94%, whereas low values are mainly caused by high series resistances or low shunt resistances. These resistances originate especially from high resistive materials or layers with many defects that reduce the mobility of charge carriers.[22]

However, the efficiency of a solar cell is one of the most important parameters and is used to compare different solar cells. Since, the efficiency is highly dependent on the solar spectrum, the intensity of the incoming light and the temperature it is necessary to measure the solar cells under STC. The efficiency can be calculated with the maximum achievable power $P_{MPP}$ over the input power of the sunlight $P_{in}$ (formula 2).[30]

$$\eta = \frac{P_{MPP}}{P_{in}} = \frac{V_{OC} * I_{SC} * FF}{P_{in}} \qquad \textit{Formula (2)}$$

## 2.3 Perovskite solar cells

Over the last years perovskite solar cells developed to an interesting alternative to more established solar cell materials based on Si, CdTe or GaAs.[15] In 2009 the first group published a dye sensitized solar cell that contained a methylammonium lead halide perovskite adsorbed on a nanocrystalline $TiO_2$ surface, which achieved efficiencies of around 3-4%. Further improvements were done on liquid perovskite solar cells, but they attained little attention.[31] A few years later in 2012, the first long-term durable stable solid-state perovskite solar cell with a PCE of 9.7% was discovered and research towards perovskite solar cells increased. Two years later it was already possible to fabricate perovskite solar cells with a certified PCE of 17.9 %, which improved further to record efficiencies of 25%.[32,33]

Originally, the perovskite structure was related to the crystal structure of calcium titanate that was discovered in 1839 by the mineralogist Gustav Rose and named after the Russian mineralogist Lev Perovski.[34] Typically, perovskites can be described with an $ABX_3$ crystal structure that can vary in its composition. They are most often composed of a monovalent A-site cation, a divalent metal atom as well as a halide anion at the X position. The A-site cations can vary very much and can have an inorganic (e.g. $K^+$, $Rb^+$, $Cs^+$) or organic nature (e.g. methylammonium ($MA^+$), formamidinium ($FA^+$)). For the B site of the perovskite structure, the metal cations $Pb^{2+}$ and $Sn^{2+}$ are mainly used and the X-site is normally occupied by a halide anion like chloride, bromide or iodide. However, not only halide anions but also other anionic species like oxides or chalcogenides are able to form a perovskite structure but are of less importance for the application in perovskite solar cells. Typically, the $BX_6^-$ octahedra form a connected 3-dimensional network with A-site cations at the 12-fold coordinated voids to gain charge neutrality. If the structure is imagined as a cubic unit cell, it consists of five atoms where the cation B has six nearest neighbors and the A-site cation has 12 nearest neighbors. However, also higher valent metal cations like $Bi^{3+}$ or $Sb^{3+}$ can be integrated at the B-site resulting in a $A_3B_2X_9$ structure. Figure 7 shows the structure of an $ABX_3$ perovskite.[35,36]

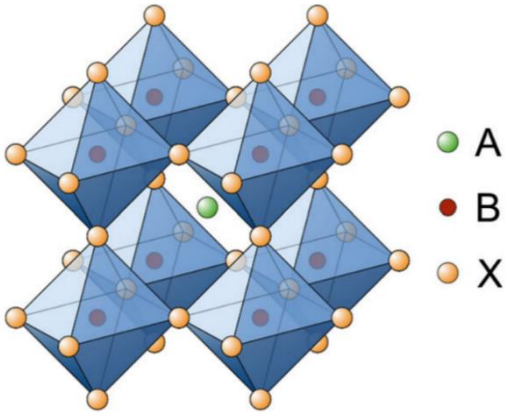


**Figure 7** *$ABX_3$ perovskite structure. Here, A describes a monovalent organic or inorganic cation ($FA^+$, $MA^+$, $Cs^+$, etc.), B a divalent metal atom ($Pb^{2+}$, $Sn^{2+}$) and X a halide anion ($I^-$, $Br^-$, $Cl^-$).*

*Reproduced from literature 35; Copyright by the authors.*

To investigate the structure and stability of a perovskite it is possible to use the octahedral factor μ (formula 3) and the Goldschmidt tolerance factor t (formula 4). In these equations the terms of $r_A, r_B, r_X$ are defined as the ionic radii of the A-site cation, B-site cation and X-site anion.

$$\mu = \frac{r_B}{r_X} \qquad \textit{Formula (3)}$$

$$t = \frac{r_A + r_X}{\sqrt{2} * (r_B + r_X)} \qquad \textit{Formula (4)}$$

Typically, the octahedral factor can be used to determine the stability of the $BX_6^-$ octahedra, while the Goldschmidt tolerance factor can be used to predict a crystal structure. To obtain a perovskite structure the tolerance factor should range between $0.8 \leq t \leq 1.0$. A tolerance factor close to one results normally in a cubic structure, while for lower values between 0.8 – 0.89 distorted structures (orthorhombic, tetragonal, rhombohedral) develop. Deviations from that region often results in lower dimensionalities or other crystal structures. Especially, large cations often lead to the formation of two-dimensional (layered), one-dimensional (chain-like) or zero-dimensional perovskite structures.[35,36] An important application is the usage as absorber material in perovskite solar cells, since these materials provide interesting properties like strong optical absorption, high electron and hole mobilities and diffusion lengths, high defect tolerance, low surface recombination rate, favorable grain boundaries and tunable bandgaps.[8] The electrical and optical properties of those materials can be influenced strongly by bandgap tuning. It was found that the bandgap correlates with the largest metal-halide-metal bond angle, that can be influenced by octahedra tilting. For that purpose, the steric size of the cation plays an important role and usually, the integration of suitable molecular cations can be helpful to control the bond angles. Often, the cations are only charge compensators and do not contribute directly to the band structure. However, their size and form can have an important influence on the deformation of the octahedra and as a consequence, on the absorption range and the band gap energy of the perovskite.[36,37]

In general, perovskite solar cells can be divided into the three main structures mesoscopic, planar and inverted. A mesoscopic device contains a nanostructured ETL (should provide better light harvesting and enhanced electronic collection efficiency). In contrast, the planar device does not have this nanostructured ETL but a similar set-up. Exchange of the ETL and the HTL results in an inverted PSC. Typical examples for ETMs are $TiO_2$ or ZnO nanostructures (for mesoscopic devices), PCBM or $C_{60}$, while HTMs can be for example spiro-OMeTAD, PTAA or PEDOT:PSS. All basic structures are pictured in figure 8.[38]

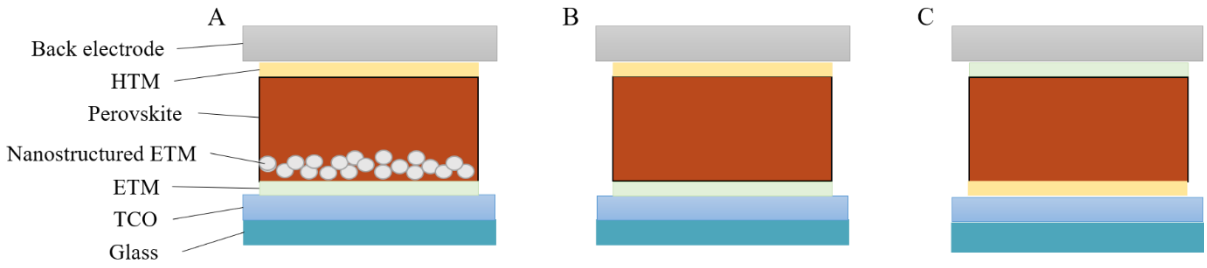


**Figure 8** *Mesoscopic (A), Planar (B), Inverted (C) cell set-up. Self-designed based on literature 38.*

### 2.3.1 Lead perovskite solar cells

Like mentioned above $Pb^{2+}$ cations are able to form perovskite structures with the formula $ABX_3$, where A is an organic or inorganic cation and X is a halide anion. Especially, lead perovskite solar cells were studied extensively over the last years, causing large increase in efficiencies from 3.8% in 2009 to 22.1% in 2016.[39] Recently, the National Renewable Energy Laboratory (NREL) reported an even higher PCE value of 25%, which is up to now the best reported efficiency for PSCs.[33]

In 2009, Kojima et al. were the first ones who demonstrated organo-lead halide perovskites as visible-light sensitizers in dye sensitized solar cells. They used a $MAPbI_3/TiO_2$ anode ($MA^+$ = methylammonium) , a Pt-coated fluorine doped tin oxide (FTO) glass as cathode and a mixture of LiI and $I_2$ dissolved in methoxyacetonitrile as electrolyte and were able to achieve a PCE of 3.81%.[40] Im et al. managed to further improve that system to efficiencies of 6.54% but mentioned high stability problems due to perovskite dissolution into the electrolyte.[41] Therefore, many other working groups began to investigate "solid-state perovskite solar cells" by usage of spiro-OMeTAD or PTAA as hole transport layers to improve the stability and efficiencies up to 12.0%.[42,43] In the very beginning especially, monocationic Pb-perovskites like $MAPbX_3$, $FAPbX_3$ ($FA^+$ = formamidinium) and $CsPbX_3$ were studied. $MAPbI_3$ was found to have long carrier lifetimes, very good charge carrier mobilities as well as long diffusion lengths but suffers from poor moisture stability, thermal degradation and observable hysteresis during operation.[39] At the time, the best $MAPbI_3$ PSCs reached efficiencies of greater 20% and were reported by Son et al., who improved the hole and electron extraction at the grain boundaries, and Momblona et al., who demonstrated a vacuum deposition method for the perovskite film to produce highly efficient solar cells.[44,45] Further improvements of these systems were achieved by using mixed A-site cations or mixed X-site anions, different HTMs and ETMs and new methods to prepare the perovskite absorber layer.[46] In 2016, Anaraki et al. fabricated a planar solar cell device with an efficiency of 20.7%, which is up to now the best reported PSC for this set-up. They used $SnO_2$ as electron selective layer (ESL), which was first spin coated onto an FTO substrate and post-treated with chemical bath deposition. Afterwards, the Cs/MA/FA containing mixed triple cation lead

iodide/bromide perovskite precursor solution was spin coated onto the ESL via AS dripping procedure, followed by spiro-OMeTAD and Au electrodes. The produced devices showed very high efficiencies of nearly 21%, mild hysteresis and good reproducibility.[47] However, higher PCEs were achieved with mesoscopic cell structures like demonstrated by Grätzels working group. They developed a cell that consisted of "Glass-FTO/compact $TiO_2$/mesoporous $TiO_2$/Perovskite/Spiro-OMeTAD/Au", whereby the lead perovskite layer was made of a quadruple composition of $Rb^+/Cs^+/MA^+/FA^+$ with mixed bromide and iodide anions (fabrication with chlorobenzene AS dripping procedure).[48] An even higher certified PCE of 22.1% was achieved by Yang et al., who used a special intramolecular exchange process to prepare the perovskite film. Therefore, a mixture of $PbI_2$ and $PbBr_2$ was spin coated onto a $TiO_2$ surface, followed by spin coating of a solution of MABr and FAI enriched with $I_3^-$ ions, to reduce iodide deficiency. The device showed the set-up "FTO/thin barrier $TiO_2$ (~60 nm)/mesoporous $TiO_2$ : perovskite composite layer (~150 nm)/perovskite upper layer (~500 nm)/PTAA (~50 nm)/Au (~100 nm)".[49]

### 2.3.2 Lead-free perovskite solar cells

Although, lead-based perovskites provided very good results in the past, their toxicity is a challenging problem. Lead is able to bind to thiol and cellular phosphate groups in enzymes, proteins and cell membranes and can therefore, affect the functionality of the hematopoietic, renal, reproductive and central nervous system, the latter is especially harmful for children. Furthermore, it is supposed that a few lead compounds are water-soluble, which enables an accumulation in the food chain. All these reasons led to an incorporation of lead to the "Restriction of Hazardous Substances" (RoHS), which prohibits and regulates the usage of hazardous substances in electrical and electronic equipment. The most interesting alternative metal cations comprise group 14 elements like $Sn^{2+}$ and $Ge^{2+}$ (3D perovskite framework), group 15 elements like $Bi^{3+}$ and $Sb^{3+}$ (pseudoperovskites without corner sharing octahedra) and transition metals like $Cu^{2+}$(forms typically 2D layered perovskites).[50,51] However, also these compounds can be dangerous for health and environment but still less harmful compared to lead based systems. Tin for example, is able to affect the iron/calcium metabolism and can cause nutritional disorders and inhibition of haematopoiesis. Bismuth has the property to denaturate and thus, destroy organisms that possess sylhydril groups and antimony can cause reproductive disorders, heart failure and hepatic damage.[50] Below, all these systems are discussed in more detail.

### *2.3.2.1 Tin perovskite solar cells*

Since, it was found that the stability of lead perovskites is in conjunction with the electronic configuration of lead ($s^2p^2$), other elements in the same group seemed to be the most promising alternatives to lead-based perovskites for solar cell applications. Especially, tin seems to be an interesting alternative due to its narrower bandgap energies that range from 1.2 to 1.4 eV and thus, are very near at the ideal bandgap energy of 1.34 eV (corresponds to a theoretical maximum PCE of around 33.5%) according to the Shockley-Queisser limit for single-junction solar cells. In order to form a perovskite structure, it is necessary that the metal cations keep their $s^2$ electron pair and lose their two electrons in the p-orbitals, resulting in a +2 charge of the metal cation. This inert s pair is more common in heavier elements such as lead, since the relativistic contraction stabilizes the s-orbitals. Therefore, lead is more stable in the divalent oxidation state compared to tin or germanium, which can be easily oxidized to the oxidation state +4 resulting in severe stability issues.[52–54] Thus, tin perovskites are usually fabricated in an inert atmosphere in absence of oxygen to prevent the formation of $Sn^{4+}$, which would lead to p-type doping and consequently, to higher carrier recombination and poor device performance.[10,55]

One of the most intensively studied A-site cations for the application in tin perovskite solar cells comprise methylammonium ($MA^+$, $CH_3NH_3^+$) and formamidinium ($FA^+$, $CH(NH_2)_2^+$) as organic cations as well as the inorganic cesium cation ($Cs^+$).[50]

$CsSnI_3$ was one of the first studied perovskite materials in solar cell devices, since it showed good thermal stability (approximately 400 °C), a low bandgap energy of 1.3 eV and very high hole mobilities.[51] The first time, it attracted attention in 2012, when it was used in dye sensitized solar cells as hole transport material.[56] Thereupon, Chung et al. investigated $CsSnI_3$ and found that this material is a direct p-type semiconductor with high carrier concentrations and exceptionally high hole mobility, which explains the metal-like character.[57] Kumar et al. demonstrates the usage of $CsSnI_3$ as absorber material in perovskite solar cell. They added $SnF_2$ to the perovskite solution to control its Sn-cation vacancies and consequently, its metal-like conductivity. Their best prepared cell had a "FTO/c-$TiO_2$/m-$TiO_2$/$CsSnI_3$/m-MTDATA/Au" set-up resulting in a PCE of 2.02% if 20 mol% $SnF_2$ were added.[58] By so far, the best $CsSnI_3$ cell was published in 2017 by Song et al. and achieved a PCE of 4.81% with a molar ratio of CsI:$SnI_2$ of 0.4:1. The preparation of the cell was carried out in a reducing vapour atmosphere of hydrazine.[53]

In 2014 Noel et al. described the first $MASnI_3$ perovskite solar cell with the device set-up "FTO/compact $TiO_2$/mesoporous $TiO_2$/$MASnI_3$/spiro-OMeTAD/Au" and achieved PCE values of 6.4% under illumination of 1 sun.[59] In the same year, also the research group of Kanatzidis demonstrated highly efficient methylammonium tin halide perovskite solar cells. They were capable to fabricate a $MASnI_{3-x}Br_x$ (x = 0,1,2,3) perovskite solar cell with a PCE of 5.73 %, using spiro-OMeTAD as HTL and $TiO_2$ as ETL and found out that an increasing amount of Br additions resulted in a blue shift of the

absorption onset, which leaded to a decreased $J_{SC}$ and increased $V_{OC}$.[50] The quality of a perovskite film is a limiting factor for highly efficient solar cell devices. Therefore, further research of Kanatzidis group provided results concerning the fabrication of highly uniform, pinhole-free perovskite films from dimethyl sulfoxide solution via a $SnI_2$*3 DMSO intermediate phase. It was supposed that the use of DMSO instead of DMF slows down the crystallization process and thus, provides an increased homogeneity of the perovskite film.[60]

Comparatively late, research on formamidinium tin halide perovskites as absorber materials for solar cells began. In 2013, Stoumpos et al. compared the properties of the three cations $MA^+$, $FA^+$ and $Cs^+$ in tin and lead iodide perovskites. They showed that the $FA^+$ ion in the tin iodide perovskite structure provides slightly higher resistivities and lower mobilities compared to $Cs^+$ or $MA^+$ but still, good ohmic behavior, which makes it an interesting material for energy-related applications.[61,62] The first investigation of such a formamidinium tin iodide absorber layer in perovskite solar cells was done in 2015. Koh et al. produced a $FASnI_3$ cell with the set-up "Glass-FTO/$TiO_2$ blocking layer/m-$TiO_2$/$FASnI_3$/Spiro-OMeTAD/Au" that possessed an optical bandgap of 1.41 eV and reached an efficiency of 2.10% upon incorporation of 20 mol% $SnF_2$. This work shows that 10 mol% and 20 mol% additions of tin fluoride lead to a suppression of the oxidation from $Sn^{2+}$ to $Sn^{4+}$ and furthermore, improve the film morphology of the perovskite absorber layer. Higher $SnF_2$ additions of 30 mol% and 40 mol% resulted in nano-platelet structures with a negative effect on the cell performance, mainly caused through a photocurrent drop.[63] Later, Lee et al. tried to add varying amounts of pyrazine to complex $SnF_2$ in the perovskite solution. With this additive they were able to produce highly efficient mesoscopic $FASnI_3$ perovskite solar cells with a PCE of 4.8% that were less prone to oxidation of $Sn^{2+}$ and therefore, showed good reproducibility and long term stability over 100 days when encapsulated.[64] In 2016, Liao et al. showed a $FASnI_3$ perovskite solar cell with an inverted cell set-up that reached power conversion efficiencies of 6.22%[65], which is still the highest PCE up to now for this cell type.

Like mentioned above, these tin-based perovskite solar cells often show problematic stability issues, due to their self-doping properties caused by the oxidation of $Sn^{2+}$ to $Sn^{4+}$. Especially, the addition of $SnF_2$ to the perovskite solution was a breakthrough in perovskite solar cell research and lead many different groups to explain the role of $SnF_2$ as additive in the perovskite absorber layer. Typically, $SnF_2$ can prevent the formation of Sn vacancies in perovskites caused by oxidation of $Sn^{2+}$ to $Sn^{4+}$, which would lead to unwanted p-type doping. This in turn, results in reduced background carrier density and higher resistance to charge recombination to overall improve the cell performance.[66,67] Other studies by Gupta et al. showed that $SnF_2$ is able to decrease the work function and the ionization potential of a $CsSnBr_3$ perovskite, which causes a shift of the valence band maximum closer to the HOMO level of the HTM and thus, a decrease in voltage losses in the cell.[66] But these are not the only properties like Xiao et al. demonstrated in 2017. Here, they showed that $SnF_2$ is able to create nucleuses for the crystal growth to obtain an improved uniformity of the thin film with high coverage.[68] Structural investigations

of $CsSnI_3$ by Kumar et al. provided that $SnF_2$ cannot be integrated into the perovskite structure but is uniformly distributed in the perovskite film.[58] Further improvements were achieved with an addition of pyrazine to the $SnF_2$ to obtain highly efficient cells with good reproducibilities and stabilities.[64] Not only $SnF_2$ but also other excess tin sources like $SnI_2$ and $SnCl_2$ were used to provide better cell performance, due to reduction of Sn vacancies and oxidation degree. Another approach to improve the cell performance was the usage of reducing agents like hydrazine or hypophosphorous acid.[62] Song et al. recently reported piperazine as reducing agent in $CsSnI_3$ perovskite solar cells, since it possesses a diamine character similar to hydrazine but is too bulky to be integrated into the perovskite structure. The diamine group is crucial for suppression of self-doping effects in perovskites.[69]

The engineering of the A-site cationic mixture has been demonstrated to be an effective possibility to adjust the properties and to improve the cell performance.[50] In 2017 Zhao et al. demonstrated an inverted mixed-organic-cation perovskite solar cell on tin basis that was capable to reach power conversion efficiencies of 8.12% and a very high open circuit voltage of 0.61 V. The perovskite consisted of $FA_xMA_{1-x}SnI_3$ (x = 0, 0.25, 0.50, 0.75, 1.0) with 10 mol% $SnF_2$ as additive, the best results were obtained with a cell set-up of "ITO/PEDOT:PSS/$FA_{0.75}MA_{0.25}SnI_3$/$C_{60}$/BCP/Ag". SEM investigations revealed that a lower content of $FA^+$ caused phase separation in the perovskite layer whereas, a higher content improved the thin film morphology greatly. It should be mentioned that a $SnF_2$ addition of 10 mol% resulted in an enhancement in grain size and thus, in an increase in performance. All higher $SnF_2$ additions caused a decrease in cell performance due to, phase separation and reappearing of pinholes.[70] However one year later, Liu et al. managed to outmatch this result with a nearly similar cell set-up (Al electrode instead of Ag) by application of solvent engineering, resulting in a PCE of 9.06%. While Zhao et al. used only DMSO as solvent for the perovskite precursor solution, Liu et al. were working with a mixture of DMF and DMSO also adding 10 mol% $SnF_2$. In both cases the solvent dripping step was carried out with chlorobenzene.[71] Another interesting approach was provided by Ke et al., who published a hollow MA{en} (en = ethylenediammonium) tin iodide solar cell with an efficiency of 6.63% and improved stability. In comparison to the pure $MASnI_3$ cell, the incorporation of the {en} caused an increase in $SnI_2$ vacancies and thus, a larger bandgap, larger unit cell volumes and much longer carrier lifetimes.[72] On the other hand, the same group worked on a hollow FA{en}$SnI_3$ perovskite using a new dopant-free tetrakis-triphenylamine (TPE) as hole transport layer in an mesoscopic cell set-up made of "FTO/m-$TiO_2$/FA{en}$SnI_3$/TPE/Au". TPE can be easily synthesized and is composed of a tetraphenylethene core with four endcapped triphenylamine units. Due to its intrinsic high hole mobility, a dopant is unnecessary and makes it a highly efficient and low-cost HTM. The absorber layer was capable to absorb over a wide wavelength range from 300 to 880 nm and was produced with 15 mol% $SnF_2$, providing a smooth and pinhole-less morphology to reduce charge recombination. All these improvements resulted in a PCE of 7.23%.[73] The 3D hollow perovskite structure, which develops when ethylenediammonium is integrated in the structure, was varied by Kanatzidis' group. They found out that propylenediammonium (PN) and trimethylenediammonium (TN), which are slightly bigger than

$FA^+$, can be integrated into the perovskite structure without changing the 3D dimensionality. For that experiment was used a normal set-up with "FTO/m-$TiO_2$/$FASnI_3$ with 10 mol% PN or TN/PTAA/Au". The perovskite was prepared with an addition of 10 mol% PN or TN and 15 mol% $SnF_2$ to a $FASnI_3$ precursor solution, resulting in nearly two-times higher efficiencies compared to pristine $FASnI_3$ solar cells. These additions lead to a better film morphology and reduce the trap-state density, the dark currents and the recombination of the devices.[74] Apart from that, researchers from Taiwan tried to integrate a nonpolar guanidinium cation ($GA^+$) into a $FASnI_3$ perovskite structure with 1% ethylenediammonium iodide ($EDAI_2$) and 10 % $SnF_2$ as additives. They were able to achieve power conversion efficiencies of 9.6 % with an inverted cell set-up, if a molar ratio of 20:80 ($GA^+$:$FA^+$) was used for the perovskite. XRD data showed that the $GA^+$ is inserted into the $FASnI_3$ lattice, resulting in larger unit cell parameters but still maintaining a 3D perovskite structure. With an increased GAI proportion, the energy levels of the valence bands began to shift downwards nearer to PEDOT:PSS (favoring larger $J_{SC}$) and the $E_g$ values increased (favoring larger $V_{OC}$). The little amount of $EDAI_2$ helped to control the kinetics of film formation and thus, produce a more uniform crystal size.[75]

All the devices above, described in this section, were based on a 3D perovskite structure that normally, provides better cell performance but also stability problems. Recently, 2D and mixed 2D/3D perovskite structures were found to be more stable towards humidity and light, show improved processability, long term durability and higher versatility compared to 3D structures. The most often used A-site cations for 2D perovskites are minimally branched aliphatic ammonium cations like for example phenylethylammonium (PEA) or butylammonium (BA). Typically, they can form different structures like a 2D layer, mixed 2D/3D perovskite phases, capping layers or passivated 3D perovskites. The growth of their layers is a crucial parameter to form highly efficient perovskites and was shown to be most efficient in a vertical alignment of the inorganic perovskite sheets to enable a good charge transport. However, most 2D structures are growing horizontal to the substrate and thus, show worse charge-transport. Furthermore, 2D structures have compared to the 3D ones, higher exciton binding energies, which means that excited electrons are more attracted to the holes and recombine more easily.[54]

The usage of $PEA^+$ cations was studied very intensively in the last years. Liao et al. studied a 3D $FASnI_3$ perovskite with 20% of PEA content and discovered that the organic PEA ligands have an encapsulating effect and thus, enhance the stability. SEM investigations showed that the obtained film was very smooth and dense, inhibiting the oxygen infiltration. Furthermore, they observed less diffraction peaks for the mixed perovskite compared to the pure $FASnI_3$ perovskite in the XRD, implying that the crystal grains have preferential orientations. GIWAX data provided that the $(10\bar{1})$ plane of the crystal grains grew parallel to the substrate surface. The best cell had an inverted cell set-up and a $PEA_2FA_8Sn_9I_{28}$ absorber layer that contained 10% $SnF_2$ as additive, resulting in 5.94% efficiency.[76] Even higher efficiencies of 9.0% were obtained by Shao et al., who used an inverted cell set-up of "ITO/PEDOT:PSS/Perovskite/$C_{60}$/BCP/Al". The perovskite solution was prepared from 0.08 M PEAI,

0.92 M FAI, 1 M $SnI_2$ and 0.1 M $SnF_2$ in a 4:1 mixture of DMF:DMSO. Moreover, also this report showed a high orientation of the 2D/3D perovskite crystal grains. They supposed that double layers of $SnI_6$ octahedra are separated by double layers of PEA molecules.[77] Like mentioned above, the two studies added a PEAI salt to the perovskite precursor solution resulting in a throughout layered 2D/3D perovskite structure. Recently, Chen et al. demonstrated the usage of PEABr as interlayer between a hole transport layer and a $FASnI_3$ perovskite. They supposed that only at the HTM/Perovskite interface a 2D/3D layered structure can be formed, while the upper part of the $FASnI_3$ perovskite remains in a 3D structure. The best cell achieved a PCE of 7.05% with an inverted solar cell set-up of "ITO/PEDOT:PSS/PEABr/$FASnI_3$/$C_{60}$/BCP/Cu". It should be mentioned that the high efficiency was most likely caused by an increase in $V_{OC}$ and $J_{SC}$, which can be explained by an improvement of the film morphology due to the introduction of the PEABr interlayer.[78] Table 1 summarizes a few important results of Sn-based PSCs.

**Table 1** *Most promising results of tin perovskite solar cells*

| **Perovskite** | **PCE [%]** | **FF [%]** | **$J_{SC}$ [mA*cm$^{-2}$]** | **$V_{OC}$ [V]** |
|---|---|---|---|---|
| $CsSnI_3$ | 4.81 | 49.05 | 25.71 | 0.382 |
| $MASnI_3$ | 6.4 | 42 | 16.8 | 0.88 |
| $FASnI_3$ | 6.22 | 60.67 | 22.07 | 0.465 |
| $FA_{0.8}GA_{0.2}SnI_3$ | 9.6 | 72.9 | 21.2 | 0.619 |
| 2D/3D | 9.0 | 71 | 24.1 | 0.525 |

The experimental procedure and idea behind this thesis were based on previous works and findings on tin halide PSCs by Jasmin Handl, Bastian Friesenbichler and Stefan Weber. Especially, the master theses of Bastian Friesenbichler[79], who investigated different A-site cations for $ASnI_3$ perovskites and of Jasmin Handl[80], who examined and optimized a triple cation tin iodide perovskite were used as basis. One of their most important works explored the properties of a triple cation methylammonium/formamidinium/phenylethylammonium tin iodide perovskite with the composition $MA_{0.75}FA_{0.15}PEA_{0.1}SnI_3$ and described possible ways to improve this system. Investigation of the perovskite layer preparation provided that a two times AS dripping step with chlorobenzene at 20 s and 80 s from a distance of approximately 4.5 cm, followed by a direct annealing step on the hot heating plate resulted in much better perovskite film morphology with smaller grains and less pinholes. Moreover, they investigated the electrical properties of this perovskite material in a "Glass-ITO/PEDOT:PSS/ $MA_{0.75}FA_{0.15}PEA_{0.1}SnI_3$/$PC_{60}$BM/Aluminium" set-up, resulting in PCEs up to 5%. Shelf-life tests of this cell provided very good results with only slight losses in performance after 5400 h storage and also very high stability under active load.[81] Furthermore, Weber et al. tried to do a partial substitution of iodide with bromide, resulting in the structure $MA_{0.75}FA_{0.15}PEA_{0.1}Sn(Br_xI_{3-x})$ with $x = 0 – 1$. With the introduction of bromide, the absorption onset provided a blueshift and consequently, an increase in $V_{OC}$. The best efficiencies were achieved with a bromide content of $x = 0.25$ and provided a PCE value of 4.63%.[82]

### *2.3.2.2 Germanium perovskite solar cells*

Germanium based perovskites are another interesting alternative to lead-based systems. It is located in the same group of the periodic table like Pb and Sn and therefore, also has a $ns^2$ configuration. Like described above, this configuration is very important to form a stable perovskite structure. In general, the s electrons of Ge are not stabilized as good as the ones of Pb, resulting in higher oxidation tendencies of $Ge^{2+}$ to $Ge^{4+}$ and this in turn, to metal-like conductivity and short circuits of the solar cell devices. The bandgaps of Ge perovskites are slightly higher than the ones of their Pb and Sn analogs (contrary to expectations), due to a very small ionic radius of $Ge^{2+}$, which causes $[GeI_6]^-$ octahedra distortion.[51,55,83] In 2015, Stoumpos et al. described different hybrid inorganic/organic germanium iodide perovskites as semiconducting materials. They investigated the bandgap energies and structures of $CsGeI_3$ ($E_g$ = 1.6 eV), $MAGeI_3$ ($E_g$ = 1.9 eV), $FAGeI_3$ ($E_g$ = 2.2 eV), $CH_3C(NH_2)_2GeI_3$ ($E_g$ = 2.5 eV), $(NH_2)_3GeI_3$ ($E_g$ = 2.7 eV), $(CH_3)_3NHGeI_3$ ($E_g$ = 2.5 eV) and $(CH_3)_2CHNH_3GeI_3$ ($E_g$ =2.8 eV) and found out that the first four structures resulted in a 3D perovskite structure, while the others formed 1D infinite chains. All 3D perovskite materials revealed a direct band transition and all 1D structures an indirect band transition.[84] In the same year, Krishnamoorthy et al. investigated the stabilities and performances of $CsGeI_3$, $MAGeI_3$ and $FAGeI_3$. All compounds were measured with thermogravimetric analysis (TGA) and showed thermal stability up to 150 °C, which is within the region of device working temperature. The obtained performances of the cells were relatively bad, due to poor perovskite film quality and high oxidation tendencies of Ge and poor solubility of these compounds in polar solvents. It was possible to reach power conversion efficiencies of 0.11% and 0.20% for $CsGeI_3$ and $MAGeI_3$ respectively.[85] However, further improvement of the PCE value was achieved by Kopacic et al., who produced an inverted methylammonium germanium halide perovskite solar cell with an efficiency of 0.68% by substitution of 10% iodide with bromide.[86] Up to now, the efficiencies of pure germanium halide perovskites are relatively low, therefore more interest was devoted to mixed Ge-Sn PSC. Recently, Chen et al. described a $CsSn_{0.5}Ge_{0.5}I_3$ PSC with an efficiency of 7.11% and very high stability through native-oxide passivation.[87] In table 2, the most important results of germanium halide PSCs are listed.

**Table 2** *Most promising results of germanium perovskite solar cells*

| **Perovskite** | **PCE [%]** | **FF [%]** | **$J_{SC}$ [mA*cm$^{-2}$]** | **$V_{OC}$ [V]** |
|---|---|---|---|---|
| $CsGeI_3$ | 0.11 | 27 | 5.7 | 0.074 |
| $MAGeI_3$ | 0.20 | 30 | 4.0 | 0.150 |
| $MAGeI_{2.7}Br_{0.3}$ | 0.68 | 48 | 3.11 | 0.46 |
| $CsSn_{0.5}Ge_{0.5}I_3$ | 7.11 | 60.6 | 18.61 | 0.63 |

### *2.3.2.3 Bismuth perovskite solar cells*

Since, Sn and Ge based PSC often show poor stability and reproducibility, Bi perovskites were of high interest over the last years. Bismuth can be found in the 15$^{th}$ group of the periodic table directly next to lead, resulting in very similar electronic configuration, electronegativity and ionic radius, which makes the material a promising alternative. Furthermore, Bi-compounds show higher chemical stability and lower toxicity compared to the lead analogs. In general, the perovskites of this element have the formula $A_3Bi_2X_9$, where A is a monovalent cation and X is a monovalent halide anion. It was found that the dimensionality (0D, 1D, 2D) of these materials is dependent on the halide anion and the size of the A cation (especially tunable with organic bulky cations).[88] Very early Park et al. demonstrated three different Bi halide PSC, which were composed of "Glass-FTO/compact-$TiO_2$/mesoscopic-$TiO_2$/Perovskite/HTM/Ag". For that purpose, $Cs_3Bi_2I_9$, $MA_3Bi_2I_9$ and $MA_3Bi_2I_9Cl_x$ were used as absorber layers and provided PCE values of 1.09%, 0.12% and 0.003% respectively.[89] Often the photoactive film quality is very poor, resulting in low PCE values. Therefore, Zhang et al. published a new two-step perovskite preparation method for $MA_3Bi_2I_9$ ($BiI_3$ was deposited in high-vacuum an is transformed to the perovskite in low-vacuum). This resulted in more uniform, compact, pinhole-free, large-grained films that were able to achieve a PCE of 1.64% (see table 3).[90] However, even better results were obtained for a $Cs_3Bi_2I_9$ PSC, using a "FTO/c-$TiO_2$/Perovskite/CuI/Au" cell structure. Bai et al. used a dissolution-recrystallization process to fabricate high quality ultra-thin perovskite nanosheets, resulting in an efficiency of 3.20% (see table 3), which is the best efficiency for bismuth halide PSCs in literature up to now. For the recrystallization a mixture of CsI and $BiI_3$ was dissolved in DMF, spin coated onto $TiO_2$ layer and annealed at 100 °C. Afterwards, a polar organic solvent made of DMF and $CH_3OH$ was dropped onto the perovskite film and annealed at 100 °C for 30 min.[91]

**Table 3** *Most promising results of bismuth perovskite solar cells*

| **Perovskite** | **PCE [%]** | **FF [%]** | **$J_{SC}$ [mA*cm$^{-2}$]** | **$V_{OC}$ [V]** |
|---|---|---|---|---|
| $MA_3Bi_2I_9$ | 1.64 | 69 | 2.95 | 0.81 |
| $Cs_3Bi_2I_9$ | 3.20 | 64.4 | 5.78 | 0.86 |

### *2.3.2.4 Antimony perovskite solar cells*

Antimony perovskites behave relatively similar to bismuth perovskites. With an electron configuration of $[Kr]4d^{10}5s^25p^3$, they have to lose three electrons to achieve a $5s^2$ configuration, which is necessary to form a perovskite structure. Since, $Sb^{3+}$ cannot form an $ABX_3$ structure, an alternative $A_3B_2X_9$ structure (like observed for bismuth) is formed. Typically those perovskites form either a hexagonal phase consisting of 0D bioctahedral face-sharing $(M_2I_9)^{3-}$ clusters or 2D corrugated layers with partially corner-sharing $MX_6$ octahedra.[92] In 2017, Boopathi et al. demonstrated the two perovskite materials $MA_3Sb_2I_9$ ($E_g$ = 1.95 eV) and $Cs_3Sb_2I_9$ ($E_g$ = 2.0 eV) as absorber layers in an inverted cell set-up made of "Glass-ITO/PEDOT:PSS/Sb-perovskite/$PC_{71}BM$/$C_{60}$/BCP/Al". They varied the molar ratios of $SbI_3$:MAI/CsI to investigate the film morphology and the impact on the cell performance, the best ratios were 0.5:1 ($SbI_3$:MAI) and 0.2:1 ($SbI_3$:CsI), resulting in smooth film morphology and highest PCE values of 2.04% and 0.84% respectively. Furthermore, it was found that the addition of HI was crucial for an appropriate cell performance.[93] Moreover, the work of Correa-Baena et al. provided further results for all inorganic antimony based PSC comprising $Cs_3Sb_2I_9$ (0D), $Rb_3Sb_2I_9$ (2D) and $K_3Sb_2I_9$ (2D). The best results were obtained with the rubidium Sb perovskite, which achieved a PCE value of 0.76%.[94] However, the most promising results for Sb perovskites were obtained by Adonin et al., who synthesized a N-ethylpyridinium bromoantimonate complex ((N-EtPy)[$SbBr_6$]) , which forms $ABX_6$ compounds that are comparable to conventional $ABX_3$ structures. With this new approach they were able to fabricate PSCs composed of "ITO/c-$TiO_x$/bromoantimonate/P3HT/Au", resulting in a record PCE of 3.8%.[95] Table 4 represents the most promising results of antimony perovskites.

**Table 4** *Most promising results of antimony perovskite solar cells*

| **Perovskite** | **PCE [%]** | **FF [%]** | **$J_{SC}$ [mA*cm$^{-2}$]** | **$V_{OC}$ [V]** |
|---|---|---|---|---|
| $MA_3Sb_2I_9$ | 2.04 | 60.82 | 5.41 | 0.62 |
| $Cs_3Sb_2I_9$ | 0.84 | 48.11 | 2.91 | 0.60 |
| $Rb_3Sb_2I_9$ | 0.76 | 63 | 1.84 | 0.66 |
| (N-EtPy)[$SbBr_6$] | 3.8 | 58 | 5.1 | 1.29 |

# 3 Results and Discussion

In this chapter, all important results of the investigated tin-based perovskite solar cells are described. The fabricated system shows a set-up of "Glass-ITO/PEDOT:PSS/Sn-perovskite/$PC_{60}BM$/Aluminium". During this work, the A-cationic composition of an $ABX_3$ perovskite absorber layer was varied and further improved.

## 3.1 Optical characterization of the perovskite systems

In this section, the optical properties of all investigated perovskite systems are discussed. This comprises absorption spectra, which were measured by UV-VIS spectroscopy as well as profilometry measurements to enable a calculation of the bandgap energy of the absorber materials.

The UV-VIS samples were prepared on glass substrates coated with PEDOT:PSS to provide the same underground for the perovskite layer like in the solar cell set-up. The perovskite layer was produced by spin coating of the respective perovskite precursor solution and two times AS dripping at 10 s and 70 s, followed by a 70 °C annealing step like described in the experimental section. The absorption of the substrates was corrected by the absorption of PEDOT:PSS on glass.

With the absorption data it was possible to calculate the absorption coefficient of the material. The absorption coefficient can be derived from Beer-Lambert Law shown in formula 5. Here, $I_0$ is the incoming light intensity, I the intensity of the transmitted light, α the absorption coefficient and d the layer thickness of the thin film.

$$I = I_0 * e^{-\alpha * d} \qquad \textit{(Formula 5)}$$

By transforming the equation and using the natural logarithm the equation changes to formula 6.

$$-\ln\frac{I}{I_0} = \alpha * d \qquad \textit{(Formula 6)}$$

To calculate the absorption coefficient, it is necessary to transform the natural logarithm into the common logarithm which has the base 10. Therefore, a conversion factor of 2.303 must be used (see formula 7).

$$2.303 * log\frac{I_0}{I} = \alpha * d \qquad \textit{(Formula 7)}$$

Since $log\frac{I_0}{I}$ equates to the value of the measured absorption (Abs), the formula changes to formula 8, which shows the final equation that was used for the calculation of the absorption coefficient α.

$$\alpha\ [cm^{-1}] = \frac{2.303 * Abs\ [1]}{d\ [cm]} \qquad \textit{(Formula 8)}$$

The determination of the absorption coefficient can be used for further calculations to determine the band gap energy $E_g$ of the material. For materials with a direct band gap transition the band gap energy can be determined by plotting $(\alpha h\upsilon)^2$ against the photon energy $h\upsilon$.

Formula 9 shows the calculation for the Tauc plot.

$$(\alpha h\upsilon)^2[cm^{-2} * (eV)^2] = \left( \alpha\,[cm^{-1}] * \left( \frac{6.626 * 10^{-34}[J * s] * \frac{2.998 * 10^8\,[m * s^{-1}]}{\lambda\,[m]}}{1.602 * 10^{-19}} \right) \right)^2 \qquad \textit{(Formula 9)}$$

The received curve shows a linear steep slope in the beginning of the course of the curve, which is used for extrapolation. The intersection of the linear line with the x-axis provides the band gap energy $E_g$.

### 3.1.1 Single cation Sn-perovskites

Three different single A-site tin perovskites have been investigated in detail. These three systems comprise a $FASnI_3$, a $CsSnI_3$ as well as a $RbSnI_3$ perovskite. Figure 9 A-C shows their absorption behavior.

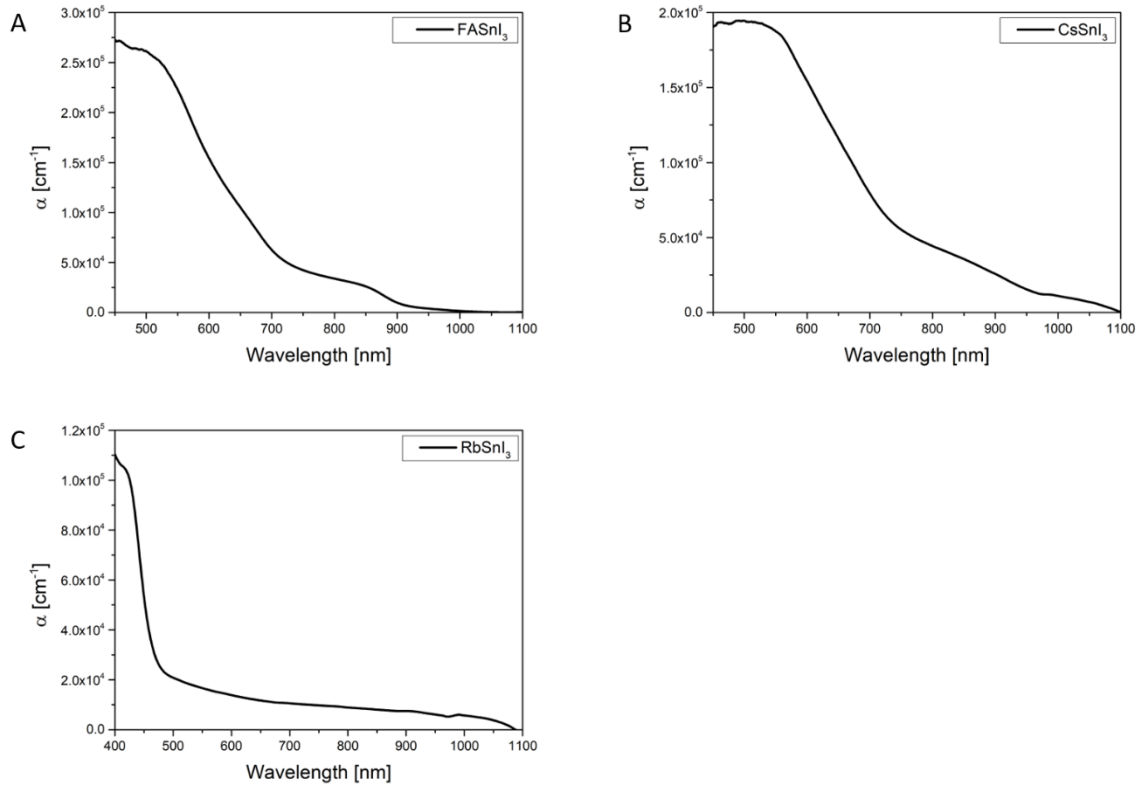


**Figure 9** *Absorption spectra of* ***(A)*** *$FASnI_3$,* ***(B)*** *$CsSnI_3$ and* ***(C)*** *$RbSnI_3$*

The absorption spectra show, that the two perovskites $FASnI_3$ and $CsSnI_3$ absorb light over a wide wavelength range from the optical spectrum. This is in accordance with the observation of a black color of the absorber layer. In the UV-VIS spectrum of $FASnI_3$ a steep onset at approximately 900 nm can be seen, this region is used for the calculation of the bandgap. $CsSnI_3$ showed the onset at 960 nm. $RbSnI_3$ behaves differently and absorbs especially in a wavelength region between 400 to 450 nm, corresponding to the absorbance of blue light. This result was to be expected, since the absorber layer showed the complementary color yellow. The material shows a steep onset at approximately 460 nm, resulting in a high band gap energy.

Using these results, it was possible to draw the Tauc plots of these materials and determine the bandgap energies (see figure 10). The results of the calculated bandgaps in comparison with literature values are summarized in table 5.

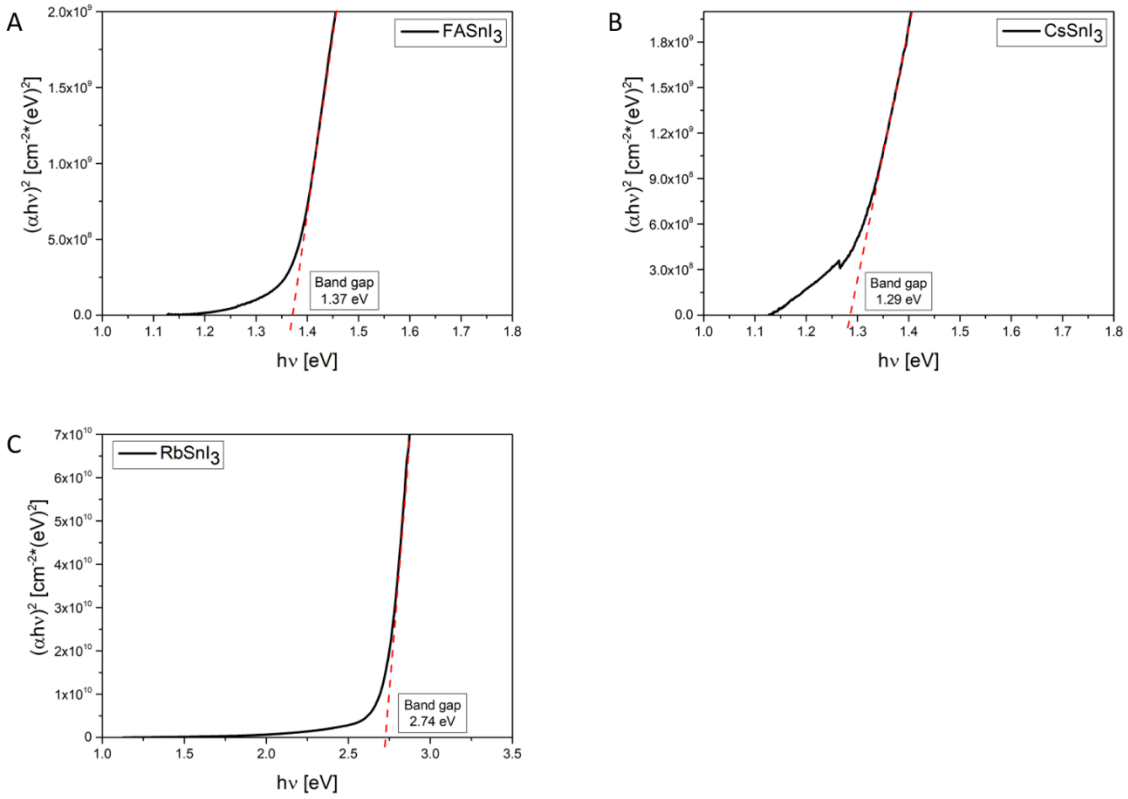


**Figure 10** *Tauc plots of the single cation Sn-perovskites for the calculation of the band gap energy $E_g$.* ***(A)*** *$FASnI_3$,* ***(B)*** *$CsSnI_3$ and* ***(C)*** *$RbSnI_3$*

All three materials show most probably a direct band transition. Therefore, the values of $(\alpha h\upsilon)^2$ are shown on the y-axis. $FASnI_3$ shows a bandgap of approximately 1.37 eV which matches relatively good with the values of 1.35 eV – 1.41 eV found in literature[96,97]. The bandgap of $CsSnI_3$ shows a value of 1.29 eV, which is also in accordance with literature[53] for the black B-γ $CsSnI_3$. For $RbSnI_3$ the bandgap is comparatively high. Materials with a higher bandgap require light with smaller wavelengths for the excitation of electrons from the valence band into the conduction band. The calculated bandgap of

2.74 eV makes sense, since $RbSnI_3$ shows a high absorbance in the blue region of the spectrum (smaller wavelengths). In literature[98] $RbSnI_3$ is also described as a yellow crystal structure, which confirmed the obtained results.

**Table 5** *Band gap energies $E_g$ of $FASnI_3$, $CsSnI_3$ and $RbSnI_3$*

| Perovskite | $E_g$ measured | $E_g$ Literature[53,96,97] |
|---|---|---|
| $FASnI_3$ | 1.37 | 1.35 – 1.41 |
| $CsSnI_3$ | 1.29 | 1.30 |
| $RbSnI_3$ | 2.74 | - |

### 3.1.2 Double cation Sn-perovskites

The double cationic Sn-perovskites were based on a $FASnI_3$ system with varying amounts of piperazine-1,4-diium iodide ($PIPI_2$) or hexylammonium iodide (HAI). Here the UV-VIS spectra and determined bandgap energies of the best tested concentrations, according to their efficiencies, for these double cationic mixtures are shown. In figure 11 the absorption spectra of $FASnI_3$, $FA_{0.95}HA_{0.05}I_3$ and $FA_{0.98}PIP_{0.02}SnI_3$ are depicted. Other double cationic Sn-perovskites percentages can be found in the appendix.

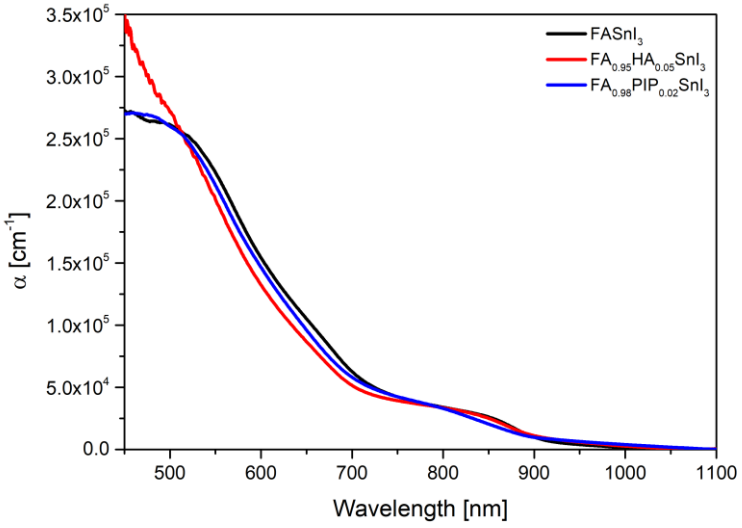


**Figure 11** *Absorption spectra of the $FASnI_3$ reference and the double cation perovskites $FA_{0.95}HA_{0.05}SnI_3$ and $FA_{0.98}PIP_{0.02}SnI_3$.*

Both materials show absorption over a wide wavelength range like it can be observed for the pure $FASnI_3$ perovskite reference. The curves look relatively similar to the reference, but slight differences occur for the piperazine-1,4-diium iodide sample regarding the observed onset, which looks less steep compared to the other samples. The absorption of the hexylammonium absorber layer seems to be a little

bit shifted to smaller wavelengths, without changing the position of the first onset at approximately 900 nm. However, the absorption behavior of this curve at values above $2.5*10^5$ $cm^{-1}$ seems unrealistic and should show most probably a similar curve progression like the other two samples.

The next graphs 12A and 12B show the determined bandgap energies of the double cationic Sn-perovskites, assuming that they also show a dominant direct band transition like the $FASnI_3$.

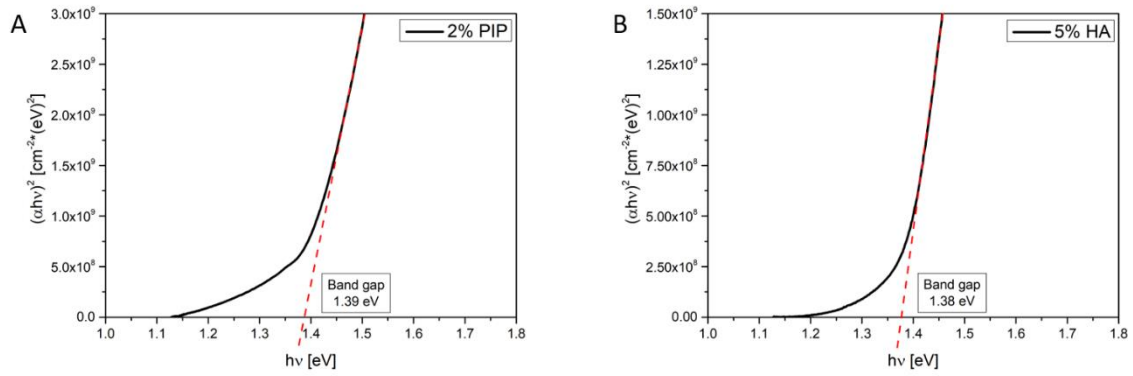


**Figure 12** *Tauc plots of the double cation Sn-perovskites for the calculation of the band gap energy $E_g$.* ***(A)*** *$FA_{0.98}PIP_{0.02}SnI_3$ and* ***(B)*** *$FA_{0.95}HA_{0.05}SnI_3$*

Like in the $FASnI_3$, the onset of all mixtures can be found at approximately 900 nm. Also, here a direct allowed band transition was supposed for the calculation of the Tauc plots, due to the very similar absorption behavior and the high percentage of formamidinium iodide present in the double cation Sn-perovskites. The determined bandgap energies of $FA_{0.98}PIP_{0.02}SnI_3$ (1.39 eV) and $FA_{0.95}HA_{0.05}I_3$ (1.38 eV) are relatively similar but slightly higher than the one of the pure $FASnI_3$ perovskite (1.37 eV). Higher concentrations of piperazine-1,4-diium in the perovskite structure showed a shift of the bandgap energy to higher energies and consequently lower wavelengths.

Since literature so far did not provide any data for these materials it was impossible to compare the results with literature values.

## 3.2 XRD analysis of the perovskite layers

The following chapter focusses on the XRD patterns of the most important investigated perovskite systems. This comprises the single cation Sn-perovskites of $FASnI_3$, $CsSnI_3$ and $RbSnI_3$ and the double cationic Sn-perovskites of $FA_{0.98}PIP_{0.02}SnI_3$ and $FA_{0.95}HA_{0.05}SnI_3$. All perovskite thin films were produced directly on cleaned glass substrates to prevent reflexes caused by ITO or PEDOT:PSS. The absorber layers were produced by spin coating 50 µL of the respective perovskite precursor solution and two times AS dripping at 10 s and 70 s and annealing at 70 °C for 20 min.

### 3.2.1 Single cation Sn-perovskites

This section deals with the structural investigation of the examined single cation perovskites $FASnI_3$, $CsSnI_3$ and $RbSnI_3$.

#### *3.2.1.1 $FASnI_3$*

In figure 13 the XRD pattern of the pure $FASnI_3$ is shown. The measured reflexes were allocated by comparison with the work of Liao et al. on $FASnI_3$. The numbers above the reflexes represent the lattice planes of the crystal.[65]

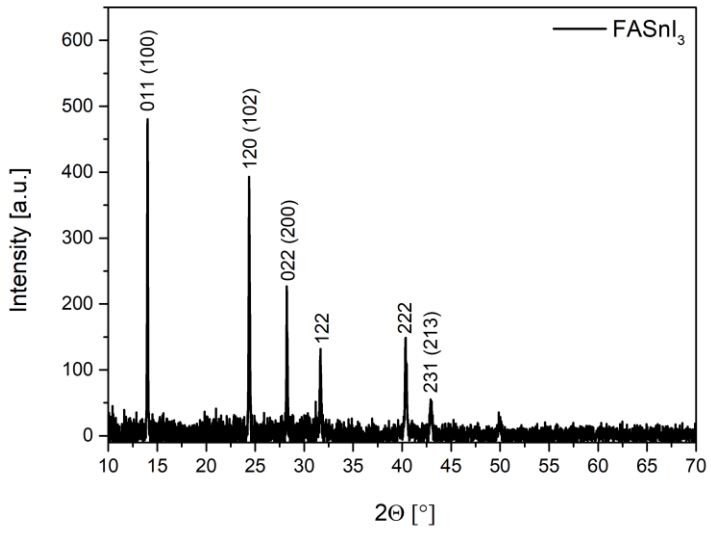


**Figure 13** *Diffractogram of $FASnI_3$. The respective lattice planes of the reflexes were taken from literature 65.*

This diffractogram is in accordance with the data found in literature. The reflexes indicate that the $FASnI_3$ perovskite shows an orthorhombic structure like also expected before. Dominant reflexes at 14°, 24.3°, 28.1°, 31.7°, 40.4° and 42.9° can be observed.

### *3.2.1.2 $CsSnI_3$*

Figure 14 shows the XRD pattern of a $CsSnI_3$ thin film. Smaller peaks between 25.5° and 30° are shown in a higher magnification in the right upper corner of the graph.

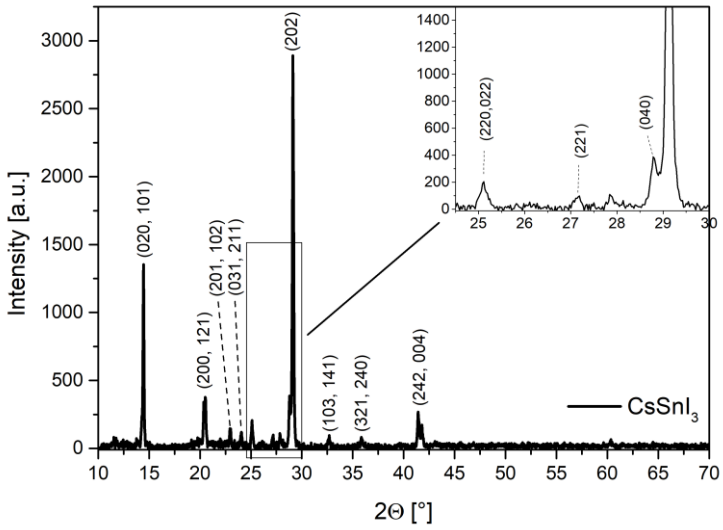


**Figure 14** *XRD of $CsSnI_3$. The respective lattice planes of the reflexes were taken from literature 99.*

Comparison with a literature diffractogram of $CsSnI_3$ suggest that the produced perovskite structure shows the orthorhombic B-γ-$CsSnI_3$ polymorph. This is in accordance with other observations like the black color of the perovskite thin film. The lattice planes for the measured reflexes were taken from literature values.[99] This sample shows the most intense reflexes at 14.4°, 20.5° and 29.1°.

### *3.2.1.3 $RbSnI_3$*

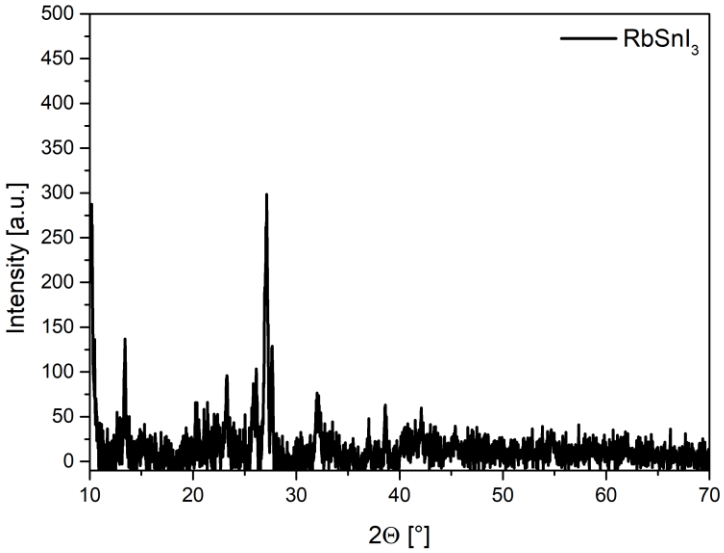


**Figure 15** *XRD of $RbSnI_3$*

Figure 15 shows the diffractogram of $RbSnI_3$. It can be seen, that the sample shows a high background noise that makes it difficult to determine smaller reflexes. The most dominant reflexes are at 10°, 13.4°, 23.3°, 27.1° and 32°.

The $RbSnI_3$ sample showed a citric yellow color of the perovskite layer. This is in accordance with literature, where the $RbSnI_3$ is always described as a yellow 1D crystal structure.[98]

### 3.2.2 Double cation Sn-perovskites

Graph 16 shows a comparison of $FASnI_3$, $FA_{0.98}PIP_{0.02}SnI_3$ and $FA_{0.95}HA_{0.95}SnI_3$. For a better visibility, the diffractograms of the compounds are pictured stacked.

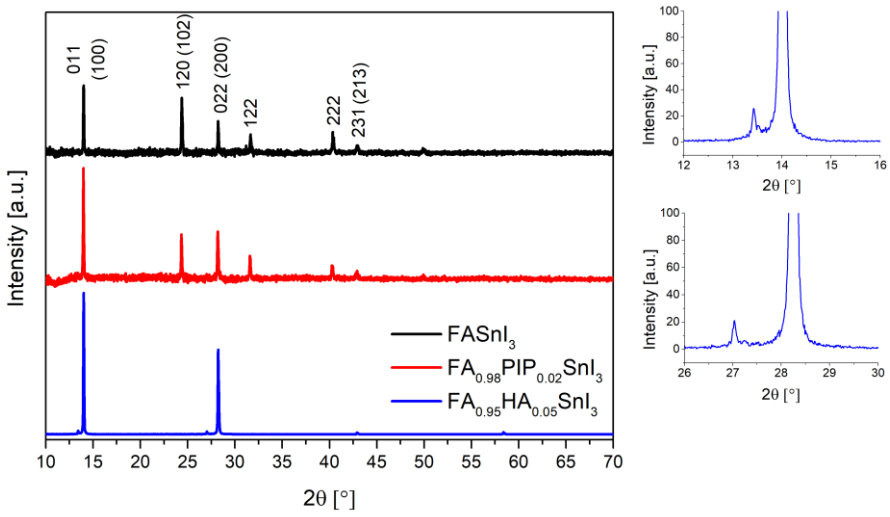


**Figure 16** *Stacked presentation of the XRD data of the double cation perovskites in comparison with $FASnI_3$. The two smaller graphs on the right side show a magnification of two main peaks of the $FA_{0.95}HA_{0.05}SnI_3$.*

The diffractogram at the top shows a $FASnI_3$ perovskite system.[65] Like it can be seen in the XRD patterns, the piperazine-1,4-diium sample looks relatively similar to the reference formamidinium cell. Therefore, it was difficult to see an evidence that piperazine-1,4-diium iodide was integrated into the perovskite structure.

However, the hexylammonium sample shows a different XRD pattern compared to the other samples. The reflexes at approximately 13.4°, 14°, 27° and 28.3° match with the XRD pattern of a formamidinium phenylethylammonium Sn-perovskite that shows typically a mixed 2D/3D perovskite structure like described in literature. These similarities in the diffractograms suggest that also the hexylammonium sample shows a mixed 2D/3D layered structure.[76,78] Due to the absence of other peaks and very dominant reflexes at the mentioned angles, it can be suggested that the perovskite crystals grow into preferred directions. Liao et al. investigated a $FASnI_3$ perovskite with additions of 20% PEAI, which resulted in

an orthorhombic crystal structure with lattice planes into the $(10\bar{1})$ and $(10\bar{2})$ direction, which correspond to the two peaks at ~14° and ~28° respectively. From XRD data, they supposed preferred orientation of the perovskite crystals and investigated this in more detail with GIWAX measurements. The perovskite showed very sharp and discrete Bragg spots, indicating high orientation of the $(10\bar{1})$ plane parallel to the substrate.[76] These results enable the suggestion that also the HA sample shows this parallel orientation to the substrate.

## 3.3 Improvement of the $FASnI_3$ reference system by variations in the perovskite film formation

During this work it was important to find and investigate a relatively stable and especially reliable reference system as well as a good basis material for A-site cationic mixtures. $FASnI_3$ seemed to be a relevant candidate for that purpose. In this part different experiments are discussed, which were used to improve the reference system. This comprises the antisolvent dripping times, the investigated film thicknesses of the absorber layer, the temperature influence and the annealing times of the perovskite layer.

### 3.3.1 Antisolvent dripping times

An AS can be very helpful for the formation of homogeneous perovskite thin films. The AS causes a reduction in solubility of the dissolved compound and induces the crystallization of the perovskite layer.[100] Since the antisolvent dripping is a very crucial step in the production of the solar cell, this process was improved using different AS dripping times. In this experiment, the solar cells were fabricated on cleaned glass-ITO substrates with PEDOT:PSS as HTL and $PC_{60}BM$ as ETL. The perovskite absorber layer was made by spin coating of 50 µL of the perovskite precursor solution for two minutes and meanwhile, two times AS dripping at different moments. It should be mentioned that also the dripping height and the dripping velocity of the AS are important during the fabrication process and must be controlled. Therefore, the AS was always dripped onto the surface relatively fast from approximately 4.5 cm distance. Figure 17 and Table 6 show the measured JV-curves and the most important results of the different AS dripping times (solar cells had an area of 0.09 $cm^2$ and were measured without mask)

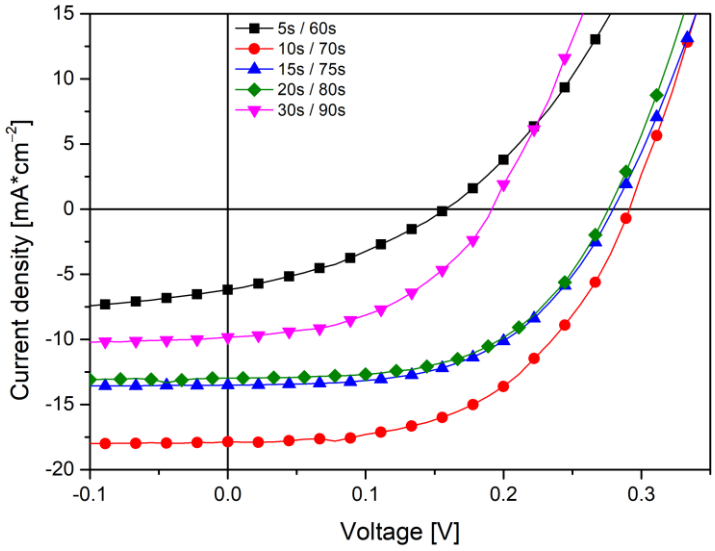


**Figure 17** *JV-measurement: Investigation of the antisolvent dripping times during perovskite thin film production.*

**Table 6** *Results of the antisolvent dripping investigation. The mean values and standard deviations were calculated from the best 5 solar cells.*

| **Substrate** | | **PCE [%]** | **FF [%]** | **$J_{SC}$ [mA*cm$^{-2}$]** | **$V_{OC}$ [V]** |
|---|---|---|---|---|---|
| **5 s / 65 s** | Mean | 0.28 ± 0.04 | 32.2 ± 1.6 | -6.0 ± 0.3 | 0.14 ± 0.01 |
| | Best | 0.33 | 34.5 | -6.2 | 0.16 |
| **10 s / 70 s** | Mean | 2.34 ± 0.23 | 51.8 ± 0.7 | -16.13 ± 1.1 | 0.28 ± 0.01 |
| | Best | 2.69 | 52.8 | -17.9 | 0.29 |
| **15 s / 75 s** | Mean | 1.93 ± 0.08 | 53.0 ± 1.8 | -13.3 ± 0.28 | 0.28 ± 0.01 |
| | Best | 2.01 | 54.4 | -13.5 | 0.28 |
| **20 s / 80 s** | Mean | 1.80 ± 0.19 | 55.7 ± 0.8 | -11.7 ± 1.08 | 0.27 ± 0.01 |
| | Best | 2.01 | 55.2 | -13.0 | 0.28 |
| **30 s / 90 s** | Mean | 0.82 ± 0.04 | 45.2 ± 1.3 | -9.8 ± 0.3 | 0.19 ± 0.01 |
| | Best | 0.86 | 46.8 | -9.8 | 0.19 |

The best results were achieved with two times chlorobenzene antisolvent dripping at 10 s and 70 s. The best cell showed a PCE value of 2.69%, a fill factor of 52.8%, a current density of -17.9 mA*cm$^{-2}$ and an open circuit voltage of 0.29 V. In general, significant differences were observed macroscopically between the surfaces depending on the moments of antisolvent dripping. Substrates, which were produced with AS dripping at 5 s/60 s and 30 s/90 s looked relatively grey and dull, while the substrates between 10 s/70 s and 20 s/80 s showed black reflective surfaces of the absorber layer. These observations are in accordance with the results listed in table 6, confirming that reflective surfaces are often attended by an improved cell performance. Based on these results all further experiments were carried out with an AS dripping at 10 s and 70 s.

### 3.3.2 Hot antisolvent dripping

Liu and co-workers provided new promising results concerning hot AS dripping. The usage of the hot AS should have a positive influence of the perovskite thin film formation during spin coating and consequently, the perovskite film should show less pinholes.[101] Therefore, the substrates were prepared like described in the experimental part and PEDOT:PSS was spin coated as hole transport layer. The perovskite layer was produced with hot AS dripping using chlorobenzene at 70 °C at 10 s and 70 s. Afterwards, $PC_{60}BM$ as ETL and the aluminium electrodes were applied. Figure 18 and table 7 show the results of this experiment (solar cells had an area of 0.09 cm$^2$ and were measured without mask).

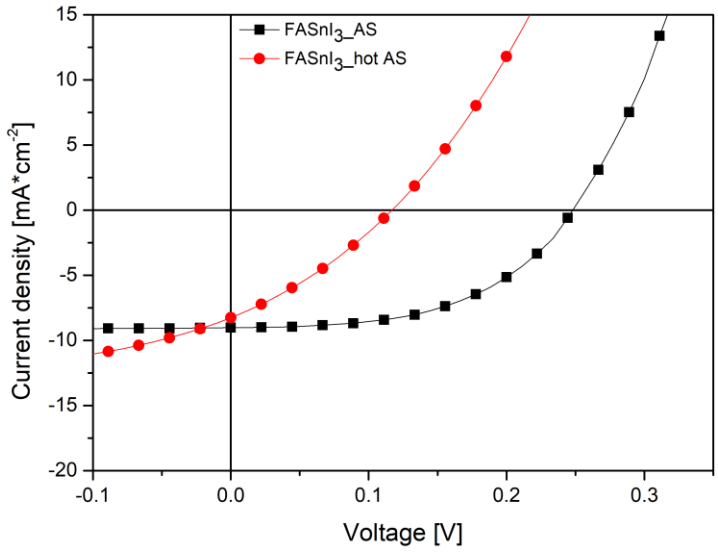


**Figure 18** *JV-measurement: Investigation of hot antisolvent dripping compared to the normal procedure with antisolvent at RT.*

**Table 7** *Results of the hot AS dripping and the AS dripping at RT. The mean values and standard deviations were calculated from the best 5 solar cells.*

| Substrate | | PCE [%] | FF [%] | $J_{SC}$ [mA*cm$^{-2}$] | $V_{OC}$ [V] |
|---|---|---|---|---|---|
| **AS at RT** | Mean | 1.08 ± 0.04 | 49.6 ± 4.5 | -9.0 ± 0.8 | 0.25 ± 0 |
| **Reference** | Best | 1.13 | 52.6 | -9.0 | 0.24 |
| **Hot AS** | Mean | 0.28 ± 0.01 | 30.6 ± 0.9 | -7.9 ± 0.4 | 0.12 ± 0.01 |
| | Best | 0.30 | 29.6 | -8.3 | 0.12 |

The AS dripping with the heated chlorobenzene provided worse results compared to the normal AS dripping with solvent at RT conditions. It can be seen, that the hot antisolvent curve runs relatively steep compared to the normal procedure, which leads to a much lower open circuit voltage. Furthermore, also the fill factor is worse and decreased from 52.6% to 29.6% for the best obtained solar cells. Although, the results were relatively bad compared to the reference, hot AS seems to have potential for the preparation of perovskite absorber layers. Therefore, it is worth to be further investigated in the future.

### 3.3.3 Hot substrate spinning

Since, the antisolvent dripping step is very complex and varies often for different materials, it was also tested hot substrate spinning at 70°C without any AS. Therefore, the glass-ITO substrates were prepared as usual and spin coated with PEDOT:PSS. Afterwards, the perovskite layer was applied. For that purpose, 50 µL of the precursor solution were spin coated for two minutes without any AS addition. The JV-measurements of these films provided short circuits. The reason for the short circuits can be seen in the light microscope images of the $FASnI_3$ films, which were produced with AS (figure 19A) and without AS (figure 19B).

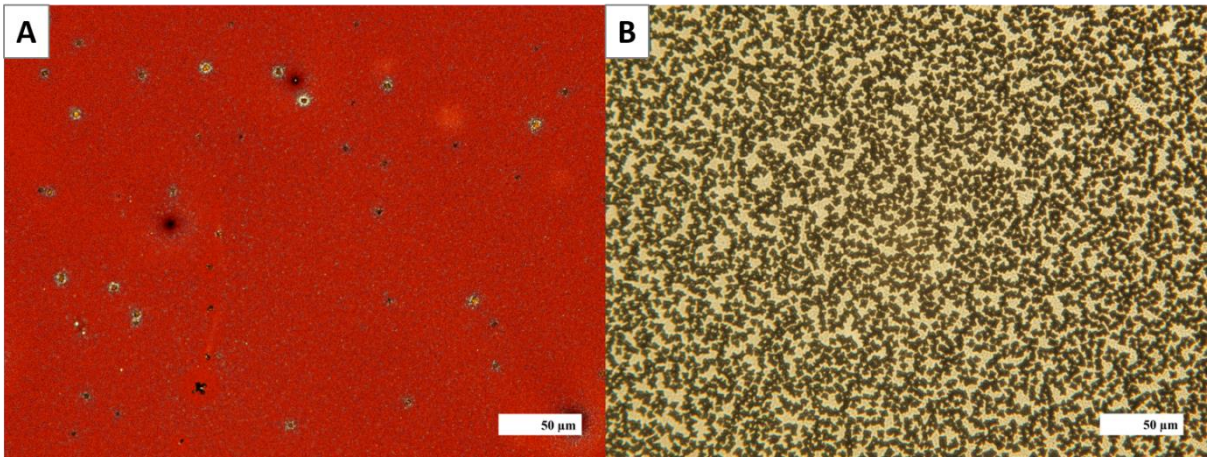


**Figure 19** *Comparison between the perovskite film formation with antisolvent dripping (A) and hot substrate spinning (B) with a magnification of 400 times.*

The $FASnI_3$ film, produced with AS dripping is pictured in figure 19A and shows a relatively homogeneous surface with a few larger black crystals. In figure 19B can be seen that the perovskite film, which was produced without AS shows many black single crystals and large pinholes. As a consequence, it was possible that the hole transport layer and the electron transport layer come into contact with each other and this in turn caused short circuits in the solar cell.

### 3.3.4 Investigation of the different perovskite layer thicknesses

In this subchapter different thicknesses of the $FASnI_3$ absorber layer are discussed. All cells were fabricated on glass-ITO substrates with PEDOT:PSS as HTL and $PC_{60}BM$ as ETL. For the production of the absorber layer were used spin coating parameters between 1000 rpm and 8000 rpm with an acceleration of 2000 rpm*$s^{-1}$ and AS dripping at 10 s and 70 s. Figure 20 shows the best JV-curves of the different tested film thicknesses of the absorber layer. The measured film thicknesses and the corresponding results of the JV-measurements are shown in table 8 and 9.

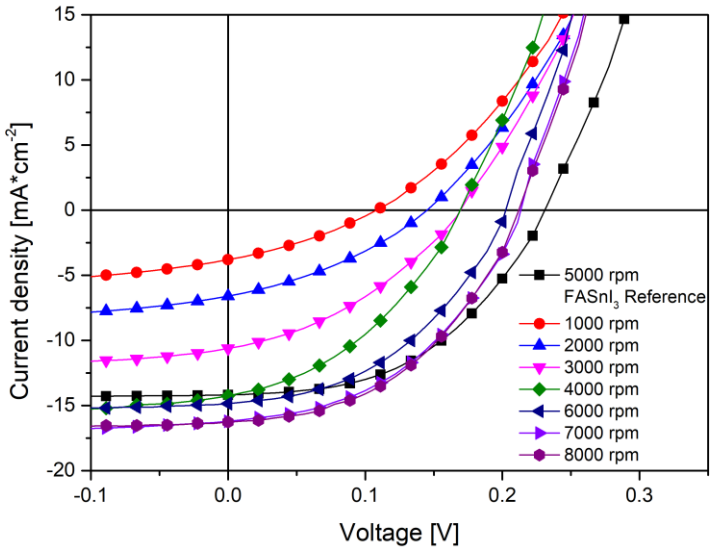


**Figure 20** *JV-measurement: Investigation of the influence of the layer thickness on the cell performance.*

**Table 8** *Rotation speeds of the spin coater and resulting layer thicknesses of the perovskite film*

| Speed [rpm] | Layer thickness [nm] |
|---|---|
| 1000 | 283 nm ± 52 nm |
| 2000 | 283 nm ± 27 nm |
| 3000 | 287 nm ± 12 nm |
| 4000 | 260 nm ± 3 nm |
| 5000 | 242 nm ± 5 nm |
| 6000 | 208 nm ± 29 nm |
| 7000 | 200 nm ± 29 nm |
| 8000 | 180 nm ± 31 nm |

**Table 9** *Results of the solar cells with different film thicknesses. The mean values and standard deviations were calculated from the 5 best solar cells.*

| Substrate | | PCE [%] | FF [%] | $J_{SC}$ [mA*cm$^{-2}$] | $V_{OC}$ [V] |
|---|---|---|---|---|---|
| **1000 rpm** | Mean | 0.11 ± 0.02 | 32.0 ± 0.9 | -3.23 ± 0.39 | 0.11 ± 0.01 |
| | Best | 0.13 | 31.1 | -3.8 | 0.11 |
| **2000 rpm** | Mean | 0.16 ± 0.10 | 32.1 ± 1.9 | -4.3 ± 1.3 | 0.11 ± 0.02 |
| | Best | 0.33 | 34.6 | -6.6 | 0.14 |
| **3000 rpm** | Mean | 0.55 ± 0.09 | 36.0 ± 1.2 | -10.3 ± 0.6 | 0.15 ± 0.01 |
| | Best | 0.66 | 37.6 | -10.6 | 0.14 |
| **4000 rpm** | Mean | 0.78 ± 0.11 | 39.0 ± 0.7 | -12.7 ± 1.0 | 0.16 ± 0.01 |
| | Best | 0.94 | 40.1 | -14.3 | 0.17 |
| **5000 rpm** | Mean | 1.47 ± 0.07 | 47.6 ± 0.8 | -13.6 ± 0.5 | 0.23 ± 0.01 |
| | Best | 1.56 | 47.4 | -14.2 | 0.23 |
| **6000 rpm** | Mean | 1.17 ± 0.07 | 45.8 ± 1.0 | -13.8 ± 0.7 | 0.19 ± 0.0 |
| | Best | 1.28 | 44.9 | -14.9 | 0.20 |
| **7000 rpm** | Mean | 1.46 ± 0.06 | 45.9 ± 0.7 | -15.3 ± 0.5 | 0.21 ± 0.00 |
| | Best | 1.55 | 45.6 | -16.2 | 0.21 |
| **8000 rpm** | Mean | 1.42 ± 0.16 | 46.6 ± 1.2 | -15.2 ± 1.0 | 0.20 ± 0.01 |
| | Best | 1.57 | 46.2 | -16.3 | 0.21 |

It can be seen, that spin coating parameters below 5000 rpm worked definitely worse compared to higher spin coating speeds. The best cells were gained with spin coating speeds from 5000 rpm to 8000 rpm. The layer thicknesses for these cells range from 242 nm to 180 nm. There were no big differences in the solar cell performance of these four cells. The reference showed higher $V_{OC}$ values, while the cells spin coated at 7000 and 8000 rpm showed higher current densities. Comparing the hysteresis behavior of the curves it can be observed that the 6000, 7000 and 8000 rpm samples show slightly more hysteresis than the reference cell with 5000 rpm. The corresponding hysteresis graphs can be found in the appendix.

## 3.4 Cesium tin iodide and rubidium tin iodide

Since, $FASnI_3$ was often influenced very much by the surrounding conditions also other single A-site cation Sn-perovskites were tested. Therefore, $CsSnI_3$ and $RbSnI_3$ were taken into consideration.

The solar cells showed the same solar cell set-up as described in the experimental part. The perovskite solutions of these compounds were prepared the same way as $FASnI_3$ with a molar ratio of CsI and RbI to $SnI_2$ of 1:1. During the preparation of the perovskite layers it was observable that CsI and RbI were not crystallizing at once when AS was dripped onto the surface. Both compounds crystallized 30 s to one minute later after placing them on the heating plate at 70°C. Cesium tin iodide formed a black perovskite layer with a light blue haze, whereas $RbSnI_3$ formed a yellow perovskite phase. An increase in temperature during the annealing step could not influence the crystal structure of $RbSnI_3$, JV-measurement of this compound showed no results. Therefore, only $CsSnI_3$ was used in further experiments.

### 3.4.1 Investigation of $CsSnI_3$

Since, $CsSnI_3$ did not crystallize during the spin coating step with chlorobenzene, also other antisolvents like diethylether and toluene were used in the hope that they would provide a different crystallization behavior. In this experiment the AS dripping was carried out the same way as for the $FASnI_3$ reference with spin coating of 50 µL of the perovskite precursor solution and two times AS dripping at 10 s and 70 s. The following graph shows only the results of the solutions and antisolvents, which were not dried with molecular sieves. All results with solvents, which were dried additionally, with molecular sieves provided worse results and are not shown here. In figure 21 and table 10 the results are demonstrated.

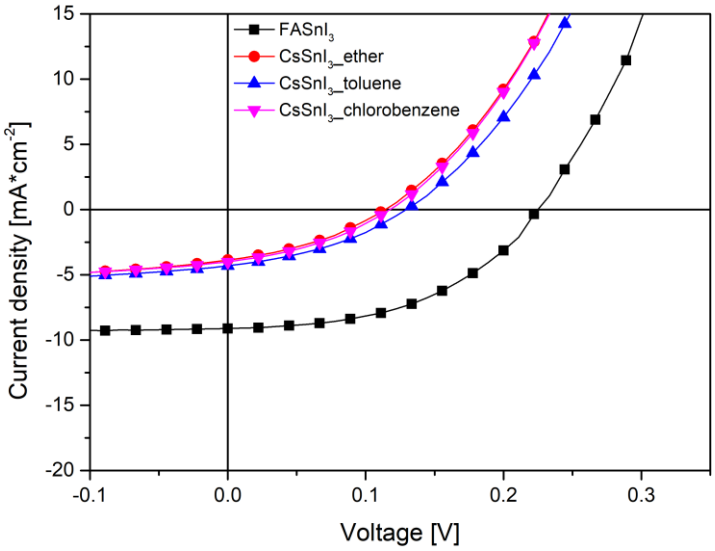


**Figure 21** *JV-measurement: Investigation of different antisolvents for the fabrication of $CsSnI_3$.*

**Table 10** *Results of the different $CsSnI_3$ cells. Mean values and standard deviations were calculated from the 5 best solar cells.*

| Substrate | | PCE [%] | FF [%] | $J_{SC}$ [mA*cm$^{-2}$] | $V_{OC}$ [V] |
|---|---|---|---|---|---|
| **$FASnI_3$** | Mean | 0.87 ± 0.07 | 47.9 ± 0.5 | -8.5 ± 0.5 | 0.22 ± 0.01 |
| | Best | 0.96 | 48.2 | -9.1 | 0.22 |
| **$CsSnI_3$ diethylether** | Mean | 0.14 ± 0.01 | 35.6 ± 1.2 | -3.7 ± 0.1 | 0.11 ± 0.01 |
| | Best | 0.16 | 36.7 | -3.9 | 0.11 |
| **$CsSnI_3$ toluene** | Mean | 0.18 ± 0.02 | 35.9 ± 1.0 | -4.0 ± 0.2 | 0.13 ± 0.01 |
| | Best | 0.20 | 35.9 | -4.3 | 0.13 |
| **$CsSnI_3$ chlorobenzene** | Mean | 0.16 ± 0.01 | 36.2 ± 1.3 | -3.8 ± 0.3 | 0.12 ± 0.01 |
| | Best | 0.17 | 34.7 | -4.0 | 0.12 |

The results of all produced $CsSnI_3$ cells with variating antisolvents were relatively similar. There cannot be seen big differences in PCE, FF, $J_{SC}$, $V_{OC}$. Especially, the $V_{OC}$ values for all $CsSnI_3$ systems were very low. Also, the desired change in crystallization behavior by usage of different antisolvents was not obtained. All in all, the $CsSnI_3$ solar cells provided worse results compared to the $FASnI_3$ solar cells. Other following experiments showed that an absence of AS caused no differences in the cell performance and no apparent differences of the perovskite film.

Due to the fact, that the $CsSnI_3$ absorber layer was not working well, also other methods for the formation of the perovskite thin film were tested. This comprised hot substrate spinning at about 70 °C and hot AS dripping with 70 °C hot solvent. For the hot substrate spinning two different ways were tested. First, only a 70 °C hot metal block was used, but the substrates were at room temperature to produce a temperature gradient during the spin coating of the $CsSnI_3$ solution. It was observable that the $CsSnI_3$ film began to crystallize slightly during spin coating, but it could not be produced a homogeneous thin film during the spin coating process that was based on a temperature gradient. Second, the substrates were heated to 70 °C before spin coating and the metal block was heated as well to 70 °C to hold the temperature during the whole spin coating procedure. This experiment worked better and caused a homogeneous crystallization of the perovskite film during the spin coating process. Warm antisolvent dripping caused no immediate crystallization of the perovskite nor in combination with the heated metal block. All these other methods provided worse results compared to the procedure described above and were not an interesting alternative.

Song et al. provided interesting results by varying the molar ratios of CsI to $SnI_2$ for the perovskite solutions. They obtained a record PCE of 4.81% for a mesoporous $CsSnI_3$ PSC with a molar ratio of 0.4M:1M prepared in a reducing hydrazine atmosphere.[53] Therefore, also the ratios 0.4M:1M and 0.6M:1M for CsI to $SnI_2$ were tested. The obtained results showed much higher $V_{OC}$ values but vanishingly small current density values. Although, the $FASnI_3$ reference was working properly, the $CsSnI_3$ substrates showed bad results of the JV-curves and dark curves, which ran relatively flat and were not fitting properly to the x-axis at zero current density. The dark curves suggested that the cells were not functioning properly. Since different fabrication methods of the perovskite layer were tested and nothing was working as good as the power conversion efficiencies shown in literature it gets obvious that this inverted set-up is not suitable for the fabrication of $CsSnI_3$ solar cells.

## 3.5 Influence of $SnF_2$ on cell performance of $FASnI_3$

The influence of $SnX_2$ compounds on $ASnX_3$ perovskite films in solar cells is of high interest. Especially, $SnF_2$ additions to the perovskite precursor solutions were investigated in detail over the last years. One extensively studied behavior is a preventive effect on the oxidation of $Sn^{2+}$ to $Sn^{4+}$ and its minimization of tin vacancies in the perovskite thin film. Furthermore, tin fluoride was found to improve the film morphology by reduction of pinholes and voids in the surface. Depending on the perovskite system also other properties like minimization of unwanted crystal phases, improved stability in ambient environment and effects on the energy level positions were observed.[10] All these observations made it interesting to take a closer look.

This experiment should provide information about the influence of the tin fluoride concentration on the cell performance of $FASnI_3$. Therefore, $SnF_2$ concentrations ranging from 0 mol% to 20 mol% were added to the perovskite precursor solution. These solar cells have the same set-up and were produced the same way as described in the experimental section. Figure 22 and table 11 show the results of the $SnF_2$ series.

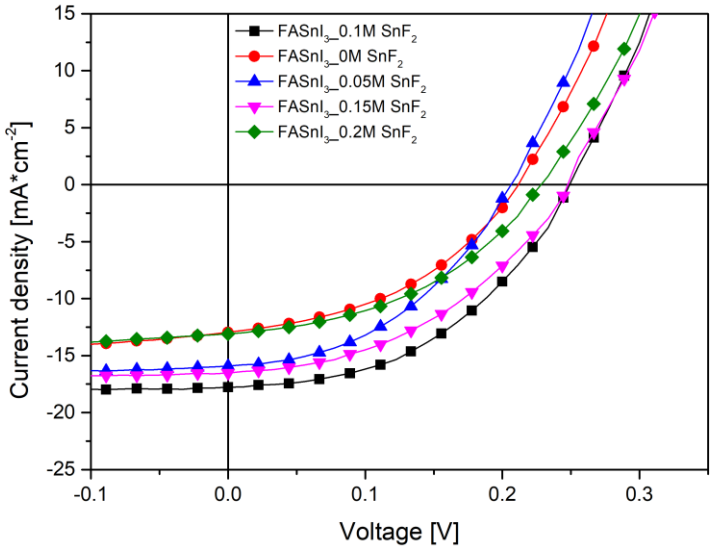


**Figure 22** *JV-measurement: Influence of different $SnF_2$ concentrations on the $FASnI_3$ solar cell performance.*

**Table 11** *Results of the different $SnF_2$ concentrations. The mean values and standard deviations were calculated from the 5 best solar cells.*

| Substrate | | PCE [%] | FF [%] | $J_{SC}$ [mA*cm$^{-2}$] | $V_{OC}$ [V] |
|---|---|---|---|---|---|
| **0 % $SnF_2$** | Mean | 1.08 ± 0.06 | 43.6 ± 0.7 | -12.2 ± 0.8 | 0.20 ± 0.01 |
| | Best | 1.16 | 42.6 | -13.0 | 0.21 |
| **5 % $SnF_2$** | Mean | 1.40 ± 0.02 | 36.5 ± 14.8 | -15.7 ± 0.3 | 0.21 ± 0.01 |
| | Best | 1.42 | 42.4 | -15.9 | 0.21 |
| **10 % $SnF_2$ Reference** | Mean | 1.78 ± 0.16 | 45.2 ± 1.1 | -16.8 ± 0.8 | 0.24 ± 0.01 |
| | Best | 2.01 | 46.8 | -17.8 | 0.24 |
| **15% $SnF_2$** | Mean | 1.59 ± 0.12 | 43.2 ± 0.7 | -15.9 ± 0.5 | 0.23 ± 0.01 |
| | Best | 1.75 | 43.7 | -16.5 | 0.24 |
| **20% $SnF_2$** | Mean | 1.20 ± 0.06 | 42.5 ± 1.2 | -13.0 ± 0.4 | 0.22 ± 0.01 |
| | Best | 1.28 | 42.2 | -13.1 | 0.23 |

The results provide, that the performance is highly influenced by the addition of tin fluoride. The best solar cell was the reference cell, which contained 10 mol% $SnF_2$ and showed a PCE of 2.01%, a FF of 46.8%, a $J_{SC}$ of -17.8 mA*cm$^{-2}$ and a $V_{OC}$ of 0.24 V. All the other tested concentrations of $SnF_2$ in the precursor solution resulted in worse PCEs and are most probably less interesting for further investigations. It should be mentioned that this experiment was repeated a few times and the results of a 20 mol% $SnF_2$ addition were fluctuating wildly and thus are not entirely reliable. The poor results of cells without any $SnF_2$ indicate that this compound is crucial for a properly working device.

Lee et al. described a positive influence on the film morphology of a $FASnI_3$ perovskite layer through a $SnF_2$-pyrazine complex.[64] Therefore, also the addition of 5 mol%, 10 mol% and 20 mol% pyrazine to the perovskite solution were tested. This positive influence on the cell performance caused by improved morphology could unfortunately not be verified by our experiments.

## 3.6 Double cation perovskites

In the past, different organic ammonium salts were used for the production of perovskite solar cells. Ke and co-workers demonstrates that also diammonium cations are suitable for the application in Sn-perovskite solar cells and are even capable to improve the device performance.[74] During this work a formamidinium iodide salt was either mixed with hexylammonium iodide or the diammonium salt piperazine-1,4-diium iodide for the preparation of the tin perovskite absorber layers.

All solar cells had the set-up "Glass-ITO/PEDOT:PSS/Perovskite/$PC_{60}BM$/Aluminium". All layers were fabricated the same way like described in the experimental part. Also here the absorber layers were produced with 50 µL precursor solution and two times AS dripping at 10 s and 70 s.

### 3.6.1 Formamidinium piperazine-1,4-diium tin iodide

Piperazine-1,4-diium (PIP) seemed to be a promising compound for the usage as A-site cation in combination with formamidinium. Different amounts of PIP in a range of 1-20% in a $FA_{1-x}PIP_xSnI_3$ perovskite system were tested. Since 15% and 20% of PIP provided worse results compared to other concentrations, a main focus was on lower concentrations. In graph 23 and table 12 the results of the JV-measurements of solar cells prepared with 1-5% PIP additions to the $FASnI_3$ precursor solution are shown.

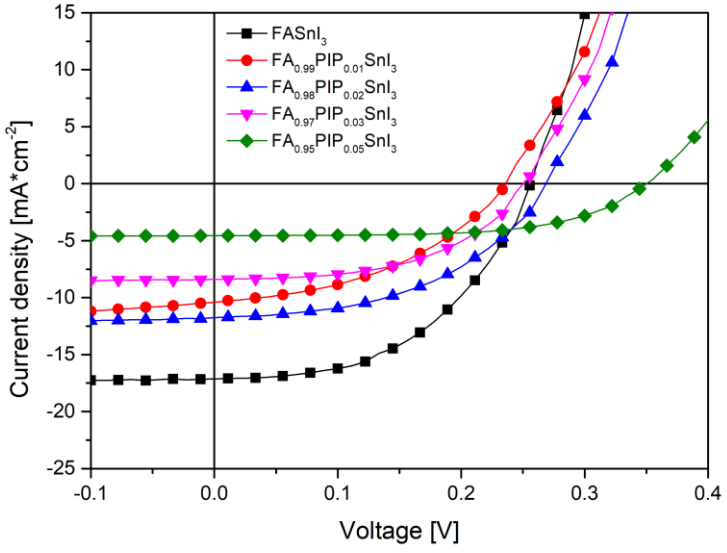


**Figure 23** *JV-measurement: Investigation of the introduction of different amounts of piperazine-1,4-diium iodide into the $FASnI_3$ perovskite.*

**Table 12** *Results of different piperazine-1,4-diium iodide amounts in the $FASnI_3$ structure. The mean values and standard deviations were calculated from the 5 best cells.*

| Substrate | | PCE [%] | FF [%] | $J_{SC}$ [mA*cm$^{-2}$] | $V_{OC}$ [V] |
|---|---|---|---|---|---|
| **$FASnI_3$** | Mean | 2.09 ±0.06 | 49.1 ± 0.9 | -17.7 ± 0.4 | 0.24 ± 0.01 |
| | Best | 2.14 | 49.7 | -17.1 | 0.26 |
| **$FA_{0.99}PIP_{0.01}SnI_3$** | Mean | 0.59 ± 0.40 | 38.2 ± 4.4 | -7.7 ± 2.5 | 0.19 ± 0.05 |
| | Best | 1.04 | 43.1 | -10.4 | 0.23 |
| **$FA_{0.98}PIP_{0.02}SnI_3$** | Mean | 1.27 ± 0.33 | 45.3 ± 3.6 | -10.8 ± 1.4 | 0.26 ± 0.02 |
| | Best | 1.51 | 48.5 | -11.8 | 0.27 |
| **$FA_{0.97}PIP_{0.03}SnI_3$** | Mean | 1.02 ± 0.08 | 50.1 ± 0.8 | -8.4 ± 0.2 | 0.24 ± 0.01 |
| | Best | 1.12 | 51.3 | -8.4 | 0.26 |
| **$FA_{0.95}PIP_{0.05}SnI_3$** | Mean | 0.87 ± 0.08 | 61.2 ± 0.9 | -4.2 ± 0.3 | 0.34 ± 0.01 |
| | Best | 0.97 | 59.8 | -4.6 | 0.36 |

It can be observed that the $V_{OC}$ of the 5% PIP substrate was much higher than that of the reference cell and other lower PIP concentrations. This trend was also found in other series with higher percentages of piperazine-1,4-diium iodide. In general, the higher the PIP content, the higher was the $V_{OC}$ and the lower the $J_{SC}$. Since the 2% substrate showed slightly higher open circuit voltages and higher current densities than other PIP samples, a special focus was put on this concentration.

### 3.6.2 Formamidinium hexylammonium tin iodide

The second cation, which was used in combination with formamidinium was n-hexylammonium (HA). These solar cells had an absorber layer which had the general form $FA_{1-x}HA_xSnI_3$. Figure 24 shows the JV-curves of an absorber layer with a percentage of 3% and 5% HA as well as the reference $FASnI_3$ cell (solar cells had an area of 0.09 cm$^2$ and were measured without mask).

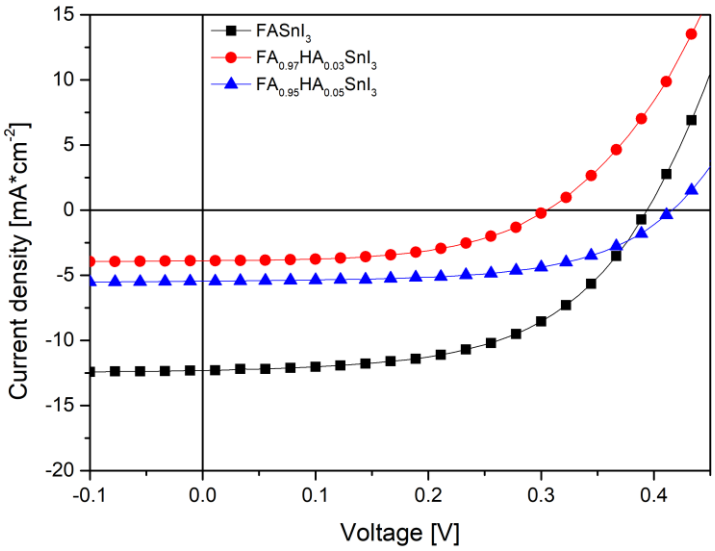


**Figure 24** *JV-measurement: Investigation of the introduction of different amounts n-hexylammonium iodide into the $FASnI_3$ perovskite.*

Both $FA_{1-x}HA_xSnI_3$ perovskites worked worse than the reference. Better results were obtained with additions of 5 mol% HAI. It was also tested a $FA_{0.9}HA_{0.1}SnI_3$ perovskite, which provided worse results compared to lower concentrations and is therefore, not shown here. It can be seen, that the incorporation of hexylammonium iodide has a similar effect on the open circuit voltage like the piperazine-1,4-diium iodide, which caused an increase in $V_{OC}$. The results of the best $FA_{1-x}HA_xSnI_3$ cells are listed in table 13.

**Table 13** *Results of different n-hexylammonium iodide amounts in the $FASnI_3$ structure. The mean values and standard deviations were calculated from the 5 best solar cells.*

| Substrate | | PCE [%] | FF [%] | $J_{SC}$ [mA*cm$^{-2}$] | $V_{OC}$ [V] |
|---|---|---|---|---|---|
| **$FASnI_3$** | Mean | 1.92 ± 0.40 | 50.6 ± 2.7 | -11.2 ± 0.6 | 0.34 ± 0.03 |
| | Best | 2.62 | 55.2 | -12.3 | 0.39 |
| **$FA_{0.97}HA_{0.03}SnI_3$** | Mean | 0.37 ± 0.16 | 49.1 ± 3.1 | -2.8 ± 0.7 | 0.26 ± 0.02 |
| | Best | 0.62 | 53.3 | -3.9 | 0.30 |
| **$FA_{0.95}HA_{0.05}SnI_3$** | Mean | 1.12 ± 0.12 | 56.4 ± 1.8 | -5.0 ± 0.3 | 0.40 ± 0.02 |
| | Best | 1.30 | 58.5 | -5.5 | 0.41 |

### 3.6.3 Comparison and characterization of the best concentrations

In this section the results of the best tested PIP and HA concentrations are compared. This comprises JV-measurements and an investigation of the cell hysteresis, MPP tracking as well as EQE measurements. In figure 25 JV-plots of the best PIP and HA concentrations in comparison with $FASnI_3$ are shown. The results of the measurements are listed in table 14.

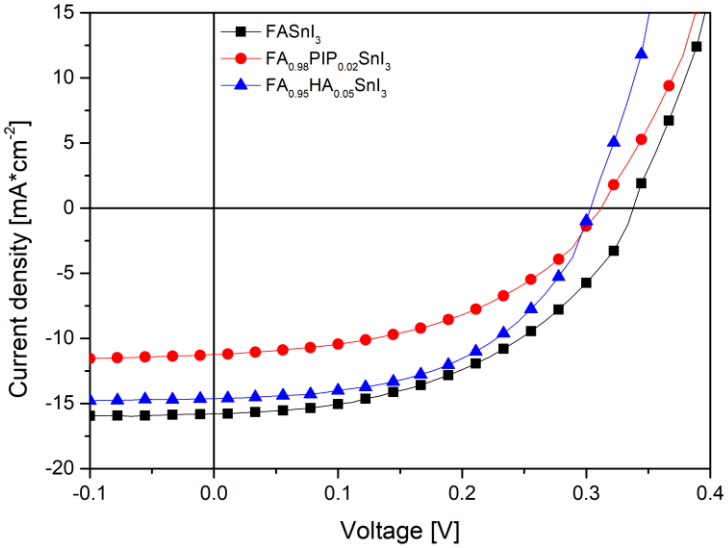


**Figure 25** *JV-measurement: Comparison of the JV-measurements of the double cation perovskites with $FASnI_3$.*

**Table 14** *Results of the $FASnI_3$ reference cell and the double cation perovskites. The mean values and standard deviations were calculated from the 5 best solar cells.*

| Substrate | | PCE [%] | FF [%] | $J_{SC}$ [mA*cm$^{-2}$] | $V_{OC}$ [V] |
|---|---|---|---|---|---|
| **$FASnI_3$** | Mean | 2.11 ± 0.49 | 44.1 ± 4.6 | -16.0 ± 1.0 | 0.30 ± 0.03 |
| | Best | 2.52 | 48.1 | -15.9 | 0.33 |
| **$FA_{0.98}PIP_{0.02}SnI_3$** | Mean | 1.12 ± 0.45 | 40.6 ± 5.8 | -9.7 ± 1.3 | 0.27 ± 0.04 |
| | Best | 1.64 | 47.0 | -11.2 | 0.31 |
| **$FA_{0.95}HA_{0.05}SnI_3$** | Mean | 1.59 ± 0.58 | 44.9 ± 5.5 | -12.4 ± 2.3 | 0.28 ± 0.03 |
| | Best | 2.31 | 52.9 | -14.6 | 0.30 |

The reference substrate provided better results than the double cationic mixtures. While, the PIP sample showed relatively bad results, the HA sample worked compared to previous series very well although, it showed lower open circuit voltages as usual.

Especially, perovskite solar cells often show a phenomenon, which is called hysteresis. It describes differences in the solar cell parameters depending on the measurement direction. Generally, a measurement can be carried out in backward (in this case from 1000 mV to -100 mV) or forward direction (-100 to 1000 mV). The hysteresis behavior of the PIP and HA sample are shown in figure 26A and 26B. Left is shown the hysteresis of the $FA_{0.98}PIP_{0.02}SnI_3$ cell and right the hysteresis of the $FA_{0.95}HA_{0.05}SnI_3$ cell after MPP tracking.

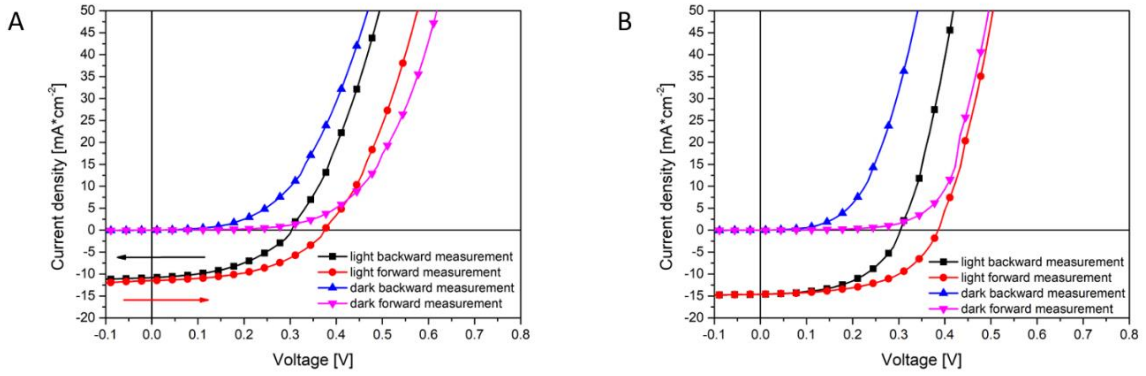


**Figure 26** *Investigation of the hysteresis behavior of the double cation perovskites. In the left image (**A**) can be seen the hysteresis of a $FA_{0.98}PIP_{0.02}SnI_3$ solar cell and in the right image (**B**) the hysteresis of $FA_{0.95}HA_{0.05}SnI_3$.*

Graph 26A shows similar hysteresis as Graph 26B. Due to this hysteresis behavior it is sometimes necessary to do further measurements to determine the actual power conversion efficiency of a measured solar cell. Therefore, a maximum power point tracking was used. Figure 27 shows the MPP tracking of the $FA_{0.98}PIP_{0.02}SnI_3$ and the $FA_{0.95}HA_{0.05}SnI_3$ cell. There are shown the PCE, the $P_{mpp}$, $J_{mpp}$, and $V_{mpp}$ as a function of time. Both cells were tracked over approximately 65 min.

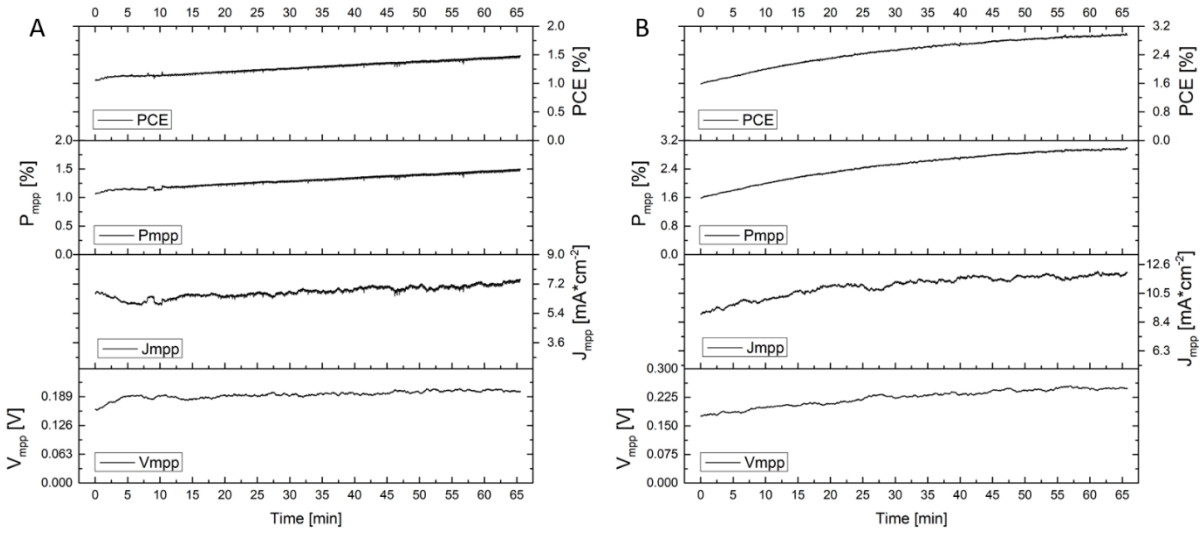


**Figure 27** *MPP tracking of (**A**) $FA_{0.98}PIP_{0.02}SnI_3$ and (**B**) $FA_{0.95}HA_{0.05}SnI_3$*

In both Figure 27A and 27B can be seen, that all parameters of the tracked cells became better over time. It is not clear if this improvement is caused by light soaking of the absorber layer or the voltage applied during measurement. The $FA_{0.98}PIP_{0.02}SnI_3$ cell showed in the beginning a PCE value of about 1.03 %, a FF of 43 %, a $J_{SC}$ of about -9.9 mA*cm$^{-2}$ and a $V_{OC}$ of 0.24 V. Tracking of the cell caused an increase in all these parameters to 1.49 % PCE, 46% FF, -10.8 mA*cm$^{-2}$ $J_{SC}$ and a $V_{OC}$ of 0.30 V. Also, the $FA_{0.95}HA_{0.05}SnI_3$ cell provided an improvement of all parameters over tracking time and began to stabilize at approximately 60min. The parameters started at a PCE of 1.55%, a FF of 48.1%, a $J_{SC}$ of -14.0 mA*cm$^{-2}$ and a $V_{OC}$ of 0.23 V and improved to higher values of approximately 2.31% PCE, 52.9% FF, -14.6 mA*cm$^{-2}$ $J_{SC}$ and 0.30 V $V_{OC}$. The results, which are shown here are always the values of the reverse scans that are lower than the results of the forward measurement. Therefore, slight deviations from the values in figure 27 can be observed.

External quantum efficiency measurements were carried out to determine the probability to excite an electron by a photon with a specific energy. Figure 28 represents the EQE spectra of the two double cation mixtures $FA_{0.98}PIP_{0.02}SnI_3$ and $FA_{0.95}HA_{0.05}SnI_3$, measured over a wavelength range from 380 nm to 1000 nm.

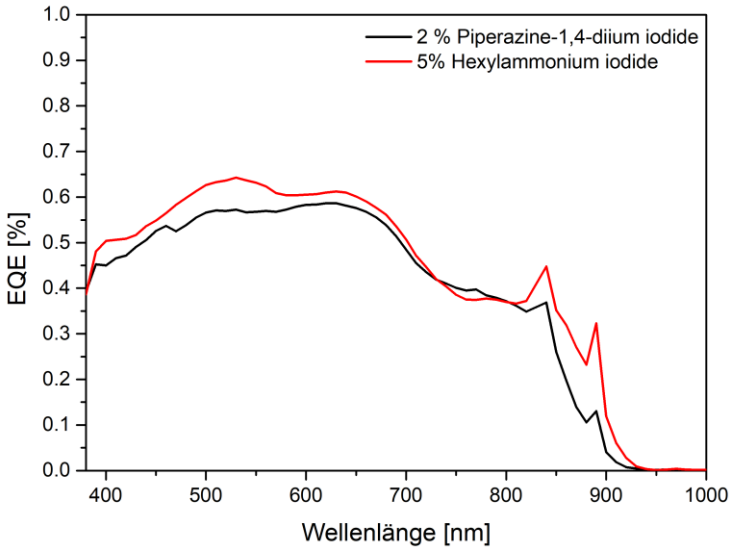


**Figure 28** *EQE measurements of the double cation perovskite solar cells.*

The investigated PIP cell provided a maximum EQE value of approximately 59 % at 630 nm. For the HA cell a slightly higher value of 64% at 530 nm was reached. Both perovskites are capable to generate current over the whole visible wavelength range. Comparison of the EQE spectra with the absorption spectra in section 3.1.2 provides approximately the same onset location at approximately 900 nm.

## 3.7 Investigation of the layer morphology

The most important perovskite absorber layers investigated were analyzed with scanning electron microscopy by Dr. Theodoros Dimopoulos. This comprises $FASnI_3$, $PIP_{0.02}FA_{0.98}SnI_3$ and $HA_{0.05}FA_{0.95}SnI_3$. All perovskite layers were produced on glass substrates coated with PEDOT:PSS. In the past, literature demonstrated that the perovskite layer morphology had a huge impact on the device performance.

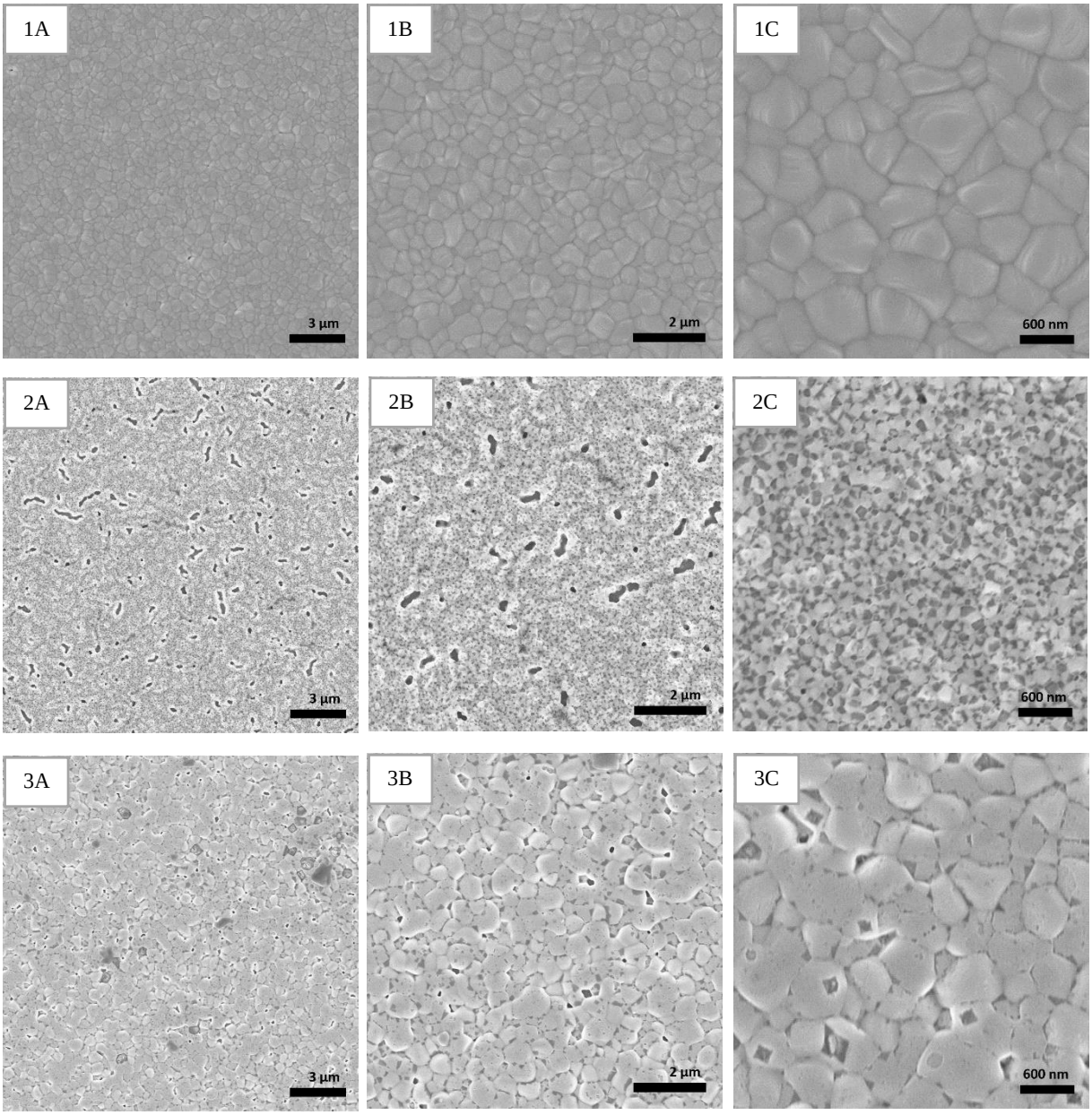


**Figure 29** *SEM images of $FASnI_3$ (**1A-C**), $FA_{0.98}PIP_{0.02}SnI_3$ (**2A-C**) and $FA_{0.95}HA_{0.05}SnI_3$ (**3A-C**).*

Figure 29 shows the three investigated perovskite thin films of the reference $FASnI_3$ cell (1A – C) as well as $PIP_{0.02}FA_{0.98}SnI_3$ (2A – C) and $HA_{0.05}FA_{0.95}SnI_3$ (3A – C). The $FASnI_3$ thin film demonstrates a very smooth surface with practically no pinholes or voids. $PIP_{0.02}FA_{0.98}SnI_3$ looks very different. Here the surface shows many pinholes. In 2C can be seen the 50 000 times magnification that reveals a spongy structure. It is difficult to determine if this structure originated by the vacuum conditions in the SEM device or this structure really represents the perovskite layer after fabrication, which would be found in the constructed solar cell. Since the performance of these cells is not that bad, it seems likely that the structure was mainly influenced by the vacuum. The pictures 3A – C represent the $HA_{0.05}FA_{0.95}SnI_3$ perovskite. Here the layer looks also relatively smooth little defects. In the 50 000 times magnification of the perovskite layer shown in 3C the defects of the grains can be seen better.

These observations are in accordance with the results shown in section 3.6. $FASnI_3$ revealed the smoothest perovskite layer and the best cell performance whereas, the $PIP_{0.02}FA_{0.98}SnI_3$ sample showed many pinholes and voids and comparatively worse JV-measurement results.

Nearly all perovskite layers showed a gray haze on the surfaces directly after spin coating of the absorber layer that was visible by the naked eye. Especially, the $FASnI_3$ reference system seemed to be highly dependent on that haze. This gray layer is most probably responsible for a worse cell performance of the fabricated solar cells. It was hoped to gain new information through the SEM analysis of the perovskite thin films but there was no hint of that haze observable in the pictures.

## 3.8 Insertion of salt interlayers

In the following experiment different salt interlayers with a concentration of 20 mg/ml were inserted between the PEDOT:PSS and the absorber layer. Therefore, the salt solutions, which were solved in DMF:DMSO with the ratio 4:1 were spin coated onto the PEDOT:PSS layer with 3000 rpm and an acceleration of 2000 $rpm*s^{-1}$. Afterwards, a formamidinium tin iodide absorber layer was spin coated onto the salt interlayer and the crystallization was carried out like described in the experimental part with two times AS dripping. Figure 30 shows the JV-curves and table 15 the corresponding results of $FASnI_3$ solar cells with different salt interlayers.

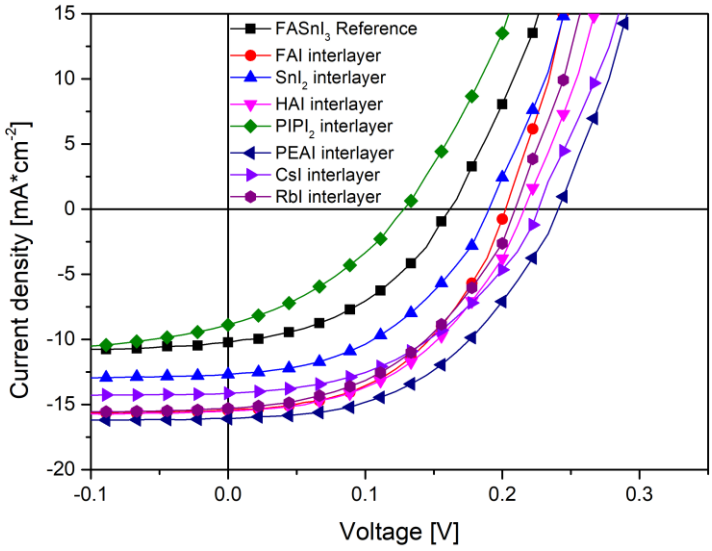


**Figure 30** *JV-measurement: Investigation of different interlayers between PEDOT:PSS and the perovskite layer.*

**Table 15** *Results of the investigation of different interlayers. The mean values and standard deviations were calculated from the 5 best solar cells.*

| Substrate | | PCE [%] | FF [%] | $J_{SC}$ [mA*cm$^{-2}$] | $V_{OC}$ [V] |
|---|---|---|---|---|---|
| **Reference** | Mean | 0.62 ± 0.06 | 42.0 ± 0.7 | -9.9 ± 0.3 | 0.15 ± 0.01 |
| | Best | 0.69 | 41.3 | -10.2 | 0.17 |
| **FAI** | Mean | 1.36 ± 0.09 | 47.3 ± 1.2 | -14.5 ± 0.6 | 0.20 ± 0 |
| | Best | 1.51 | 49.2 | -15.4 | 0.2 |
| **$SnI_2$** | Mean | 1.04 ± 0.03 | 43.3 ± 1.2 | -13.1 ± 0.5 | 0.18 ± 0.01 |
| | Best | 1.08 | 45.3 | -12.7 | 0.19 |
| **HAI** | Mean | 1.39 ± 0.10 | 45.8 ± 1.7 | -15.1 ± 0.3 | 0.20 ± 0 |
| | Best | 1.56 | 47.9 | -15.5 | 0.21 |
| **$PIPI_2$** | Mean | 0.31 ± 0.06 | 34.0 ± 1.07 | -8.11 ± 0.6 | 0.11 ± 0.01 |
| | Best | 0.40 | 34.0 | -8.9 | 0.13 |
| **PEAI** | Mean | 1.62 ± 0.16 | 47.1 ± 0.9 | -15.3 ± 0.9 | 0.23 ± 0.01 |
| | Best | 1.85 | 47.3 | -16.1 | 0.24 |
| **CsI** | Mean | 1.37 ± 0.06 | 46.1 ± 1.1 | -14.5 ± 0.4 | 0.21 ± 0.01 |
| | Best | 1.44 | 46.7 | -14.1 | 0.22 |
| **RbI** | Mean | 1.23 ± 0.14 | 43.8 ± 1.0 | -14.1 ± 0.8 | 0.20 ± 0.01 |
| | Best | 1.46 | 45.4 | -15.3 | 0.21 |

In general, it can be observed that most of the interlayers led to an improvement of the reference $FASnI_3$ system. Only the piperazine-1,4-diium iodide interlayer caused a declined performance of the solar cell. The best results were obtained with a phenethylammonium iodide, hexylammonium iodide, cesium iodide and rubidium iodide interlayer. Chen et al. described the improved performance of a $FASnI_3$ cell with a PEABr interlayer and referred it to the formation of a 2D/3D perovskite structure at the interphase between the PEDOT:PSS and perovskite absorber layer, caused by the diffusion of salt ions into the perovskite layer.[78] Most probably the same effect can be observed with the PEAI interlayer. Hexylammonium iodide most probably also causes the formation of a 2D/3D structure of the perovskite like discussed in section 3.2.2. Therefore, it can be supposed that also HAI shows that behavior. The improvement of the cell by insertion of RbI or CsI can be explained by the much smaller effective radii of these ions compared to formamidinium. Gao and co-workers described the effect of CsI insertion into $FASnI_3$ lattice with a contraction of the corner sharing $SnI_6$ octahedra that consequently, caused an improvement of the geometric symmetry of the $FASnI_3$ structure.[102]

All in all, the integration of interlayers led to an overall improvement of the perovskite solar cells and should be further investigated in the future.

## 3.9 Best $FASnI_3$ cell

The best cell obtained during this work was a $FASnI_3$ solar cell with the set-up "Glass-ITO/PEDOT:PSS/Perovskite/PCBM/Aluminium". The perovskite solution was spin coated with 5000 rpm and 2000 rpm*$s^{-1}$ and the crystallization was induced with two times chlorobenzene AS dripping at 10 s and 70 s.

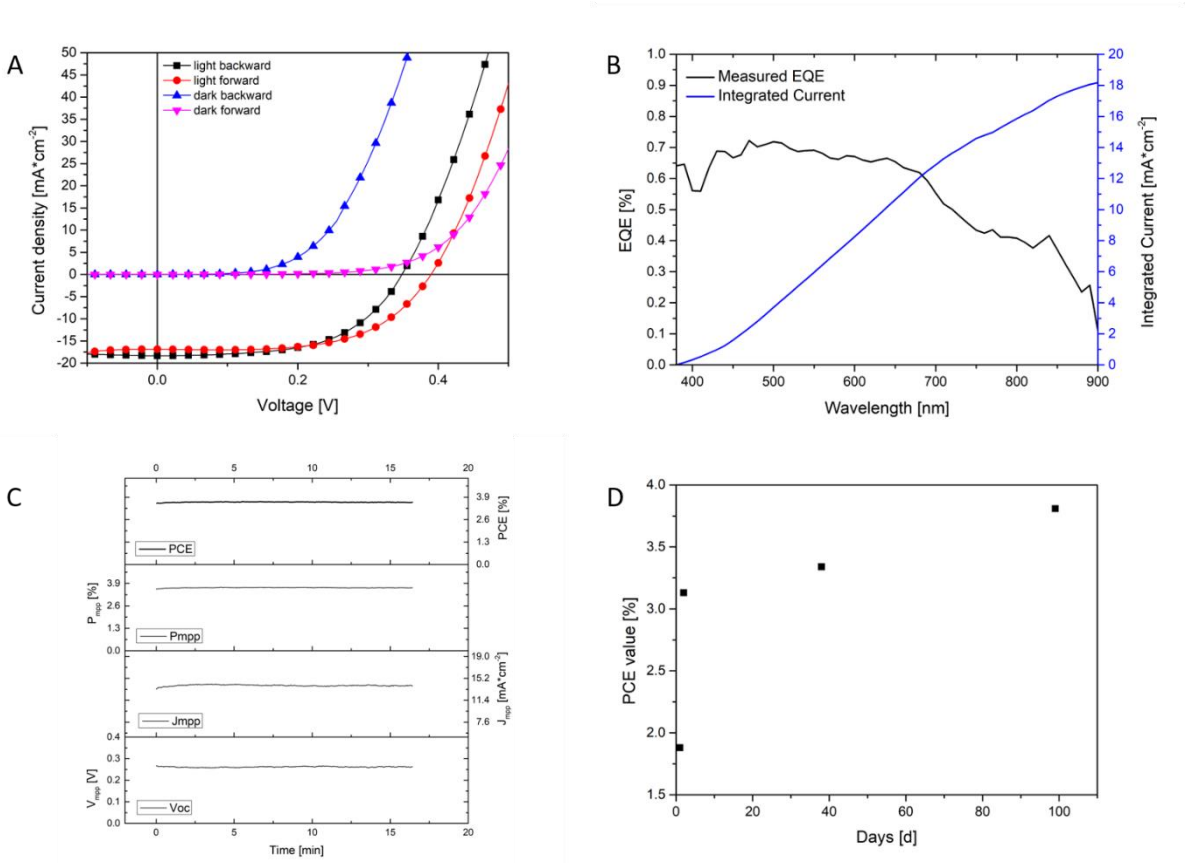


**Figure 31** *Characteristics of the best $FASnI_3$ solar cell. (**A**) Hysteresis, (**B**) EQE and integrated current, (**C**) MPP tracking, (**D**) Stability measurement.*

The best $FASnI_3$ cell provided a PCE value of 3.55 %, a FF of 56.7 %, a $J_{SC}$ of -18.3 mA*$cm^{-2}$ and a $V_{OC}$ of 0.34 V. All measurements were carried out with a mask that had an area of 0.0702 $cm^2$. Looking at Figure 31 A it can be observed that the reference system also showed hysteresis but less compared to the tested double cation Sn-perovskite solar cells. Figure 31 B shows the EQE spectrum of $FASnI_3$ and the calculated current density. The integrated $J_{SC}$ provided a value of approximately -18.2 mA*$cm^{-2}$, which is similar to the measured current density of -18.3 mA*$cm^{-2}$. This cell showed a relatively high external quantum efficiency of 72 %.

Since the cell showed hysteresis behavior also MPP tracking was carried out. Figure 31 C shows MPP tracking of the $FASnI_3$ cell over 16 min. The PCE stayed relatively constant over that time range and decreased only slightly.

To investigate the stability of the best $FASnI_3$ perovskite solar cell the PCE value of the cell was measured a few times within 100 days (see figure 31 D). The recorded measurement points were measured without a mask and therefore the radiated area was 0.09 $cm^2$. It can be seen, that the cell improved very much from the first day to the second day. Afterwards, the cell performance improved further but not in that extent. This behavior was also observed for other perovskite solar cells.

The record PCE of 3.55 % for a $FASnI_3$ cell measured with mask is higher than other cells investigated during this work but nevertheless significantly lower than actual literature values for the same perovskite. Liao et al. presented a $FASnI_3$ perovskite solar cell with the set-up "Glass-ITO/PEDOT:PSS/$FASnI_3$/$C_{60}$/BCP/Ag". This cell was capable to reach a record PCE of 6.22% under illumination of 100 $mW*cm^{-2}$ and an area of 0.04 $cm^2$.[65]

Bathocuproin buffer layers in between the electron transport layer and the electrode often cause an increased solar cell performance like shown by Chen and co-workers.[103] Therefore, it was also tried to improve the $FASnI_3$ perovskite solar cell performance by insertion of a bathocuproine interlayer, using thermal evaporation. It resulted a worse cell performance compared to the reference procedure and the wished enhancement could not be achieved.

## 3.10 Reproducibility and observations

During this work, it was observed that the fabrication of solar cells, especially the fabrication of the perovskite layer, depends on many different factors. Since $Sn^{2+}$ can be easily oxidized to $Sn^{4+}$, the oxygen and water content in the glovebox played a crucial role during the fabrication. Very often the perovskite layers looked more reflective and the cell performances were better after regeneration. Another important factor was the solvent atmosphere inside the glovebox or inside the spin coater. For the fabrication of the perovskite layer was used a perovskite precursor solution made with a solvent mixture of 4:1 DMF:DMSO and chlorobenzene was used as AS during spin coating. Often, the cells in the beginning worked worse compared to the cells, which were produced in the end of a series. This can be most probably explained by the solvent atmosphere, which generates during the working procedure. At the beginning, the atmosphere in the spin coater was relatively neutral and became more and more saturated with DMF and DMSO over time, which seemed to help to produce the perovskite layer. However, the parallel developing CB atmosphere seemed to have a negative impact on the solar cell performance. As a consequence, it was often a problem to work directly after somebody else, since the atmosphere was still saturated with solvent vapors.

Furthermore, it was investigated the influence of molecular sieves that were used for drying of solvents. In figure 32 the PCE values for $FASnI_3$ references that were fabricated and measured during this thesis are shown. The left image shows that obtained PCE values for $FASnI_3$ cell that were fabricated by usage of molecular sieves, while the right image shows all $FASnI_3$ cells that were fabricated without molecular sieves. On the x-axis is plotted the number of cells, on the y-axis the range of the PCE values and on top of each bar the percentage of solar cells with the respective PCE range.

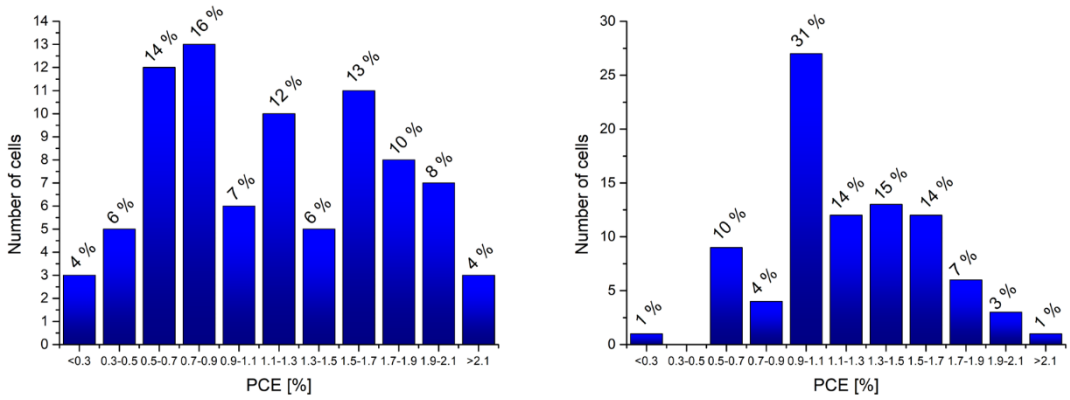


**Figure 32** *Comparison of the efficiencies of $FASnI_3$ cells that were fabricated with molecular sieves (left) or without molecular sieves (right).*

It can be seen, that the cells produced with molecular sieves have a larger distribution of PCE values. In this case, 16% of the produced cells in the left image provided a PCE value between 0.7% and 0.9%. The $FASnI_3$ cells that were produced completely without molecular sieves, showed a narrower distribution, where 31% of the produced cells showed a PCE value between 0.9% and 1.1%. For these analyzes only measurements on the first day with mask (area of 0.0702 $cm^2$) were taken into consideration. Looking at these distributions it becomes apparent that the reproducibility of Sn-based PSCs is a challenging problem that must be fixed in the future.

Another interesting effect was observed when the cells were measured multiple times or over longer time (MPP tracking). In nearly all cases, the solar cells provided better efficiencies if they were measured on the first day and again on the second day after fabrication. In particular this improvement was caused by an increase in $V_{OC}$ and $J_{SC}$. However, it is difficult to conclude if this improvement was caused by light soaking, the applied voltage during measurement or changes in the materials of the PSCs.

# 4 Experimental Part

## 4.1 List of chemicals

In table 16 all used chemicals for the preparation and fabrication of the perovskite solar cells are represented. This table comprises the used chemicals, the abbreviations and chemical formulas, the suppliers as well as the purity of the compound and other important information.

**Table 16** *Necessary chemicals, abbreviations and chemical formulas, suppliers, purities and additional information for the production of solar cells*

| Chemical | Abbreviations and Chemical Formulas | Supplier | Purity | Additional Information |
|---|---|---|---|---|
| Glass-indium tin oxide substrates | - | Luminescence Technology Corp. | - | 15x15x1.1 mm 15Ω |
| Poly-(3,4-ethylene dioxythiophene)-poly(styrene sulfonate); Clevios P VP.AI 4083 | PEDOT:PSS | Heraeus | 1.3-1.7% solids content in $H_2O$ | pH 1.2 – 2.2 |
| Tin iodide | $SnI_2$ | Sigma Aldrich | 99.99% | - |
| Tin fluoride | $SnF_2$ | Sigma Aldrich | 99% | - |
| Formamidinium iodide | FAI | Dyesol | - | - |
| Piperazine-1,4-diium iodide | $PIPI_2$ | Dyesol | - | - |
| n-Hexylammonium iodide | HAI | Dyesol | - | - |
| Phenethylammonium iodide | PEAI | Dyesol | - | - |
| Cesium iodide | CsI | Sigma Aldrich | 99.999% | - |
| Rubidium iodide | RbI | Sigma Aldrich | 99.9% | - |
| [6,6]-Phenyl $C_{61}$ butyric acid methyl ester | $PC_{60}BM$ | Solenne | 99.5% | - |
| Chlorobenzene anhydrous | CB | Sigma Aldrich | 99.8% | - |
| N,N-Dimethylformamide anhydrous | DMF | Merck SeccoSolv | max. 0.003% water | - |
| Dimethyl sulfoxide anhydrous | DMSO | Sigma Aldrich | ≤ 0.02% water | - |
| 2-Propanol | | Carl Roth GmbH | ≥ 99.8% | - |

## 4.2 Principle set-up of the solar cell system

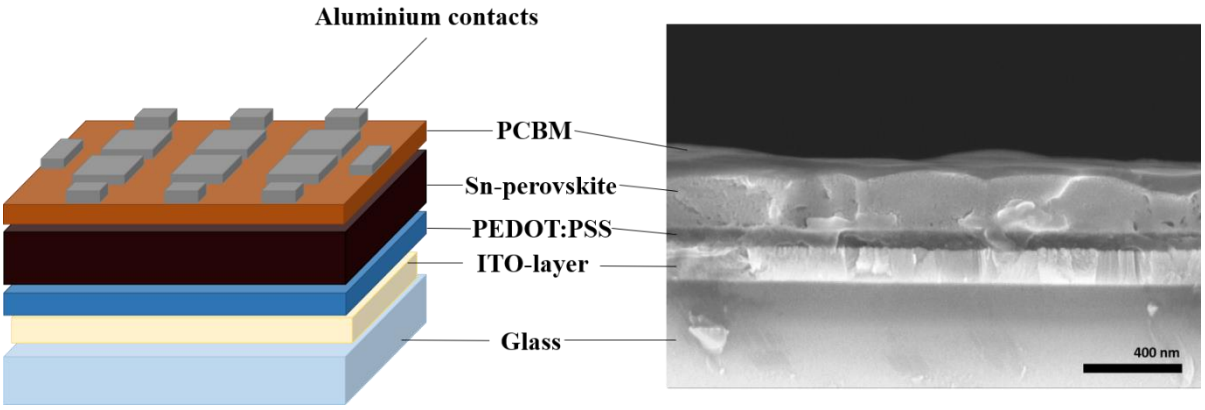


**Figure 33** *Principle solar cell set-up with the architecture "Glass-ITO-PEDOT:PSS-Perovskite-PCBM-Al". The right image shows the recorded SEM image of the reference $FASnI_3$ solar cell.*

In figure 33 the general set-up of an inverted tin based perovskite solar cell is shown. The system shows the structure "Glass-ITO/PEDOT:PSS/Perovskite/$PC_{60}BM$/Al". In this case, an indium tin oxide (ITO) layer was used as anode material, which collects all the holes produced in the material. The hole transport layer (HTL) is represented by PEDOT:PSS. In this work different single cation and double cation Sn-perovskites were used as light absorbing materials in the perovskite solar cell. The $PC_{60}BM$ layer has the function of an electron transport layer (ETL), which conducts all the electrons to the electron collecting electrode, made of aluminium.

In the end of the work also a bathocuproin (BCP) layer was integrated into the device architecture. Therefore, BCP was applied onto the PCBM layer via thermal evaporation, followed by the thermal evaporation of aluminium.

## 4.3 Device fabrication procedure

In the following section the whole fabrication procedure towards a fully functional solar cell device is described. Figure 34 shows a general fabrication scheme with all important parameters, dripping times and annealing temperatures. The solar cell fabrication was carried out at ambient atmosphere and in an MBraun glovebox.

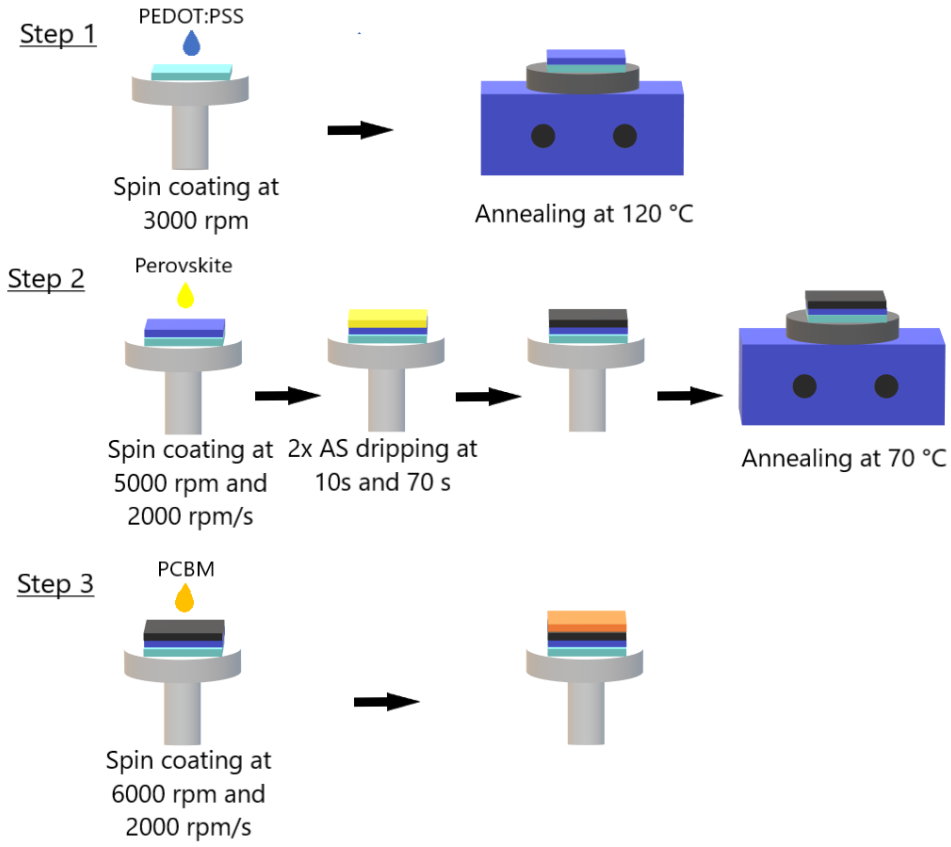


**Figure 34** *Scheme for the preparation of perovskite solar cells.* ***Step 1*** *Spin coating of PEDOT:PSS at 3000 rpm in ambient atmosphere and annealing at 120 °C inside the glove box* ***Step 2*** *Spin coating of the perovskite layer at 5000 rpm and 2000 rpm/s acceleration; chlorobenzene antisolvent dripping at 10s and 70s during spin coating; annealing at 70 °C* ***Step 3*** *Spin coating of the $PC_{60}BM$ layer at 6000 rpm and 2000 rpm/s*

### 4.3.1 Cleaning of the ITO-glass substrates

The preparation of the substrates is an essential step in the device fabrication. The cleaning of the substrates was carried out by careful removal of dirt and particles on the surface using distilled water and acetone, followed by 30 minutes ultrasonication at 40 °C in an isopropanol bath. Afterwards, the substrates were blown with nitrogen gas and placed in an oxygen plasma etching device for three minutes to remove organic residues and provide a more polar surface for better adhesion of the following PEDOT:PSS layer.

### 4.3.2 Preparation of hole transport layer (HTL)

The PEDOT:PSS solution was put in an ultrasonic bath for 30 min at 40 °C and was filtered afterwards. Directly after the etching process 50 µL of the ultrasonicated and filtered PEDOT:PSS solution were applied on the Glass-ITO substrates via spin coating at 3000 rpm for 30 seconds at ambient atmosphere, followed by an annealing step at 120 °C for 20 minutes in the glove box. All further device fabrication steps were also carried out in an inert nitrogen atmosphere in the glove box.

### 4.3.3 Preparation of the absorber layer

First, the perovskite precursor solution was prepared in the glovebox. Therefore, tin iodide ($SnI_2$), the respective A-site cationic salts, as well as, 10 mol% tin fluoride ($SnF_2$) were dissolved in a 4:1 mixture of DMF:DMSO and were stirred overnight in the glove box. The solution should have a 1:1 molar ratio of $SnI_2$ to the respective A-site cationic salt mixture. In the end it should be obtained a 1M solution of $SnI_2$ and a 1M solution of the A-site cationic salts in the respective ratios. In this work the salts FAI, CsI, RbI. $PIPI_2$ and HAI were used. One day afterwards, 50 µL of the filtered perovskite solution were spin-coated on the PEDOT:PSS surface with a rotational speed of 5000 rpm and an acceleration of 2000 rpm/s for two minutes. The crystallization of the thin film was induced by two times antisolvent dripping with chlorobenzene at 10 s and again 70 s. The AS was added always fast from a distance of approximately 4.5 cm. Directly after the spin coating procedure, the substrates were placed on the hot heating plate and annealed at 70°C for 20 min.

### 4.3.4 Preparation of the electron transport layer (ETL)

A 20 mg/ml $PC_{60}BM$ solution was prepared in chlorobenzene and stirred overnight. The solution was filtered on the next day and 30 µL of the $PC_{60}BM$ solution were applied onto the perovskite surface by spin coating at 6000 rpm and 2000 rpm/s for one minute.

### 4.3.5 Thermal deposition of the cathode

To produce the cathode, aluminium with a film thickness of 100 nm was deposited on the substrates by thermal evaporation. Before, two contacts between the electrodes must be provided by scratching free two positions along the ITO layer. The substrates were placed in a stator to produce six solar cells on one substrate. For the evaporation, tungsten coils filled with aluminium wire were used. It was always worked under a vacuum of at least $1*10^{-5}$ mbar.

## 4.4 Characterization methods

The solar cells were characterized by *JV*-measurements, profilometry, UV-VIS spectroscopy, light microscopy, SEM, XRD and EQE measurements.

### 4.4.1 Current density-voltage (*JV*) measurements

For all solar cells, *JV*-curves were recorded under inert nitrogen atmosphere inside the glove box. The measurement was carried out with a Keithley 2400 source meter coupled to a LabVIEW software. The solar cells were measured under a constant irradiation of 100 $mW*cm^{-2}$, which corresponds to an irradiation of one sun, by usage of a Dedolight DLH400D lamp. The used measurement parameters are listed in table 17. Most of the cells described in this thesis were measured with a mask that had an area of 0.0702 $cm^2$. Cells that were measured without a mask showed an area of 0.09 $cm^2$ and are indicated in the results and discussion part.

**Table 17** *Parameters for JV-measurements*

| Function | Voltage/current |
|---|---|
| Start Lv | 1000 mV |
| Stop Lv | -100 mV |
| Compliance | 100 mA |
| Nr. of points | 100 |
| Overwrite max | 500 |
| Delay | 100 ms |
| Step widths | -0.011 |

The calculated scan rate was 56.4 $mV*s^{-1}$. To see if the cells are properly working, light as well as dark measurements were carried out all the time. Later, also measurements into backward and forward direction were done to investigate the hysteresis behavior. In general, most of cells were measured on the first day after fabrication and sometimes again on the second day after fabrication. However, most of the results shown in the results and discussion part were recorded on the first day.

### 4.4.2 Profilometry

During the device fabrication it was necessary to investigate the layer thicknesses in the solar cell device. Therefore, a Bruker DektakXT profilometer was used. Except of the ETL, all layers were measured over a range of 1000 µm for 10 s with a stylus radius of 6.5 µm and a stylus force of 3 mg. The ETL showed a softer surface as the others and was therefore, measured with a stylus force of 2 mg to receive a result that is closer at the true layer thickness. To measure the layer thickness, the surface was scratched with a blade and then scanned with a stylus in a 90° angle to the scratches.

### 4.4.3 UV-VIS spectroscopy

The optical characterization of the layers was carried out with a LAMBDA 35 PerkinElmer UV-VIS spectrometer and a Scan LAMBDA 35 software.

The layers to be measured were always prepared on cleaned glass substrates. The perovskite layers which should be investigated, were prepared on glass-PEDOT:PSS substrates to provide a perovskite thin film crystallization similar to the perovskite film in the solar cell. The measured substrates were corrected by the absorption value of glass or glass-PEDOT:PSS depending on the investigated layer.

### 4.4.4 Light microscopy and photographs

The surfaces of the layers were investigated with an Olympus BX60 light microscope, which was coupled with an Olympus E520 camera to take pictures. The layers were investigated with different magnifications in bright and dark field mode.

### 4.4.5 Scanning electron microscopy (SEM)

The SEM images of the samples were taken at the Austrian Institute of Technology by Dr. Theodoros Dimopoulos. It was used a Supra 40 scanning electron microscope from Carl Zeiss, which utilizes a field emission electron source with an acceleration voltage of 5 kV. Furthermore, the SEM device possesses an in lens secondary electron detector.

There were taken top view images of the $FASnI_3$, $FA_{0.98}PIP_{0.02}SnI_3$ and the $FA_{0.95}HA_{0.05}SnI_3$ perovskite absorber layers and cross section images of a fully functional $FASnI_3$ solar cell. The perovskites for the top view investigation were produced on glass substrates spin coated with PEDOT:PSS, while the cross section shows a complete solar cell prepared in ITO-glass substrates. The production of the cells was carried out exactly the same as described in section 1.3.

### 4.4.6 External quantum efficiency measurement (EQE)

External Quantum Efficiency measurements were carried out by usage of a 75 W xenon lamp (550 nm), a Multimode 4-monochromator by AMKO, a LogIn Amplifier by Stanford Research Systems (Model: SR830 DSN) and a Keithley 2400 source meter. During measurement the monochromatic light was chopped at a frequency of 30 Hz. The sample was scanned over a wavelength range from 380 nm to 1100 nm. For the calibration of the device a spectral calibrated photodiode by the Newport Corporation (8181-UV/DB) was used.

# 5 Conclusion and Outlook

Over the last years, lead perovskite solar cells attracted high attention, due to their very fast increase in power conversion efficiencies. However, the large-scale application of lead PSCs remains challenging due to its high toxicity. Therefore, also alternative elements were explored. Especially, tin PSCs provided promising results in the past.[53,74]

The main focus of this work was on the investigation of a stable reference system and new double cation tin-based perovskite materials. For that purpose, different single cation perovskites like $FASnI_3$, $CsSnI_3$ and $RbSnI_3$ were tested. Among all these materials the $FASnI_3$ PSC seemed to be the most promising one and was further investigated and improved. Furthermore, two different double cation Sn-perovskites with variating amounts of piperazine-1,4-diium iodide and n-hexylammonium iodide in a mixture with formamidinium iodide were tested. All investigated perovskites were processed via a solution-based spin coating procedure with an AS dripping step and were integrated into an inverted cell set-up that consisted of "Glass-ITO/PEDOT:PSS/Perovskite/$PC_{60}BM$/Aluminium".

First of all, the $FASnI_3$ perovskite was investigated and improved by varying the perovskite film formation. For that purpose, the AS dripping times, hot AS dripping, hot substrate spinning and variations in the perovskite layer thicknesses were investigated. It was shown that AS dripping at 10 s and again 70 s led to very smooth, reflective surfaces and consequently, to better overall cell performances compared to other dripping times. Therefore, the AS dripping procedure was adopted for further experiments. In contrast, hot AS dripping and HSS were not further investigated since, they provided either grey, dull or pinhole rich perovskite layers that showed worse performances compared to the standard procedure. Moreover, the layer thicknesses of the perovskite were varied by using different spin coating speeds. The best results were obtained by spin coating speeds between 5000 (standard procedure) and 8000 rpm, however the differences were rather small. In literature, the positive influence of $SnF_2$ on the cell performance and the perovskite morphology is of high interest and was discussed very much over the last years.[10,64,68] Therefore, different $SnF_2$ concentrations ranging between 5 mol% and 20 mol% were added to the perovskite precursor solution and it was investigated the change in PCE for a $FASnI_3$ based PSC. Due to reproducibility issues, this experiment was carried out many times, always leading to the result that an addition of 10 mol% is most probably the best amount for the perovskite film fabrication. Since, pyrazine was found to complex $SnF_2$ and hence, improves the reproducibility and PCE, also additions of pyrazine to the solution were tested, leading to no results. The best $FASnI_3$ PSC reached a PCE of 3.55% and high quantum efficiency of 72%. However, the average of the investigated $FASnI_3$ cells showed worse results that are distributed over a large range.

Moreover, other single cation perovskites like $CsSnI_3$ and $RbSnI_3$ with the same cell set-up were fabricated. The fabrication of the pure $RbSnI_3$ perovskite resulted in crystallization of a photoinactive yellow crystal structure, that cannot be changed by increase in temperature. This result was also

consistent with literature data, that describes $RbSnI_3$ as a one-dimensional yellow crystal structure.[98] The other investigated perovskite $CsSnI_3$, showed interesting results in literature[53] but cannot reach high efficiencies with the used inverted cell set-up used during this work. Since, $CsSnI_3$ itself showed a black reflective thin film, it can be suggested that the fabricated perovskite is the photoactive orthorhombic B-γ-$CsSnI_3$ phase. The measured X-ray patterns are is accordance with literature.[104] Thus, it seems likely that the formed perovskite was not the problem, but the chosen set-up was not fitting for that type of perovskite.

Furthermore, two different double cation perovskite materials were tested. Both materials were based on a $FASnI_3$ perovskite with small additions of piperazine-1,4-diium iodide ($PIPI_2$) or n-hexylammonium iodide (HAI). The best PCE values for these systems were obtained with $PIP_{0.02}FA_{0.98}SnI_3$ and $HA_{0.05}FA_{0.95}SnI_3$, which were investigated very detailed. In general, the absorption behavior for that materials, were relatively similar to $FASnI_3$, resulting also in very similar bandgaps of 1.39 eV and 1.38 eV respectively ($FASnI_3$ showed an experimental bandgap of 1.37 eV). However, the XRD data provided very different results for both new materials. The insertion of PIP into the crystal lattice cannot be proven, since the data were not deviating from the XRD data of pure $FASnI_3$. On the other hand, the second perovskite showed less reflexes compared to $FASnI_3$, meaning that the crystals must be oriented into preferred directions. Comparison with literature provided that the mixed HA Sn-perovskite formed most probably a 2D/3D layered perovskite structure that can also be found for mixed PEA Sn-perovskites.[76] Furthermore, these layers were integrated into an inverted cell set-up and characterized with JV-measurements. The best results for both types were achieved after MPP tracking over more than one hour resulting in a PCE of 1.49% for $PIP_{0.02}FA_{0.98}SnI_3$ (46% FF, -10.8 $mA*cm^{-2}$ $J_{SC}$, 0.30 V $V_{OC}$) and a PCE of 2.31% (53% FF, -14.6 $mA*cm^{-2}$, 0.3 V $V_{OC}$) for $HA_{0.05}FA_{0.95}SnI_3$. These results are also into accordance with the recorded SEM images of these perovskite layers, which provided a better film morphology of the HA sample. To sum up, it can be said that n-hexylammonium iodide was successfully integrated into the perovskite crystal structure and was able to reach efficiencies up to 2.31% in an inverted cell set-up, which is a promising result for this new material. The integration of piperazine-1,4-diium in contrast, did not yield the expected result.

Another interesting experiment was the integration of salt interlayers like FAI, $SnI_2$, CsI, RbI, HAI, $PIPI_2$ and PEAI between PEDOT:PSS and $FASnI_3$. Nearly all interlayers provided very good results compared to the $FASnI_3$ reference. The only exception was piperazine-1,4-diium iodide, which showed a worse cell performance. These results are very promising and should be investigated in future research.

All these results provided important information for further investigations of Sn PSCs. Especially, the atmosphere in the glovebox and the solvent atmosphere, which develops during the work, were found to have an impact on the cell performance. The bad reproducibility due to the instability of $Sn^{2+}$ remains a challenging problem for further research and must be fixed.

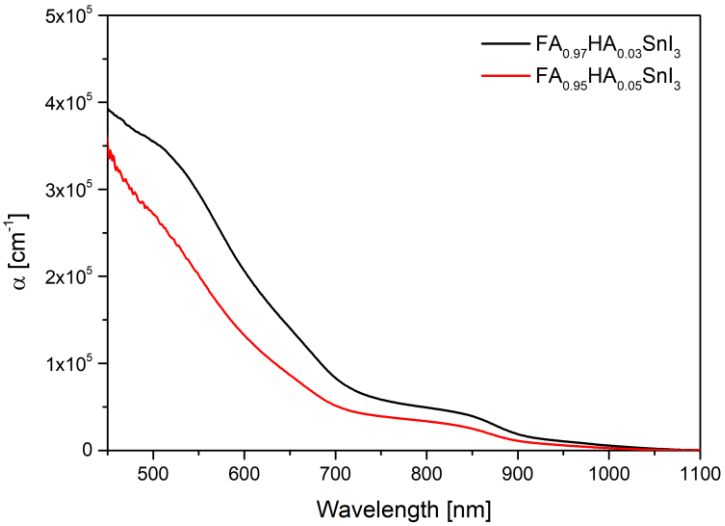


**Figure 35** *Absorptionspectra of different HAI concentrations.*

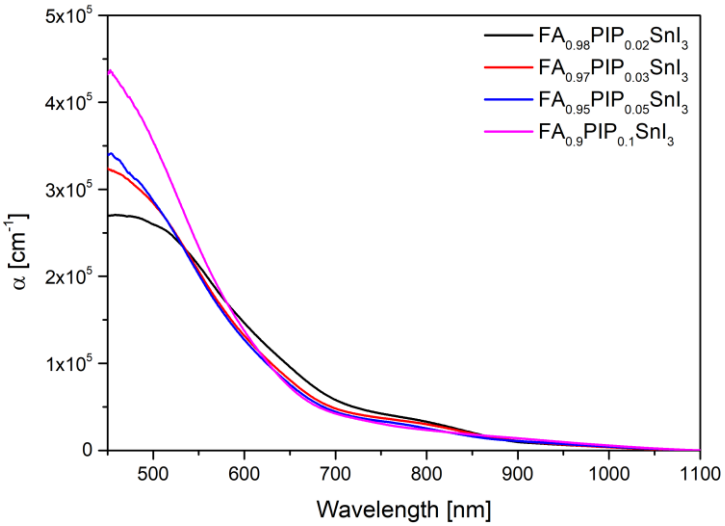


**Figure 36** *Absorptionspectra of different $PIPI_2$ concentrations.*

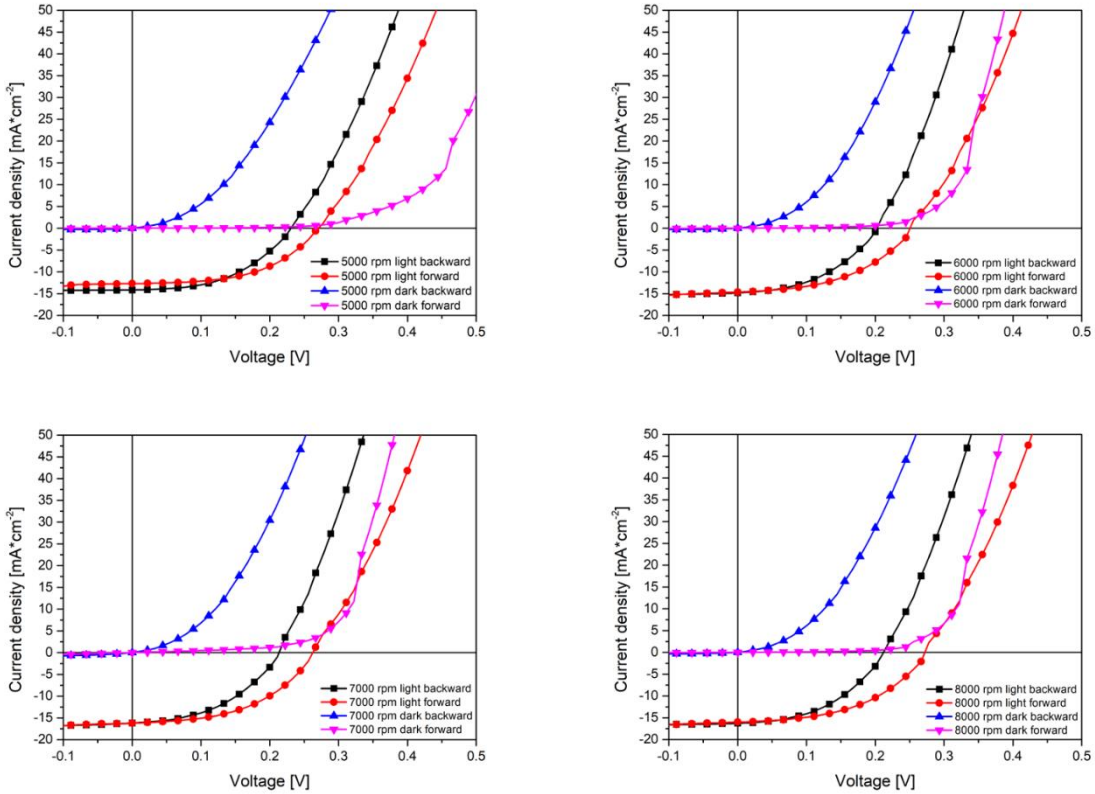


**Figure 37** *Hysteresis behavior of $FASnI_3$, which was prepared with different spin coating parameters.*

# 7 List of Figures

**Figure 37** Hysteresis behavior of $FASnI_3$, which was prepared with different spin coating parameters.

**62**

# 8 List of Tables

# 9 Literature


(1) Global energy demand rose by 2.3% in 2018, its fastest pace in the last decade. https://www.iea.org/newsroom/news/2019/march/global-energy-demand-rose-by-23-in-2018-its-fastest-pace-in-the-last-decade.html (accessed Apr 26, 2019).

(2) IPCC: Summary for Policymakers. *In: Climate Change 2013: The Physical Science Basis.Contibution of Working Group I to the Fifth Assessment Report of the Intergovernmental Panel on Climate Change* [Stocker,T.F., D. Qin, G.-K. Plattner, M. Tignor, S.K. Allen, J. Boschung, A. Nauels, Y. Xia, V. Bex and P.M. Midgley (eds.)]. Cambridge University Press: Cambridge, United Kingdom and New York, 2013.

(3) WEO Model. https://www.iea.org/weo/weomodel/ (accessed Apr 25, 2019).

(4) Glossary. https://www.iea.org/about/glossary/ (accessed Apr 26, 2019).

(5) Renewables 2018. https://www.iea.org/renewables2018/ (accessed Apr 27, 2019).

(6) Quaschning, V. Regenerative Energiesysteme Technologie-Berechnung-Simulation, 9. Auflage; Carl Hanser Verlag: München, 2015; pp 36-37.

(7) Kalogirou, S. A. Solar Energy Engineering - Processes and Systems, 1. edition.; Academic Press: Burlington, California, London, 2009.

(8) Mesquita, I.; Andrade, L.; Mendes, A. Perovskite Solar Cells: Materials, Configurations and Stability. *Renew. Sustain. Energy Rev.* **2018**, *82*, 2471–2489.

(9) Marinova, N.; Valero, S.; Delgado, J. L. Organic and Perovskite Solar Cells: Working Principles, Materials and Interfaces. *J. Colloid Interface Sci.* **2017**, *488*, 373–389.

(10) Gupta, S.; Cahen, D.; Hodes, G. How SnF2 Impacts the Material Properties of Lead-Free Tin Perovskites. *J. Phys. Chem. C* **2018**, *122*, 13926–13936.

(11) Askeland, D. R.; Wright, W. J. Electronic Materials. In *The Science and Engineering of Materials*, 7. edition; Cengage Learning: Boston, 2015; pp 680–699.

(12) Wesselak, V.; Voswinckel, S. Die Physik der Solarzelle. In *Photovoltaik - Wie Sonne zu Strom wird*, 2. Auflage; Springer-Verlag: Berlin Heidelberg, 2012, 2016; pp 29–43.

(13) Verlinden, P. Doping, Diffusion, and Defects in Solar Cells. In *Photovoltaic Solar Energy - From Fundamentals to Applications*; Reinders, A., Verlinden, P., Van Sark, W., Freundlich, A., Eds.; John Wiley and Sons, Ltd: Chichester, West Sussex, United Kingdome, 2017; pp 21–31.

(14) Mertens, K. Grundlagen der Halbleiterphysik. In *Photovoltaik - Lehrbuch zu Grundlagen, Technologie und Praxis*, 4., aktualisierte Auflage; Carl Hanser Verlag: München, 2018; pp 64–89.

(15) Correa-Baena, J.-P.; Saliba, M.; Buonassisi, T.; Grätzel, M.; Abate, A.; Tress, W.; Hagfeldt, A. Promises and Challenges of Perovskite Solar Cells. *Science.* **2017**, *358*, 739–744.

(16) What is a PIN Diode? Definition, Construction, Working, Characteristics and applications of PIN Diode - Electronics Desk. https://electronicsdesk.com/pin-diode.html (accessed May 27, 2019).
(17) PIN Diode | Electrical4U. https://www.electrical4u.com/ (accessed May 27,2019)
(18) RP Photonics Encyclopedia - p-i-n photodiodes, PIN photodiode. https://www.rp-photonics.com/p_i_n_photodiodes.html (accessed May 27, 2019).
(19) Photodiode - Symbol, Working and Types - Diode. https://www.physics-and-radio-electronics.com/electronic-devices-and-circuits/semiconductor-diodes/photodiodesymboltypes.html (accessed May 27, 2019).
(20) PIN Diode Working Characteristics and Its Applications. https://www.elprocus.com/pin-diode-basics-working-applications/ (accessed May 27, 2019).
(21) Dittrich, T. Basic Characteristics and Characterization of Solar Cells. In *Materials Concepts for Solar Cells*, 2. edition; World Scientific, 2018; pp 3–43.
(22) Stadler, A. Photonik der Solarzellen - Innovative Messverfahren für moderne Solarzellen, 2. Auflage; Springer Vieweg: Wiesbaden, 2017; pp 1-129.
(23) Air Mass. https://www.pveducation.org/pvcdrom/properties-of-sunlight/air-mass (accessed May 27, 2019).
(24) Introduction to Solar Radiation. https://www.newport.com/t/introduction-to-solar-radiation (accessed May 27, 2019).
(25) Dye Sensitized Solar Cells-Dye Solar Cells-DSSC-DSC. https://www.gamry.com/application-notes/physechem/dssc-dye-sensitized-solar-cells/ (accessed May 17, 2019).
(26) Mertens, K. Aufbau und Wirkungsweise der Solarzelle. In *Photovoltaik - Lehrbuch zu Grundlagen, Technologie und Praxis*, 4., aktualisierte Auflage; Carl Hanser Verlag: München, 2018; pp 90–122.
(27) Short-Circuit Current | PVEducation. https://www.pveducation.org/pvcdrom/solar-cell-operation/short-circuit-current (accessed May 17, 2019).
(28) Open-Circuit Voltage | PVEducation. https://www.pveducation.org/pvcdrom/solar-cell-operation/open-circuit-voltage (accessed May 17, 2019).
(29) Fill Factor | PVEducation. https://www.pveducation.org/pvcdrom/solar-cell-operation/fill-factor (accessed May 17, 2019).
(30) Solar Cell Efficiency | PVEducation. https://www.pveducation.org/pvcdrom/solar-cell-operation/solar-cell-efficiency (accessed May 17, 2019).
(31) Park, N. G. Perovskite Solar Cells: An Emerging Photovoltaic Technology. *Mater. Today* **2015**, *18*, 65–72.
(32) Jung, H. S.; Park, N. G. Perovskite Solar Cells: From Materials to Devices. *Small* **2015**, *11*, 10–25.

(33) Perovskite Breakthrough Shows Importance of Added Chemical Compound in Boosting Efficiency | News | NREL. https://www.nrel.gov/news/program/2019/perovskite-breakthrough-shows-importance-of-added-chemical-compound-in-boosting-efficiency.html (accessed May 27, 2019).

(34) Shi, Z.; Jayatissa, A. H. Perovskites-Based Solar Cells: A Review of Recent Progress, Materials and Processing Methods. *Materials.* **2018**, *11*, 729.

(35) Hoefler, S. F.; Trimmel, G.; Rath, T. Progress on Lead-Free Metal Halide Perovskites for Photovoltaic Applications: A Review. *Monatshefte fur Chemie* **2017**, *148*, 795–826.

(36) Zhao, Y.; Zhu, K. Organic-Inorganic Hybrid Lead Halide Perovskites for Optoelectronic and Electronic Applications. *Chem. Soc. Rev.* **2016**, *45*, 655–689.

(37) Li, D.; Shi, J.; Xu, Y.; Luo, Y.; Wu, H.; Meng, Q. Inorganic-Organic Halide Perovskites for New Photovoltaic Technology. *Natl. Sci. Rev.* **2018**, *5*, 559–576.

(38) Zhang, H.; Li, R.; Liu, W.; Zhang, M.; Guo, M. Research Progress in Lead-Less or Lead-Free Three-Dimensional Perovskite Absorber Materials for Solar Cells. *Int. J. Miner. Metall. Mater.* **2019**, *26*, 387–403.

(39) Gong, J.; Guo, P.; Benjamin, S. E.; Van Patten, P. G.; Schaller, R. D.; Xu, T. Cation Engineering on Lead Iodide Perovskites for Stable and High-Performance Photovoltaic Applications. *J. Energy Chem.* **2018**, *27*, 1017–1039.

(40) A. Kojima; K. Teshima; Y. Shirai; T. Miyasaka. Organometal Halide Perovskites as Visible-Light Sensitizers for Photovoltaic Cells. *J. Am. Chem. Soc.* **2009**, 131, 6050–6051.

(41) Im, J. H.; Lee, C. R.; Lee, J. W.; Park, S. W.; Park, N. G. 6.5% Efficient Perovskite Quantum-Dot-Sensitized Solar Cell. *Nanoscale* **2011**, *3*, 4088–4093.

(42) Kim, H.; Lee, C.; Im, J.; Lee, K.; Moehl, T.; Marchioro, A.; Moon, S.; Humphry-baker, R.; Yum, J.; Moser, J. E.; et al. Lead Iodide Perovskite Sensitized All-Solid-State Submicron Thin Film Mesoscopic Solar Cell with Efficiency Exceeding 9%. *Sci. Rep.* **2012**, *2*:591, 1-7.

(43) Heo, J. H.; Im, S. H.; Noh, J. H.; Mandal, T. N.; Lim, C.-S.; Chang, J. A.; Lee, Y. H.; Kim, H.; Sarkar, A.; Nazeeruddin, M. K.; et al. Efficient Inorganic–Organic Hybrid Heterojunction Solar Cells Containing Perovskite Compound and Polymeric Hole Conductors. *Nat. Photonics* **2013**, *7*, 486–491.

(44) Son, D. Y.; Lee, J. W.; Choi, Y. J.; Jang, I. H.; Lee, S.; Yoo, P. J.; Shin, H.; Ahn, N.; Choi, M.; Kim, D.; et al. Self-Formed Grain Boundary Healing Layer for Highly Efficient CH3 NH3 PbI3 Perovskite Solar Cells. *Nat. Energy* **2016**, *1*, 16081.

(45) Momblona, C.; Gil-Escrig, L.; Bandiello, E.; Hutter, E. M.; Sessolo, M.; Lederer, K.; Blochwitz-Nimoth, J.; Bolink, H. J. Efficient Vacuum Deposited p-i-n and n-i-p Perovskite Solar Cells Employing Doped Charge Transport Layers. *Energy Environ. Sci.* **2016**, *9*, 3456–3463.

(46) Zhou, D.; Zhou, T.; Tian, Y.; Zhu, X.; Tu, Y. Perovskite-Based Solar Cells: Materials, Methods, and Future Perspectives. *J. Nanomater.* **2018**, *2018*, 8148072.

(47) Anaraki, E. H.; Kermanpur, A.; Steier, L.; Domanski, K.; Matsui, T.; Tress, W.; Saliba, M.; Abate, A.; Grätzel, M.; Hagfeldt, A.; et al. Highly Efficient and Stable Planar Perovskite Solar Cells by Solution-Processed Tin Oxide. *Energy Environ. Sci.* **2016**, *9*, 3128–3134.

(48) Saliba, M.; Matsui, T.; Bella, F.; Domanski, K.; Seo, J.-Y.; Ummadisingu, A.; Zakeeruddin, S. M.; Correa-Baena, J. P.; Tress, W. R.; Abate, A.; et al. Incorporation of Rubidium Cations into Perovskite Solar Cells Improves Photovoltaic Performance. *Science* **2016**, *354*, 206–209.

(49) Yang, W. S.; Park, B.-W.; Jung, E. H.; Jeon, N. J.; Kim, Y. C.; Lee, D. U.; Shin, S. S.; Seo, J.; Kim, E. K.; Noh, J. H.; et al. Iodide Management in Formamidinium-Lead-Halide-Based Perovskite Layers for Efficient Solar Cells. *Science* **2017**, *356*, 1376–1379.

(50) Fu, H. Review of Lead-Free Halide Perovskites as Light-Absorbers for Photovoltaic Applications: From Materials to Solar Cells. *Sol. Energy Mater. Sol. Cells* **2019**, *193*, 107–132.

(51) Liang, L.; Gao, P. Lead-Free Hybrid Perovskite Absorbers for Viable Application: Can We Eat the Cake and Have It Too? *Adv. Sci.* **2018**, *5*, 1700331.

(52) Abate, A. Perovskite Solar Cells Go Lead Free. *Joule* **2017**, *1*, 659–664.

(53) Song, T. Bin; Yokoyama, T.; Aramaki, S.; Kanatzidis, M. G. Performance Enhancement of Lead-Free Tin- Based Perovskite Solar Cells with Reducing Atmosphere-Assisted Dispersible Additive. *ACS Energy Lett.* **2017**, *2*, 897–903.

(54) Ortiz-Cervantes, C.; Carmona-Monroy, P.; Solis-Ibarra, D. Two-Dimensional Halide Perovskites in Solar Cells: 2D or Not 2D? *ChemSusChem* **2019**, *12*, 1560–1575.

(55) Liu, C.; Li, W.; Fan, J.; Mai, Y. A Brief Review on the Lead Element Substitution in Perovskite Solar Cells. *J. Energy Chem.* **2018**, *27*, 1054–1066.

(56) Chung, I.; Lee, B.; He, J.; Chang, R. P. H.; Kanatzidis, M. G. All-Solid-State Dye-Sensitized Solar Cells with High Efficiency. *Nature* **2012**, *485*, 486–489.

(57) Chung, I.; Song, J. H.; Im, J.; Androulakis, J.; Malliakas, C. D.; Li, H.; Freeman, A. J.; Kenney, J. T.; Kanatzidis, M. G. CsSnI3: Semiconductor or Metal? High Electrical Conductivity and Strong Near-Infrared Photoluminescence from a Single Material. High Hole Mobility and Phase-Transitions. *J. Am. Chem. Soc.* **2012**, *134*, 8579–8587.

(58) Kumar, M. H.; Dharani, S.; Leong, W. L.; Boix, P. P.; Prabhakar, R. R.; Baikie, T.; Shi, C.; Ding, H.; Ramesh, R.; Asta, M.; et al. Lead-Free Halide Perovskite Solar Cells with High Photocurrents Realized Through Vacancy Modulation. *Adv. Mater.* **2014**, *26*, 7122–7127.

(59) Noel, N. K.; Stranks, S. D.; Abate, A.; Wehrenfennig, C.; Guarnera, S.; Haghighirad, A. A.; Sadhanala, A.; Eperon, G. E.; Pathak, S. K.; Johnston, M. B.; et al. Lead-Free Organic-Inorganic Tin Halide Perovskites for Photovoltaic Applications. *Energy Environ. Sci.* **2014**, *7*, 3061–3068.

(60) Hao, F.; Stoumpos, C. C.; Guo, P.; Zhou, N.; Marks, T. J.; Chang, R. P. H.; Kanatzidis, M. G. Solvent-Mediated Crystallization of CH3NH3SnI3 Films for Heterojunction Depleted Perovskite Solar Cells. *J. Am. Chem. Soc.* **2015**, *137*, 11445–11452.

(61) Stoumpos, C. C.; Malliakas, C. D.; Kanatzidis, M. G. Semiconducting Tin and Lead Iodide Perovskites with Organic Cations: Phase Transitions, High Mobilities, and Near-Infrared Photoluminescent Properties. *Inorg. Chem.* **2013**, *52*, 9019–9038.

(62) Konstantakou, M.; Stergiopoulos, T. A Critical Review on Tin Halide Perovskite Solar Cells. *J. Mater. Chem. A* **2017**, *5*, 11518–11549.

(63) Koh, T. M.; Krishnamoorthy, T.; Yantara, N.; Shi, C.; Leong, W. L.; Boix, P. P.; Grimsdale, A. C.; Mhaisalkar, S. G.; Mathews, N. Formamidinium Tin-Based Perovskite with Low Eg for Photovoltaic Applications. *J. Mater. Chem. A* **2015**, *3*, 14996–15000.

(64) Lee, S. J.; Shin, S. S.; Kim, Y. C.; Kim, D.; Ahn, T. K.; Noh, J. H.; Seo, J.; Seok, S. Fabrication of Efficient Formamidinium Tin Iodide Perovskite Solar Cells through SnF2 - Pyrazine Complex. *J. Am. Chem. Soc.* **2016**, *138*, 3974–3977.

(65) Liao, W.; Zhao, D.; Yu, Y.; Grice, C. R.; Wang, C.; Cimaroli, A. J.; Schulz, P.; Meng, W.; Zhu, K.; Xiong, R.-G.; et al. Lead-Free Inverted Planar Formamidinium Tin Triiodide Perovskite Solar Cells Achieving Power Conversion Efficiencies up to 6.22%. *Adv. Mater.* **2016**, *28*, 9333–9340.

(66) Gupta, S.; Bendikov, T.; Hodes, G.; Cahen, D. CsSnBr3, a Lead-Free Halide Perovskite for Long-Term Solar Cell Application: Insights on SnF2 Addition. *ACS Energy Lett.* **2016**, *1*, 1028–1033.

(67) Moghe, D.; Wang, L.; Traverse, C. J.; Redoute, A.; Sponseller, M.; Brown, P. R.; Bulović, V.; Lunt, R. R. All Vapor-Deposited Lead-Free Doped CsSnBr3 Planar Solar Cells. *Nano Energy* **2016**, *28*, 469–474.

(68) Xiao, M.; Gu, S.; Zhu, P.; Tang, M.; Zhu, W.; Lin, R.; Chen, C.; Xu, W.; Yu, T.; Zhu, J. Tin-Based Perovskite with Improved Coverage and Crystallinity through Tin-Fluoride-Assisted Heterogeneous Nucleation. *Adv. Opt. Mater.* **2018**, *6*, 1700615.

(69) Song, T.-B.; Yokoyama, T.; Logsdon, J.; Wasielewski, M. R.; Aramaki, S.; Kanatzidis, M. G. Piperazine Suppresses Self-Doping in CsSnI 3 Perovskite Solar Cells. *ACS Appl. Energy Mater.* **2018**, *1*, 4221–4226.

(70) Zhao, Z.; Gu, F.; Li, Y.; Sun, W.; Ye, S.; Rao, H.; Liu, Z.; Bian, Z.; Huang, C. Mixed-Organic-Cation Tin Iodide for Lead-Free Perovskite Solar Cells with an Efficiency of 8.12%. *Adv. Sci.* **2017**, *4*, 1700204.

(71) Liu, X.; Yan, K.; Tan, D.; Liang, X.; Zhang, H.; Huang, W. Solvent Engineering Improves Efficiency of Lead-Free Tin-Based Hybrid Perovskite Solar Cells beyond 9%. *ACS Energy Lett.* **2018**, *3*, 2701–2707.

(72) Ke, W.; Stoumpos, C. C.; Spanopoulos, I.; Mao, L.; Chen, M.; Wasielewski, M. R.; Kanatzidis, M. G. Efficient Lead-Free Solar Cells Based on Hollow {en}MASnI3 Perovskites. *J. Am. Chem. Soc.* **2017**, *139*, 14800–14806.

(73) Ke, W.; Priyanka, P.; Vegiraju, S.; Stoumpos, C. C.; Spanopoulos, I.; Soe, C. M. M.; Marks, T. J.; Chen, M. C.; Kanatzidis, M. G. Dopant-Free Tetrakis-Triphenylamine Hole Transporting Material for Efficient Tin-Based Perovskite Solar Cells. *J. Am. Chem. Soc.* **2018**, *140*, 388–393.

(74) Ke, W.; Stoumpos, C. C.; Spanopoulos, I.; Chen, M.; Wasielewski, M. R.; Kanatzidis, M. G. Diammonium Cations in the FASnI3 Perovskite Structure Lead to Lower Dark Currents and More Efficient Solar Cells. *ACS Energy Lett.* **2018**, *3*, 1470–1476.

(75) Jokar, E.; Chien, C. H.; Tsai, C. M.; Fathi, A.; Diau, E. W. G. Robust Tin-Based Perovskite Solar Cells with Hybrid Organic Cations to Attain Efficiency Approaching 10%. *Adv. Mater.* **2019**, *31*, 1804835

(76) Liao, Y.; Liu, H.; Zhou, W.; Yang, D.; Shang, Y.; Shi, Z.; Li, B.; Jiang, X.; Zhang, L.; Quan, L. N.; et al. Highly Oriented Low-Dimensional Tin Halide Perovskites with Enhanced Stability and Photovoltaic Performance. *J. Am. Chem. Soc.* **2017**, *139*, 6693–6699.

(77) Shao, S.; Liu, J.; Portale, G.; Fang, H. H.; Blake, G. R.; ten Brink, G. H.; Koster, L. J. A.; Loi, M. A. Highly Reproducible Sn-Based Hybrid Perovskite Solar Cells with 9% Efficiency. *Adv. Energy Mater.* **2018**, *8*, 1702019.

(78) Chen, K.; Wu, P.; Yang, W.; Su, R.; Luo, D.; Yang, X.; Tu, Y. Low-Dimensional Perovskite Interlayer for Highly Efficient Lead-Free Formamidinium Tin Iodide Perovskite Solar Cells. *Nano Energy* **2018**, *49*, 411–418.

(79) Friesenbichler, B. Investigation of Different Cations in Organic/Inorganic Tin Halide Perovskites for Solar Cell Applications. Master Thesis, Graz University of Technology, 2017.

(80) Handl, J. Optimization of Organic/Inorganic Tin Halide Perovskite Solar Cells. Master Thesis, Graz University of Technology, 2018.

(81) Rath, T.; Handl, J.; Weber, S.; Friesenbichler, B.; Fürk, P.; Troi, L.; Dimopoulos, T.; Kunert, B.; Resel, R.; Trimmel, G. Photovoltaic Properties of a Triple Cation Methylammonium/Formamidinium/Phenylethylammonium Tin Iodide Perovskite. *J. Mater. Chem. A* **2019**, *7*, 9523–9529.

(82) Trimmel, G.; Rath, T.; Weber, S.; Handl, J.; Dimopoulos, T.; Kunert, B. Investigation of Triple Cation Tin Perovskite Solar Cells. Poster Presented at: International Conference on Hybrid and Organic Photovoltaics. Roma 2019.

(83) Shi, Z.; Guo, J.; Chen, Y.; Li, Q.; Pan, Y.; Zhang, H.; Xia, Y.; Huang, W. Lead-Free Organic–Inorganic Hybrid Perovskites for Photovoltaic Applications: Recent Advances and Perspectives. *Adv. Mater.* **2017**, *29*, 1605005.

(84) Stoumpos, C. C.; Frazer, L.; Clark, D. J.; Kim, Y. S.; Rhim, S. H.; Freeman, A. J.; Ketterson, J. B.; Jang, J. I.; Kanatzidis, M. G. Hybrid Germanium Iodide Perovskite Semiconductors: Active Lone Pairs, Structural Distortions, Direct and Indirect Energy Gaps, and Strong Nonlinear Optical Properties. *J. Am. Chem. Soc.* **2015**, *137*, 6804–6819.

(85) Krishnamoorthy, T.; Ding, H.; Yan, C.; Leong, W. L.; Baikie, T.; Zhang, Z.; Sherburne, M.; Li, S.; Asta, M.; Mathews, N.; et al. Lead-Free Germanium Iodide Perovskite Materials for Photovoltaic Applications. *J. Mater. Chem. A* **2015**, *3*, 23829–23832.

(86) Kopacic, I.; Friesenbichler, B.; Hoefler, S. F.; Kunert, B.; Plank, H.; Rath, T.; Trimmel, G. Enhanced Performance of Germanium Halide Perovskite Solar Cells through Compositional Engineering. *ACS Appl. Energy Mater.* **2018**, *1*, 343–347.

(87) Chen, M.; Ju, M. G.; Garces, H. F.; Carl, A. D.; Ono, L. K.; Hawash, Z.; Zhang, Y.; Shen, T.; Qi, Y.; Grimm, R. L.; et al. Highly Stable and Efficient All-Inorganic Lead-Free Perovskite Solar Cells with Native-Oxide Passivation. *Nat. Commun.* **2019**, *10*, 1–8.

(88) Zhang, L.; Wang, K.; Zou, B. Bismuth Halide Perovskite-Like Materials: Current Opportunities and Challenges. *ChemSusChem* **2019**, 1612–1630.

(89) Park, B. W.; Philippe, B.; Zhang, X.; Rensmo, H.; Boschloo, G.; Johansson, E. M. J. Bismuth Based Hybrid Perovskites A3Bi2I9 (A: Methylammonium or Cesium) for Solar Cell Application. *Adv. Mater.* **2015**, *27*, 6806–6813.

(90) Zhang, Z.; Li, X.; Xia, X.; Wang, Z.; Huang, Z.; Lei, B.; Gao, Y. High-Quality (CH3NH3)3Bi2I9 Film-Based Solar Cells: Pushing Efficiency up to 1.64%. *J. Phys. Chem. Lett.* **2017**, *8*, 4300–4307.

(91) Bai, F.; Hu, Y.; Hu, Y.; Qiu, T.; Miao, X.; Zhang, S. Lead-Free, Air-Stable Ultrathin Cs3Bi2I9 Perovskite Nanosheets for Solar Cells. *Sol. Energy Mater. Sol. Cells* **2018**, *184*, 15–21.

(92) Jiang, F.; Yang, D.; Jiang, Y.; Liu, T.; Zhao, X.; Ming, Y.; Luo, B.; Qin, F.; Fan, J.; Han, H.; et al. Chlorine-Incorporation-Induced Formation of the Layered Phase for Antimony-Based Lead-Free Perovskite Solar Cells. *J. Am. Chem. Soc.* **2018**, *140*, 1019–1027.

(93) Boopathi, K. M.; Karuppuswamy, P.; Singh, A.; Hanmandlu, C.; Lin, L.; Abbas, S. A.; Chang, C. C.; Wang, P. C.; Li, G.; Chu, C. W. Solution-Processable Antimony-Based Light-Absorbing Materials beyond Lead Halide Perovskites. *J. Mater. Chem. A* **2017**, *5*, 20843–20850.

(94) Correa-Baena, J. P.; Nienhaus, L.; Kurchin, R. C.; Shin, S. S.; Wieghold, S.; Putri Hartono, N. T.; Layurova, M.; Klein, N. D.; Poindexter, J. R.; Polizzotti, A.; et al. A-Site Cation in Inorganic A3Sb2I9 Perovskite Influences Structural Dimensionality, Exciton Binding Energy, and Solar Cell Performance. *Chem. Mater.* **2018**, *30*, 3734–3742.

(95) Adonin, S. A.; Frolova, L. A.; Sokolov, M. N.; Shilov, G. V.; Korchagin, D. V.; Fedin, V. P.; Aldoshin, S. M.; Stevenson, K. J.; Troshin, P. A. Antimony (V) Complex Halides: Lead-Free Perovskite-Like Materials for Hybrid Solar Cells. *Adv. Energy Mater.* **2018**, *8*, 1701140.

(96) Milot, R. L.; Klug, M. T.; Davies, C. L.; Wang, Z.; Kraus, H.; Snaith, H. J.; Johnston, M. B.; Herz, L. M. The Effects of Doping Density and Temperature on the Optoelectronic Properties of Formamidinium Tin Triiodide Thin Films. *Adv. Mater.* **2018**, *30*, 1804506.

(97) Dixit, H.; Punetha, D.; Pandey, S. K. Improvement in Performance of Lead Free Inverted Perovskite Solar Cell by Optimization of Solar Parameters. *Optik.* **2019**, *179*, 969–976.

(98) Marshall, K. P.; Tao, S.; Walker, M.; Cook, D. S.; Lloyd-Hughes, J.; Varagnolo, S.; Wijesekara, A.; Walker, D.; Walton, R. I.; Hatton, R. A. $Cs_{1-x}Rb_xSnI_3$ Light Harvesting Semiconductors for Perovskite Photovoltaics. *Mater. Chem. Front.* **2018**, *2*, 1515–1522.

(99) Zhou, Y.; Garces, H. F.; Senturk, B. S.; Ortiz, A. L.; Padture, N. P. Room Temperature "One-Pot" Solution Synthesis of Nanoscale CsSnI3 Orthorhombic Perovskite Thin Films and Particles. *Mater. Lett.* **2013**, *110*, 127–129.

(100) Zheng, X.; Chen, B.; Wu, C.; Priya, S. Room Temperature Fabrication of CH3NH3PbBr3 by Anti-Solvent Assisted Crystallization Approach for Perovskite Solar Cells with Fast Response and Small J-V Hysteresis. *Nano Energy* **2015**, *17*, 269–278.

(101) Liu, J.; Ozaki, M.; Yakumaru, S.; Handa, T.; Nishikubo, R.; Kanemitsu, Y.; Saeki, A.; Murata, Y.; Murdey, R.; Wakamiya, A. Lead-Free Solar Cells Based on Tin Halide Perovskite Films with High Coverage and Improved Aggregation Angewandte. *Angew. Chemie - Int. Ed.* **2018**, *57*, 13221–13225.

(102) Gao, W.; Ran, C.; Li, J.; Dong, H.; Jiao, B.; Zhang, L.; Lan, X.; Hou, X.; Wu, Z. Robust Stability of Efficient Lead-Free Formamidinium Tin Iodide Perovskite Solar Cells Realized by Structural Regulation. *J. Phys. Chem. Lett.* **2018**, *9*, 6999–7006.

(103) Chen, C.; Zhang, W. et al. Effect of BCP Buffer Layer on Eliminating Charge Accumulation for High Performance of Inverted Perovskite Solar Cells. *RSC Adv.* **2017**, *7*, 35819–35826.

(104) Kontos, A. G.; Kaltzoglou, A.; Siranidi, E.; Palles, D.; Angeli, G. K.; Arfanis, M. K.; Psycharis, V.; Raptis, Y. S.; Kamitsos, E. I.; Trikalitis, P. N.; et al. Structural Stability, Vibrational Properties, and Photoluminescence in CsSnI3 Perovskite upon the Addition of SnF2. *Inorg. Chem.* **2017**, *56*, 84–91.